Contributions to Performance Verification and Uncertainty Determination of Industrial Computed Tomography for Dimensional Metrology

Kim Kiekens

Jury:

Prof. Paul Van Houtte, voorzitter
Prof. Jean-Pierre Kruth, promotor
Prof. Wim Dewulf, co-promotor
Prof. Bert Lauwers
Prof. Martine Wevers
Prof. Shoufeng Yang
Prof. Simone Carmignato (Universita Degli Studi di Padova)

Dissertation presented in partial
fulfilment of the requirements
for the degree of Doctor in
Engineering Science

Uitgegeven in eigen beheer, Kim Kiekens, Celestijnenlaan 300B, B-3100 Heverlee (Belgium)

VOORWOORD

De eindstreep is gehaald! Bedankt aan iedereen die een stuk of stukje meeliep op dit pad.

Prof. Jean-Pierre Kruth, dankjewel voor alles wat ik van jou heb geleerd. Je bent top in onderzoek, steeds met een sterke link naar de industriële praktijk. Je behoudt altijd het overzicht over het groter geheel, en tegelijk heb je oog voor elk detail. Hoewel je letterlijk dag en nacht in de weer bent om alles te combineren, straal je op elk moment rust uit. Je wint prestigieuze prijzen, en behoudt op elk moment je bescheidenheid. Zowel op professioneel als op menselijk vlak ben je een voorbeeld voor velen.

Prof. Wim Dewulf, dankjewel voor het vertrouwen en de vele kansen die ik kreeg. Tijdens mijn onderzoekstijd werkte ik niet alleen aan dit doctoraat, maar heb je me ook betrokken bij heel wat andere projecten, waar ik veel van bijleerde. De laatste jaren waren hierdoor erg afwisselend en boeiend, precies wat ik nodig had om dit te kunnen afwerken.

Bedankt aan de leden van mijn begeleidingscomité en jury. Jullie tips, vragen en suggesties hielpen me om deze tekst te maken tot wat ze geworden is.

Collega’s op Groep T, dankjewel voor jullie steun, jullie humor, jullie luisterend oor, jullie geduld en de vele geanimeerde gesprekken en discussies! Merci, Rene, op jouw eigen manier, met weinig, maar wel de juiste woorden, gaf je me regelmatig de extra motivatie die ik nodig had om door te gaan.

Merci, Wim, voor je stille steun. Je hebt je meer dan eens hebt afgevraagd waarom ik dit allemaal wil doen, maar je hebt mijn “zotte ambitie” steeds ‘getolereerd’. Je sluit mee dit hoofdstuk af. Lieve Joppe, Eppo en Pippa, de combinatie van de zorg voor jullie met dit werk was vaak intens, soms niet evident, maar op elk moment zorgden jullie voor een welkome en fijne afwisseling. Merci, schatjes!

Mama en papa, inhoudelijk vanop een afstand, maar persoonlijk van heel dichtbij volgden jullie geduldig mee dit traject. Jullie nabijheid, voorbeeld en wijze woorden blijven – ook nu nog – helpen om de juiste weg te volgen. En Fran en Lynn, jullie ‘grote zus’ is nu ook “uitgestudeerd”…

Lieve vrienden, na zoveel intense momenten samen, avonden, weekends en vakanties zijn maar heel weinig woorden meer nodig, om heel erg begrepen te worden. Jullie steun was en is goud waard.

En bedankt, Laurence, voor je quote “Een doctorandus neemt zijn hersens overal mee… “. Ik heb hem vaak al lachend gebruikt… Nu mogen ze even “off”.

ABSTRACT

This dissertation started only a few years after the first CT machine for dimensional metrology was launched on the market. To be accepted as a competitive measuring technique, dimensional CT measurements should be traceable to the unit length. Verification and calibration procedures exist for many years for conventional measuring machines, but are not transferrable to CT due to a lot of new parameters, the specific configuration of the CT system and the characteristics of the X-rays. New, dedicated methods, techniques and verification objects are needed to be able to estimate the measurement uncertainty on dimensional measurements with computed tomography.

In a first part of this text, a new object is presented, allowing to estimate the error on both the voxel size and on the number of voxels (or edge detection). With a good estimation of these two uncertainties, the total uncertainty on the measured length can be determined. These uncertainties are influenced by random as well as systematic (uniform and non-uniform) errors.

A framework is presented to determine the measurement uncertainty of dimensional measurements with computed tomography, including all possible contributors to this total uncertainty budget. For each of the different sub-terms, it is explained how it should be evaluated. Based on experimental measurements, the different terms are quantified. At the end, it is explained how these different sub-terms should be combined to the total uncertainty on the measured length.

Although this framework is a valuable tool to estimate measurement uncertainty for certain objects, defining a correct, realistic uncertainty interval for a feature on a complex, industrial workpiece is still challenging.

KORTE SAMENVATTING

Dit proefschrift startte slechts enkele jaren nadat de eerste computer tomografie machines voor dimensionale metingen op de markt kwamen. Om als volwaardige meettechniek aanzien te worden moeten dimensionele metingen steeds traceerbaar zijn naar de universele definitie van de meter. Verificatie- en kalibratieprocedures voor conventionele meetmachines zijn al jarenlang ingeburgerd, maar al snel bleek dat deze niet rechtstreeks vertaalbaar zijn naar CT machines. Vele nieuwe parameters, de specifieke configuratie van de machines en de karakteristieke eigenschappen van de X-stralen vragen om aangepaste methodes, technieken en objecten die gebruikt kunnen worden om de meetonzekerheid eenduidig te bepalen.

In een eerste deel werd een nieuw object voorgesteld dat toelaat om zowel de fout op de voxelgrootte als de fout op het aantal voxels (of de randdetectie) in te schatten. Met een juiste inschatting van deze twee onzekerheden kan de totale onzekerheid op de gemeten lengte worden bepaald. De onzekerheid op de voxelgrootte én op het aantal voxels wordt beïnvloed door toevallige en systematische (uniforme en niet uniforme) fouten.

In deze tekst wordt een kader uitgewerkt, een leidraad voor het bepalen van de meetonzekerheid voor dimensionele metingen met computer tomografie, waarin al deze mogelijke fouten vervat kunnen worden. Voor elk van de verschillende termen wordt aangegeven hoe de bepaling van de onzekerheid kan gebeuren. Aan de hand van experimentele metingen op verschillende werkstukken is bovendien een inschatting gemaakt van de grootte van de verschillende factoren. Tenslotte wordt aangetoond hoe deze verschillende oorzaken van onzekerheid correct gecombineerd moeten worden om de totale onzekerheid op de gemeten lengte te berekenen uit alle sub-termen.

Hoewel dit kader een waardevol instrument is om de onzekerheid in te schatten voor een aantal objecten, blijft het definiëren van een realistisch onzekerheidsinterval voor een gemeten lengte op een complex industrieel werkstuk nog een uitdaging.

TABLE OF CONTENTS

Chapter 5: Uncertainty on the Number of Voxels u_n 77

LIST OF FIGURES

“Measure what can be measured, and make measurable what cannot be measured.”
Galileo Galilei

CHAPTER 1:
WHAT IS COMPUTED TOMOGRAPHY ?

1. WHAT IS COMPUTED TOMOGRAPHY?

Light, microwaves, X-rays and radio transmissions are several kinds of electromagnetic waves. The different names refer to different wavelengths. X-rays (or Röntgen radiation [1]) have a wavelength in the range of 10 to 0.01 nanometers, corresponding to frequencies in the range 10^{16} Hz to 10^{19} Hz.

Due to the small wavelength and high energy density, X-rays travel in straight lines and are able to penetrate and even pass right through a material sample. The level of penetration is influenced by the X-ray characteristics as well as the investigated properties of the sample, e.g. size, material, ….

When a large series of two-dimensional X-ray images are taken from different sides around a single axis of rotation, a three-dimensional image of the inside of an object can be generated. This procedure, known as computed tomography, was first developed by Godfrey Newbold Hounsfield and Allan McLeod Cormack in 1971. Around 1980, industry discovered the advantages of computed tomography for industrial applications.

2. GENERAL WORKING PRINCIPLE OF COMPUTED TOMOGRAPHY

The overall CT measurement procedure consists of four main steps: the data acquisition (1); the reconstruction of the 2D X-ray images to a 3D voxel model (2); edge detection on the voxel model (3); and data analysis / measurement (4), see *Figure 1*. A voxel is a 3D equivalent of a pixel.

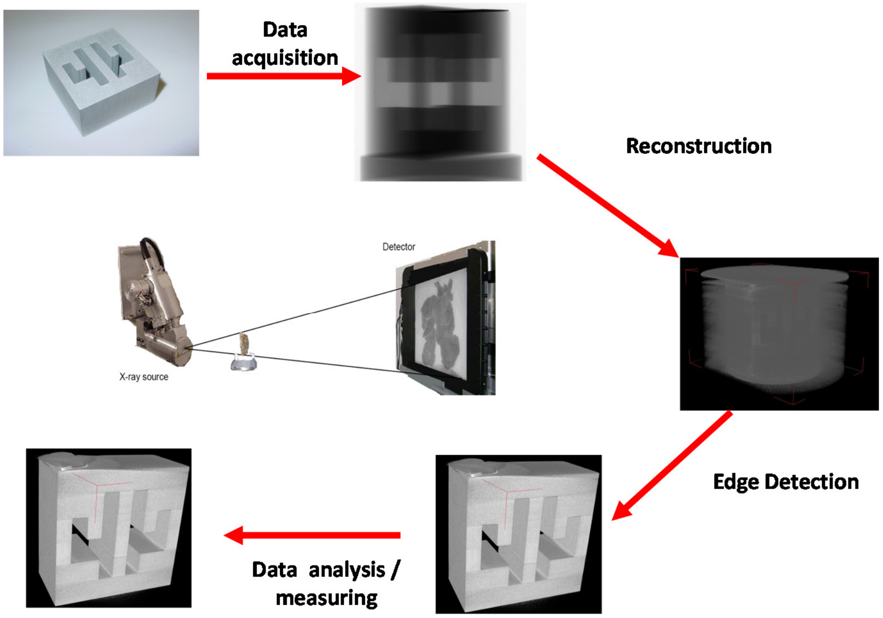

FIGURE 1: OVERVIEW OF CT MEASUREMENT PROCEDURE

This Section elaborates on each of these four main stages of a CT measurement.

The first step in each CT measurement is taking a few hundred or even thousands of 2D X-ray images, at different angular positions of the object over 360°, placed between the source and the detector (**data acquisition**).

Figure 2 shows the set-up for the **data acquisition** of the 2D images. The object is positioned in between the source and the detector. X-rays, produced by the source are partially penetrating and partially absorbed by the object, generating a 2D grey image on the detector.

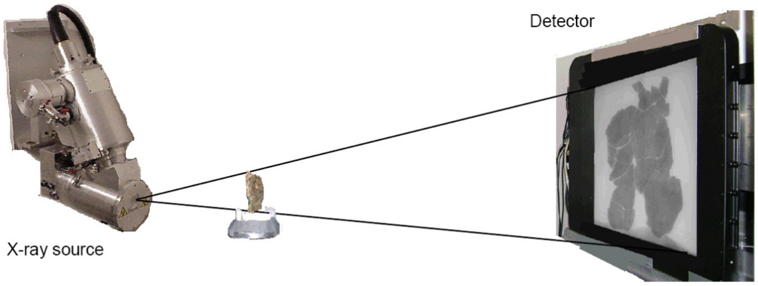

FIGURE 2: X-RAY SOURCE, ROTATION STAGE, DETECTOR [2]

Typically, in each position, several X-ray images are averaged, to deal with small fluctuations in the X-ray source spectrum.

For dimensional measurements, images are taken over 360°, in a circular scan. In this work, no helical CT is used. However Katsevich's helical algorithm [16] can theoretically lead to more accurate results; reconstructions from the real circular projections deliver better result in terms of measurement uncertainty [3].

The result of this this data acquisition step is an image stack of different 2D X-ray grey value images of the object.

Combining of these 2D images into a 3D voxel model is referred to as **reconstruction**. The images, produced using a cone beam X-ray source are reconstructed by a filtered backprojection algorithm, based on the method of Feldkamp [23]. In this dissertation, all reconstruction operations are performed using the software CTpro of Nikon Metrology (X-TEK). During reconstruction, the software offers the possibility to apply certain beam hardening correction and noise reduction algorithms, which will be used as such. Possible improvements on this reconstruction software are out of the scope of this dissertation.

The result of the reconstruction step is a 3D model, consisting of voxels. Before any analysis is feasible on this voxel model, a segmentation between background voxels and material voxels (**edge detection**) is required. In contrast to slice-by-slice thresholding methods [4], this dissertation only considers thresholding on the 3D voxel model. Section 3.3 will zoom in on the different edge detection methods and the consequences for the accuracy of the dimensional measurements on the obtained voxel models, analyzed in the **data analysis** step.

Edge detection and data analysis are performed using the software VGStudio MAX, Versions 2.1 and 2.2 [5].

3. CT SYSTEMS

3.1 CT MACHINE

For the purpose of this work, two different 225 keV machines of Nikon Metrology were used. A conventional 225 keV machine for industrial CT scanning (*Figure 3*), and a 225M (also 225 keV) machine, specifically designed for metrology applications. The main differences are the detector (a Varian 2520 versus a Perkin Elmer XRD 1621 detector) and the accuracy of the magnification axis, which has been improved in the 225M machine by adapting the mechanical design and the accuracy of the stepper motors controlling the axes.

FIGURE 3: 225KV CT MACHINE [2]

For materials research, typically devices with lower penetration powers are used (e.g. 120 keV). For very dense parts (e.g. turbine blades), CT machines with higher power are used (320 – 450 keV).

In March 2013, Fraunhofer presented the world's largest CT system (XXL Tower CT) allowing to perform complete, non-destructive inspections of large objects such as e.g. complete cars [6]. This system however was not designed for metrology applications.

The main components of each and every CT machine are an X-ray source, a rotation stage and a detector, discussed more in detail below.

3.2 HARDWARE

Source

The X-ray tube

The X-ray tube is a device which is designed to produce fast-moving electrons which are subsequently decelerated suddenly, causing a part of their energy to be converted into X-rays. It basically consists of a cathode filament, an anode, a target, and magnetic lenses (*Figure 4*).

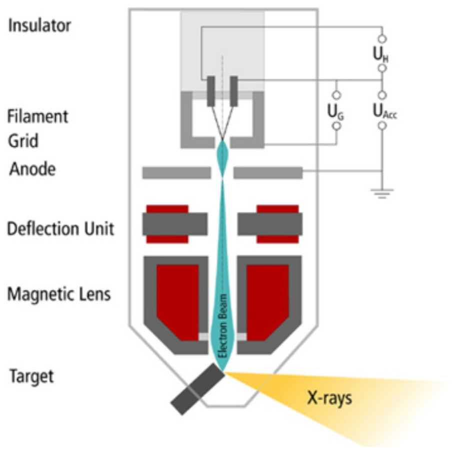

FIGURE 4: X-RAY TUBE [7]

The **filament** is a tungsten wire, from which electrons with sufficient energy can escape to form a negatively charged electron cloud.

The electron beam is focused onto a **target** using a series of deflecting magnets and an electromagnetic lens. When hitting this target, the fast moving electrons are decelerated very suddenly, causing their energy to be converted into heat and X-rays. For the target, different materials can be used, e.g. copper, tungsten, …, each producing a different X-ray spectrum.

The **magnetic lens** is used to focus the electrons on a spot on the metallic target. Obtaining a sharp, high-resolution X-ray image requires a very small spot size. If the X-ray spot size is too large, blurred regions are created in the X-ray image, as shown in *Figure 5*.

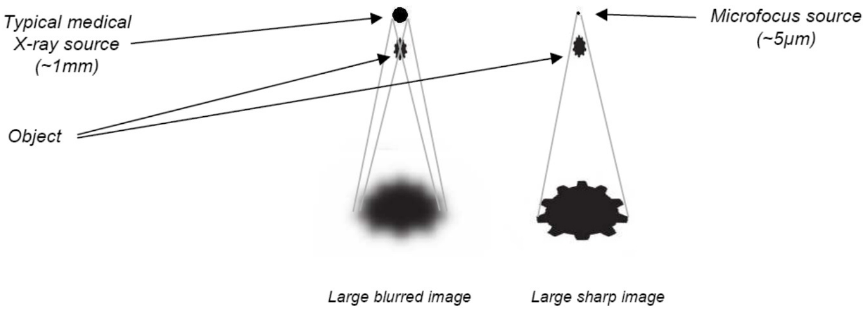

FIGURE 5: SPOT SIZE INFLUENCES THE SHARPNESS OF THE IMAGE [8]

Micro focus means that the size of the X-ray source is only a few microns.

Production of X-rays

Electrons reaching the target from the filament of an X-ray tube may possess up to e.g. 450 keV of kinetic energy, depending on the voltage across the X-ray tube. These high-energy electrons travel at up to 80% of the speed of light and interact with the atoms of the target material in a number of ways, most of which only serve to increase the temperature of the target. Unfortunately, these heat-producing interactions are far more likely to occur than X-ray producing interactions, and less than 1% of the energy deposited on the target of an X-ray tube is converted into a conical beam of X-radiation [9], see *Figure 6*.

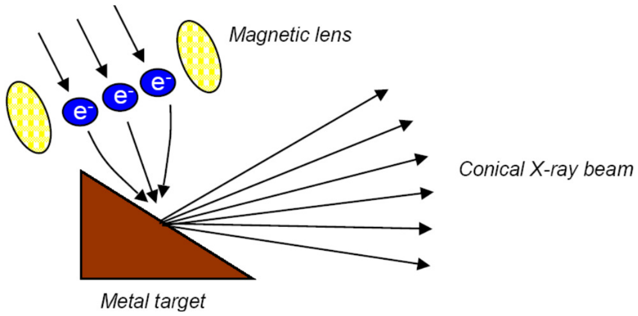

FIGURE 6: PRODUCTION OF X-RAYS [8]

There are two types of interactions which do result in the emission of X-rays:

1) An electron travelling at high speed may experience a sudden change in its direction of motion.
2) An electron in an atom may undergo a transition from a high energy state to a lower energy state.

The **first X-ray production mechanism** is the production of radiation in the form of X-rays due to the deceleration of a high energy electron by electrons orbiting an atom in the target. This process is called **Bremsstrahlung -** translated from German as braking radiation.

This is the dominant X-ray production process and produces a wide spectrum of X-ray energies up to the accelerating voltage, so photons of all energies (X-ray energies) are created. The result is an X-ray beam having a continuous spectrum. The number of photons decreases by increasing X-ray energy.

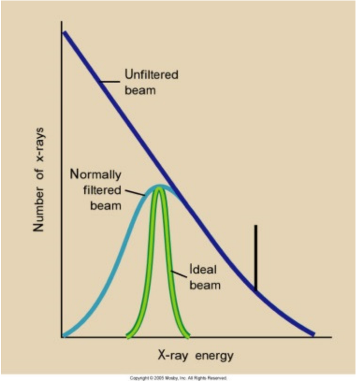

FIGURE 7: THE CONTINUOUS SPECTRUM OF BREMSSTRAHLUNG X-RADIATION AND THE CHARACTERISTIC RADIATION (PEAK AT SPECIFIC X-RAY ENERGY) [10] (REMARK: AT ENERGY = 0, NO X-RAYS ARE PRODUCED)

The **second X-ray production mechanism** involves a collision between the electrons at high speed and the orbital electrons in the atom. The interaction occurs if the incoming electron has more kinetic energy than the binding energy of the electron within the atom. When this condition exists, and there is a collision, the electron will be dislodged from the atom. The orbital electron that is removed leaves a vacancy that is filled by an electron from a higher energy level. When the filling electron moves down to fill the vacancy, it gives up energy emitted in the form of an X-ray photon. This is known as characteristic radiation since the energy of the photon depends on the target material.

The spectrum of radiation of this type of interaction is a line spectrum (vertical black line in *Figure 7*).

X-ray emission spectrum

The **target material** and the X-ray settings (voltage and current) all have an influence on the X-ray emission spectrum.

High atomic number elements like gold (Z=79) and tungsten (Z=74) enable to reach higher penetration (because the spectrum is shifted towards high energy levels), enhancing the efficiency of X-ray generation [10], *Figure 8*.

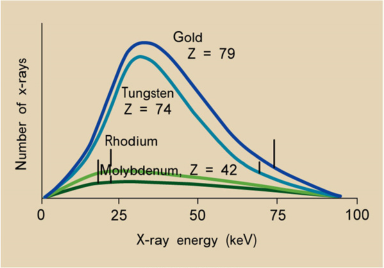

FIGURE 8: DEPENDENCY OF THE X-RAY EMISSION SPECTRUM ON THE CHOSEN TARGET MATERIAL – THE INTENSITY OF BREMSTRAHLUNG IS SIGNIFICANTLY REDUCED FOR MATERIALS WITH LOWER ATOMIC NUMBER [10]

Also the **tube current and voltage** have an effect on the X-ray spectrum produced, *Figure 9*. A change of tube current changes the amplitude of the X-ray spectrum; an increase of the voltage increases the amplitude of the spectrum, but also shifts the curve towards higher energy levels.

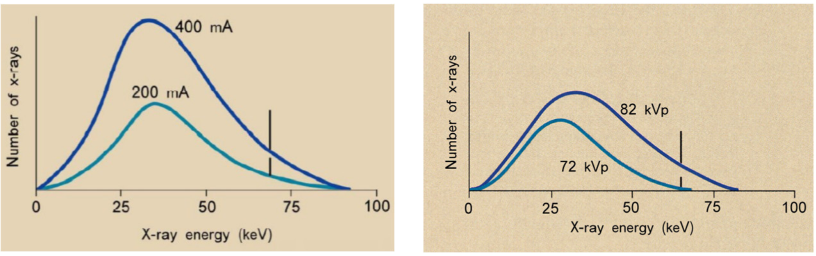

FIGURE 9: DEPENDENCY OF THE X-RAY EMISSION SPECTRUM ON THE X-RAY SETTINGS (VOLTAGE AND CURRENT) [10]

When a polychromatic beam of X-rays passes through a homogeneous material, the intensity of the rays is decreased due to scattering and absorption. After passing through a sample of thickness s [m], the initial X-ray beam intensity I_0 changes into the attenuated intensity I. For a homogenous material, this process can be described by the law of Lambert-Beer. μ is the linear attenuation coefficient [1/m].

$$I = I_0 \cdot e^{-\mu s}$$

For inhomogeneous materials, the equation must be rewritten as follows

$$I = I_0 \cdot e^{-\int \mu \cdot ds}$$

Since the X-ray beam is polychromatic, the beam transmission does not follow the simple exponential decay seen with a monochromatic X-ray.

Rotation stage

During the scan, the object is mounted on the rotation stage. For dimensional metrology, the accuracy of the rotation stage is extremely important, since a misalignment of the rotation stage can cause important artifacts.

Whereas lenses can be used to magnify optical images, this principle cannot be used for X-rays. Geometric magnification is used by moving the sample and the rotation stage closer to the X-ray source (and vice versa). The position of the rotation stage between the source and the detector is therefore determining the magnification of the workpiece (hence the rescale factor).

Detector

Two main types of detectors exist: line detectors (*Figure 10,* left) for 2D CT and flat panel detectors (*Figure 10*, right) for 3D CT. Due to the cone beam, differences occur between the center and top and bottom of the detector. These problems can be overcome by using a line detector. The main drawback is the longer scanning time, since the rotation has to be combined with a translation for a full scan of the object. With a flat panel detector, a 3D model of the object can be generated during one single rotation of the workpiece.

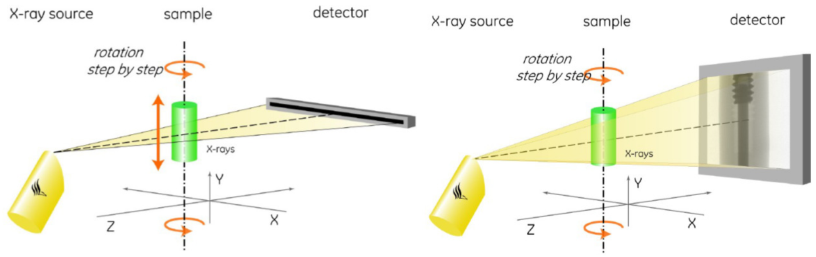

FIGURE 10: LINE DETECTOR (LEFT) AND FLAT PANEL DETECTOR (RIGHT)

In this work, all measurements are acquired with a flat panel detectors.

3.3 SOFTWARE

3D reconstruction

Once a set of 2D X-ray images is being combined into a 3D volume, we can speak of Computed Tomography, instead of 2D X-ray imaging. Digital geometry processing is used to generate a three-dimensional image of the inside of an object from a large series of two-dimensional X-ray images taken around a single axis of rotation.

After reconstruction, the result is a three-dimensional volume. Commonly, a filtered back projection method is used for reconstruction of the 3D model from the 2D X-ray images [11]. Also the software used in this work (CT pro) is based on this filtered back projection algorithm.

For a good quality CT volume around 1000 projection images are used. To collect these in a reasonable time we use continuous rotation. Typical scans are 20 minutes (1500 images) or 40 minutes (3000 images).
Most scans presented in the next chapters are taken with 1000 images.

Surface determination and thresholding

Under ideal conditions, a CT scan of a homogenous material would produce a voxel model of one single grey value. However, due to the partial volume effect, the voxels at the edges have different grey values (*Figure 11*). Under ideal conditions it would be possible to define the component surface simply by determining the grey value threshold. This threshold, also known as the ISO50% threshold in the software used (VG Studio Max), could be calculated as the mean value from the material grey value and the image background grey value. Such an ISO50% threshold value could be used to describe the entire component surface in the CT data set [12].

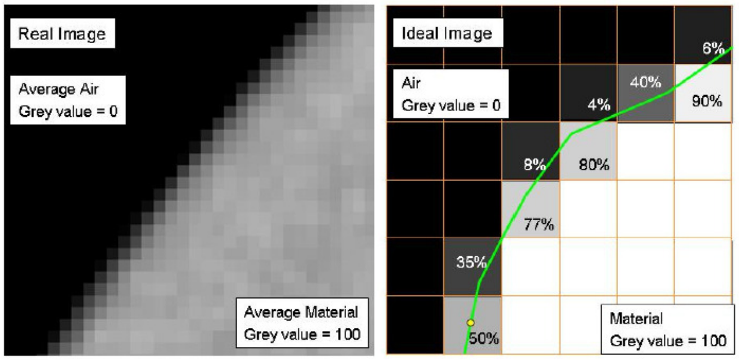

FIGURE 11: REAL AND IDEALIZED CT SLICE IMAGE. THE GREEN LINE IN THE IMAGE ON THE RIGHT REPRESENTS THE COMPONENT SURFACE. THE PERCENTAGES SHOWN REPRESENT THE OVERLAP OF THE RESPECTIVE VOXEL WITH THE OBJECT AND THE VOXEL GREY VALUE AT THE SAME TIME [12]

However, artifacts such as beam hardening and scattering cause that the surface cannot be described by the ISO 50% value. Even on one voxel model the correct threshold value for the outer and inner dimensions will be different. On *Figure 12*, the change in diameter of an inner and outer cylinder with changing edge grey value is shown.

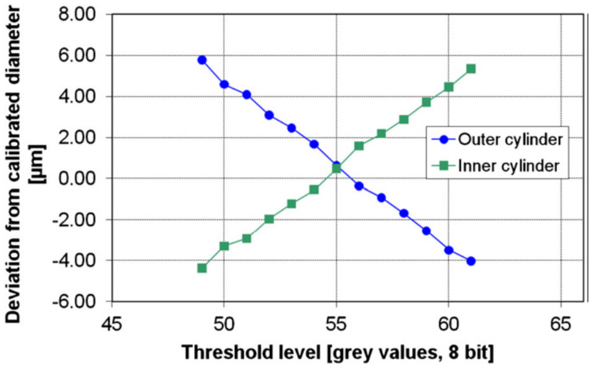

FIGURE 12: INFLUENCE OF THE THRESHOLD VALUE ON THE MEASURED DIAMETERS OF CYLINDRICAL FEATURES. AS THE THRESHOLD VALUE INCREASES, DIAMETERS OF INNER CYLINDERS INCREASE, WHILE DIAMETERS OF OUTER CYLINDERS DECREASE [13]

More complex algorithms allow to define the surface grey value locally. Since the threshold is not simply described by the ISO50% value, in this dissertation local thresholding is used for most of the measurements, unless stated otherwise.

Data correction

Since the standard thresholding techniques available in the software (VGStudio MAX 2.0, 2.1 and 2.2) are unsatisfactory (even these working with local adaptive thresholding), a data correction is needed to improve the dimensional measurements. The following chapters will zoom in on this data correction and the measurement uncertainty on this edge detection step.

4. INFLUENCE FACTORS

Although industrial Computed Tomography has evolved into a promising dimensional measurement technique, the result of a CT dimensional measurement is still influenced by many different parameters [14, 15]. In addition to the factors influencing a traditional dimensional measurement, further error sources related to the measurement set-up and algorithms used to reconstruct the 3D model out of the 2D images occur in CT measurements.

Cantatore summarized the main influence factors, ordered by type, and listed in *Figure 13*. Similar overviews are made by others, e.g. by Carmignato [13].

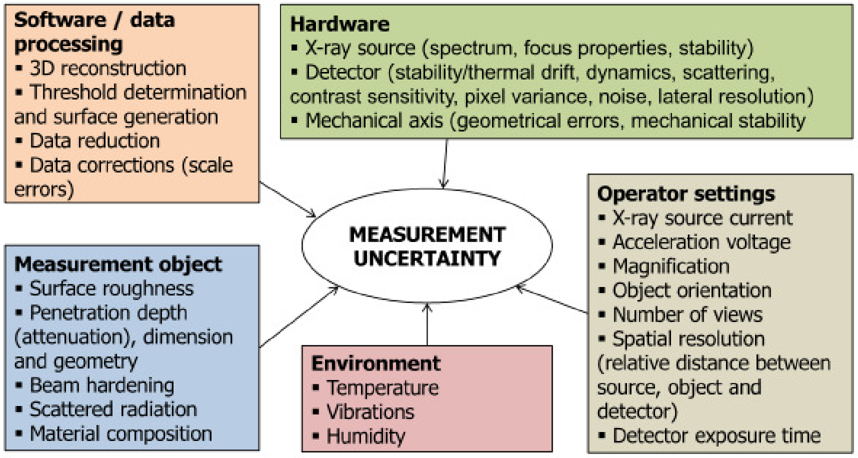

FIGURE 13: ERROR SOURCES IN 3D X-RAY MICRO-CT MEASUREMENTS [17]

Investigating the influence of all different parameters is challenging, not only due to the number of parameters having an effect on the CT measurement result, but also due to the mutual influence of some of these parameters. E.g. changing the object material (or orientation) often asks for other X-ray settings and filtration, which hinders the investigation of the effect of one single factor on the CT result by experimental measurements.

Two main artifacts influencing every CT measurement, especially for dense materials, are beam hardening and scatter.

4.1 BEAM HARDENING

The attenuation processes of X-rays in matter are energy dependent. In general, X-rays in the lower energy ranges are more easily attenuated. They are referred to as soft X-rays. In contrast, those in higher energy ranges are more penetrating, and referred to as hard X-rays.

The X-ray beams produced in X-ray tubes are however polychromatic, with a moderately broad energy spectrum. While the X-ray beam is penetrating material, the low-energy X-rays of the beam are more easily absorbed, hence selectively removed from the beam. Consequently, the higher-energy (hard) rays remain, and the beam becomes progressively harder or more penetrating as it transverses through matter. This phenomenon is referred to as beam hardening. The amount of beam hardening depends on the initial X-ray spectrum as well as on the composition of the material traversed [18, 19, 20]. This effect causes so-called beam hardening artifacts in CT images.

Common X-ray systems are standard equipped with a filter, such as a thin aluminum or copper plate, which reduces the beam hardening effect. The filter is placed between the source and the object, absorbing low energy X-rays before the beam reaches the actual sample material. The main disadvantage of this technique is the decreased amount of soft X-rays, which results in a decrease of the image signal-to-noise ratio especially for low absorbing objects. Furthermore, this method gives only a reduction of the beam hardening effect [21]; it cannot be removed completely by a hardware filter. Besides hardware filtering beam hardening effects can be corrected (partially) with a software filter during reconstruction.

4.2 SCATTERED RADIATION

Due to interactions with matter in the path of the radiation beam, photons can be redirected, which is called scatter. As a result of this, the scattered photons will not reach the detector at the place they were originally directed to. In addition, the scattered photons may transfer a part of their energy to atoms or electrons of the material [22].

The primary important interactions between the X-rays and the matter are
- Photoelectric effect
- Compton scattering
- Rayleigh scattering
- Pair production

X-ray scatter leads to errors in reconstruction because the effect changes with each projection [20].

5. CHALLENGES

Notwithstanding a lot of adaptations to industrial CT systems (in hardware as well as in software) during the last few years, **metrological traceability establishment** is still a major challenge for CT measurements due to the complex physical properties of X-rays and the numerous sources of uncertainty, which complicate tracing back the CT results to the international length standard [15]. An illustration of metrological traceability through a calibration hierarchy for dimensional measurements is given in *Figure 14* [24].

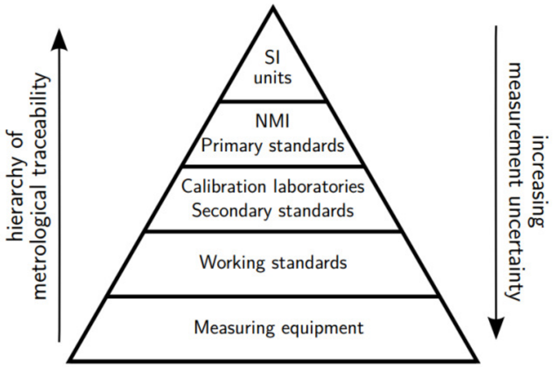

FIGURE 14: ILLUSTRATION OF METROLOGICAL TRACEABILITY THROUGH A CALIBRATION HIERARCHY [24]

The lack of traceability implies that evaluating measurement uncertainty (hence expressing the reliability of the dimensional measurement results) and determining the actual metrological performance of CT systems are still difficult.

Internationally standardized procedures on metrological performance testing of CT systems and error quantification are not available yet. Only draft international or national guidelines exist [25, 26]. The current lack of well-defined calibration procedures and of reference objects suited to assess the accuracy of CT systems limits the ability to quantify effectively deterministic errors in view of subsequent error correction and traceability establishment. The lack of standardized procedures also limits the comparability of CT systems mutually as well as to other coordinate measuring systems [27] and is one of the main reasons for limited consideration of CT as a valid measuring technique in industry. CT dimensional measurements have to become traceable and their results have to be comparable to Coordinate Measurement Machine (CMM) results in order to reach the same recognition for coordinate metrology applications [28].

6. CONCLUSION

Computed Tomography is a well-known technique applied for many decades in materials research and medical industry. The main steps to create a 3D voxel model are the data acquisition in the CT machine, the reconstruction of the 2D images in a 3D model, the edge detection on this model and the data analysis.

The main hardware components of a CT system are the X-ray source, the rotation stage (to mount the workpiece) and the detector.

Many factors are influencing the final result of a CT scan: beam hardening and scatter are the most important, but definitely not the only ones. In the next chapter, the state of the art of dimensional metrology with CT is given, elaborating on all the different parameters influencing accurate CT metrology.

Although CT has many advantages for dimensional metrology, and the growing interest in CT as a measuring technique, the lack of traceability and many influencing factors determining the uncertainty on the measured value hinders this technique to be accepted as a reliable, robust measuring technique in industry.

"Il n'est pas certain que tout soit incertain."
Blaise Pascal (°1623 - †1662)

CHAPTER 2: STATE OF THE ART AND RESEARCH OBJECTIVES

The adaptation of X-ray Computed Tomography to manufacturing metrology offers new possibilities for coordinate measurements. CT offers the possibility to acquire a volumetric model with a single measurement at which analyses such as the estimation of geometric features can be performed [29].

The influence of the different parameters on CT measurements is studied by several researchers, using simulations as well as experiments. The first section of this chapter provides an overview of the effect of the most important influence factors on CT measurements.

Notwithstanding the many influence factors, there are currently two different principles already applied in industry to ensure traceability establishment and performance verification for computed tomography: multi-sensor metrology [30, 31, 32] or the use of verification artefacts [33, 34]. An overview of the currently existing verification objects for CT measurements is given in Section 2.

Estimating measurement uncertainty up to now is mostly done by 'translating' existing standards for conventional measuring machines to systems with CT sensors. CT with his specific characteristics asks for a dedicated procedure for measurement uncertainty determination.

This chapter concludes with the research objectives for this dissertation.

1. INVESTIGATION OF INFLUENCE FACTORS

In this section, the literature about the investigations of influence factors on CT dimensional measurements is given. The structure is according to the overview of parameters proposed by Cantatore et al. [17] as referred to in Chapter 1.

1.1 X-RAY SOURCE

Source pre-filtration

Wenig and Kasperl investigated besides the alignment accuracy and the detector exposure time the effect of source pre-filtration. From this investigation, the *source pre-filtration* was figured out to have a distinct influence on the measurement quality [35]. The relative measurement error decreases with increasing source pre-filtration. For the object studied, the error reduces to value for the monochromatic reference value using a 4 mm Cu filter.

Reiter et al. [36] simulated 22 parameter combinations for a hollow stepped cylindrical test part. By comparing the results with a tactile CMM measurement, Reiter concluded that beam hardening effects can best be reduced by using pre-filter plates or applying a correction algorithm. Increasing the acceleration voltage also reduces measurement deviations, but not as much as a proper filter.

Voltage variations

Hiller and Kasperl [37] used simulations to investigate the influence of *the magnification*, *the orientation of the workpiece* and *voltage variations* during a CT measurement. No significant errors could be measured after introducing voltage variations in simulated measurements.

1.2 DETECTOR

The detector exposure time can be set for every measurement, and is user dependent. It seems that the longer the *detector exposure time* is, the smaller the relative measurement errors are. At an exposure time of 400 ms, the results are comparable to a simulation without noise [35].

1.3 MECHANICAL SYSTEM

Detector alignment

Errors up to 24% of the voxel size are measured, for a detector tilt of 1 pixel (pixel size 400 µm) by Wenig and Kasperl [35]. The effect of the *object configuration* within the scanner and *errors in the system geometry* are studied by Kumar et al. [38]. Simulation analysis shows that if there is an error in the geometrical parameters, then the position and orientation of a test object have an impact on the accuracy of the measurements. They conclude that for accurate measurements, the detector tilt should be less than 1° of the ideal geometry during all scanning tasks.

Errors in system geometry

Using numerically generated CT data and statistical evaluation methods, Hiller and Reindl [39] demonstrated, using a case study, the practical application of simulation methods to investigate the effect of *image artefacts* (like beam hardening and scatter) and geometrical scanner misalignment. Based on 50 simulations (limited for reasons of computational time) of a hollow stepped cylinder (with 2 steps), they evaluated the accuracy and uncertainty of the measurements. Varying a set of 20 parameters (of the X-ray tube, the scanning geometry and the clamping system) and performing about 50 simulations, the maximum measured deviation was about 10 µm on a diameter of 10 mm. The authors state that to increase the reliability of the estimation, the number of simulations should be increased.

1.4 MEASUREMENT OBJECT

Beam hardening

Beam hardening is studied by many researchers. Beam hardening is a particular problem with high atomic number materials such as steel and ceramics. Compared to low atomic number materials such as plastic, these high atomic number materials have dramatically increased attenuation at lower energies. The effect of beam hardening is visualized in *Figure 15*.

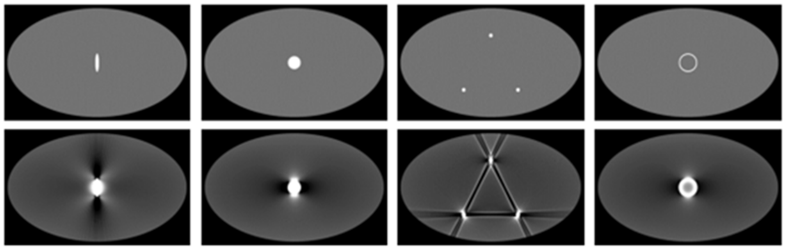

FIGURE 15: SIMULATED SCANS WITHOUT (TOP ROW) AND WITH (BOTTOM ROW) BEAM HARDENING, SHOWING THAT DARK STREAKS OCCUR ALONG THE LINES OF GREATEST ATTENUTATION, AND BRIGHT STREAKS OCCUR IN OTHER DIRECTIONS [40]

Not only on the 2D slices, but also in the 3D voxel model, beam hardening hinders edge detection and so accurate dimensional measurements. However, most studies focus on image quality, rather than on the effect on metrology applications.

In homogeneous objects it appears that inner regions are less dense than border areas. This effect is known as cupping artefact [41], illustrated in *Figure 16*, where the grey value changes over de diameter of the cross section.

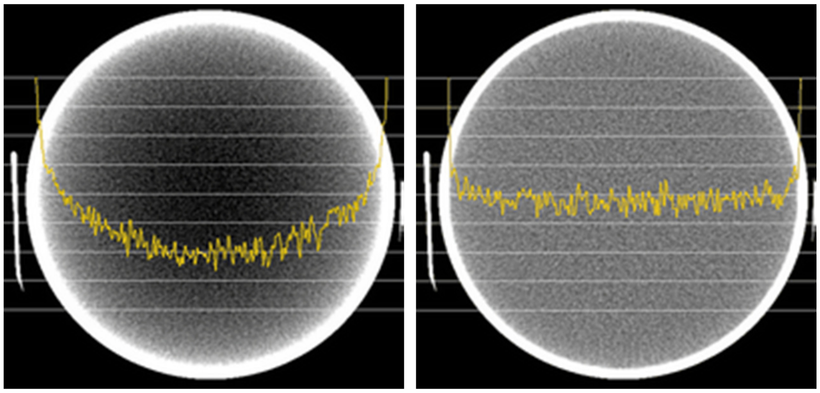

FIGURE 16: CUPPING ARTEFACT [42]

By comparing simulations and experiments Krimmel et al. [43] investigated the effect of the X-ray source, the geometrical set-up, the sample properties and the detector properties on the formation of image artefacts in X-ray CT, resulting from beam-hardening.

Another common method to reduce beam hardening artifacts in mono-material objects is the **linearization technique.** It is based on the estimation of the relation between a propagated path length within the specimen and an according measured weakened intensity by means of various estimation algorithms. The resulting characteristic line can be used to compute beam hardening corrected intensity values which allow the reconstruction of an artifact free CT image [44, 45].

For multi-material objects, this problem becomes even more challenging [46, 47]. Krumm et al. [45] and Kasperl [22] proposed a method to deal with beam hardening for multi-material objects by combining the advantages of linearization and post-reconstruction methods.

Another way to deal with multi-material objects is using **dual energy CT** [48], [49]. The main idea of Dual Energy Computed Tomography (DECT) is to utilize different X-ray spectra (dual exposure technique) in order to optimally characterize multi-material objects. A fusion step combines the two complementary DECT datasets, featuring the strength of each dataset [50].

Another method is **Iterative Surface Normalisation**, generating a normalized voxel volume, optimized for surface extraction [51, 52].

Mostly, beam hardening correction is applied using a **hardware pre-filter** or a **beam hardening correction algorithm** in the reconstruction software [53, 54, 55]. Using BHC improves the position accuracy for the sphere center distance on a calotte plate by approximately a factor two [53]. Based on two measurements (one with and one without an automated beam hardening correction (BHC) in the software) of a sphere calottes plate made of Zerodur®, it was shown that the range of errors on the sphere center distances is halved using a BHC compared to the measurement without beam hardening correction. With a voxel size of 100 µm, the range of errors on the distances only was ± 1,5 µm with BHC [55].

In [54], it has been shown that beam hardening correction is in some cases improving the absolute accuracy. However, this not always holds true. It has been observed that beam hardening correction can introduce a dependency of dimensional measurements on the amount of surrounding material.

Image artifacts

Combining and comparing of CT measurement data with simulated CT models was carried out by Hilpert et al. [56]. By comparing the characteristics of the measurement output of CT and the output gained from simulation, the *influence of measurement artefacts* was judged in analogy to existing guidelines of coordinate metrology. Adding noise, ring artefacts and beam hardening to the simulation introduces form errors in the order of magnitude of one voxel at the specified position.

1.5 OPERATOR SETTINGS

Magnification

On simulated data, with increasing voxel size, the unsharpness of the data increases [37]. Using a ball plate as workpiece, it has been shown the magnification is a very important influence factor in real measurements. For two different magnification positions, differences in the measured ball center distance are measured to be up to 15 µm [57].

Object orientation

Using simulations, the object position and orientation do not seem to have any significant effect on the measurement accuracy provided there is no error in the system geometrical parameters if noise is not taken into account [38]. However, in certain orientations (45°) slightly bigger deviations are measured compared to the 0°-position for a calotte plate [40]. When simulating a CT measurement of the calotte plate in horizontal and vertical direction, the residual errors in the vertical position were observed to be maximum ± 6.5 µm [56].

Real measurements have proven that the positioning of the workpiece in the measurement volume is vital for the quality of the measurements. A bad orientation (e.g. a flat plate parallel to the X-ray beam) introduces artifacts which have to be avoided (e.g. by wobbling) [13]. Planes perpendicular to the rotational axis are more subject to noise, impeding accurate measurement of their mutual distance [58]. An optimal orientation (e.g. taking into account stability, X-ray penetration lengths, …) of the workpiece demonstrates a superior reduction of artifacts and distortions [59].

Number of projections

Measuring a ball bar showed that more than 800 projections reduce the deviations on the measured sphere center distance by less than 5% [57].

2. VERIFICATION OBJECTS

The measurement capability of CT measurements depends on the knowledge of the measurement uncertainties present. To deal with the copious number of influencing factors and the artifact errors (beam hardening and scatter), verification objects were designed enabling to compensate the effects of these main disturbing factors. The attempt of using verification objects is – similar to objects used in conventional measuring machines – to identify measurement uncertainty as well as to identify systematic errors and to correct for them where possible (verification and correction).

2.1 SIMPLE GEOMETRIES

Similar to the verification objects used for conventional measuring machines, many objects used for CT verification have simple geometries, or consist of a combination of elementary features (spheres, cylinders, planes). Based on the idea of a ball bar used for CMM's [60] a combination of spheres is often used, mainly for voxel size correction (see Chapter 4).

The ability of CT to measure inside objects, asks for calibrated objects with internal features. A hollow cylinder (*Figure* 17) is a typical example of a calibrated object often used for the determination and correction of edge offsets of CT measurements [61].

Besides this hollow cylinder, Bartscher presented a stepped cylinder in aluminum and a ball bar to correct for typical CT errors [61], see *Figure 17*. The ball bar of *Figure* 17, also has been used to investigate the CT dimensional measurement process chain [62] and to check the change of the rescale factor over time [63].

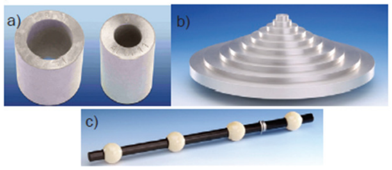

FIGURE 17: CALIBRATED OBJECTS BASED ON "SIMPLE" FEATURES [61]

To investigate the maximum tolerable detector rotation around both the X and Z-axis (as defined on *Figure* 10), Wenig and Kasperl [35] used a thin cylinder with a sphere at each end as a test object, as depicted in *Figure 18*. By varying the detector tilt from 0.014° to 0.22°, it was concluded that tilts of less than 0.056° on the detector don't have an influence on the geometry and thus on the dimensional measurements, because the error will be in the order of magnitude of the reconstruction artefacts and noise.

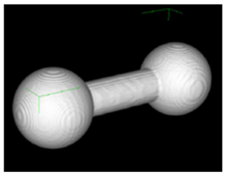

FIGURE 18: THIN CYLINDER WITH SPHERE AT EACH END [35]

Hiller et al. used a similar ball bar (with two spheres) to do a performance evaluation of an X-ray micro-computed tomography system for dimensional metrology applications [64]. The repeatability of the distance between the balls, over 8 measurements performed on different days and including repositioning was measured to be 30% of the voxel size, which was 29,6 µm.

2.2 CALIBRATED TEST PIECE WITH LARGE SET OF SPHERES

This calibrated test piece consists of 27 ruby spheres mounted on carbon fibre shafts. This object (*Figure 19*, left) incorporates a large number of distances and directions in a single test part, as the sphere-centre to sphere-centre distances of several pairs of spheres can be measured [65]. This calibrated object can be used for accuracy as well as repeatability determination.

Welkenhuyzen [66] designed a similar calibrated object *(Figure 19*, right), with spheres of different diameters, to compare experimental measurements with simulations. With this calibrated object, the influence of the position of the sphere with respect to the rotation center was clearly shown.

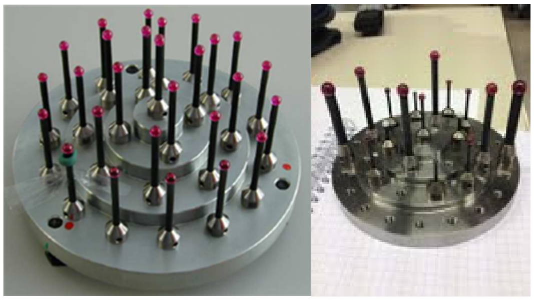

FIGURE 19: CALIBRATED TEST PIECES FOR ACCURACY / REPEATABILITY DETERMINATION CONSISTING OF 27 RUBY SPHERES (LEFT: [65]; RIGHT: [66])

2.3 CT BALL PLATE

The CT ball plate (consisting of 25 spheres glued on a carbon fiber plate) presented in [67] enables to measure probing errors and length measurement errors in accordance to procedures applied in traditional coordinate metrology (*Figure 20*Figure 23). The concept of this calibrated object is similar to the calotte plate developed by PTB (see next section). However, the use of ruby spheres minimizes manufacturing inaccuracies.

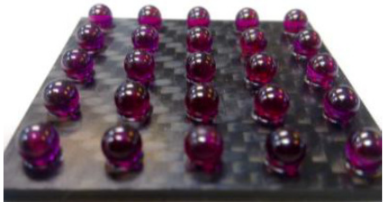

FIGURE 20: CT BALL PLATE [67]

Length measurement errors were calculated for two measurements at different orientations in the machine (straight and flat, or perpendicular and parallel to the beam). In the first position, the Feldkamp effect at the borders of the X-ray detector causes errors up to three times bigger than in the flat position.

In [68] this CT ball plate was used to investigate the influence of image quality on dimensional CT measurements. Image quality was assessed in terms of spatial resolution and pixel noise.

2.4 CALOTTE PLATE/CUBE PTB

A well established and high-potential reference standard is a calotte plate or cube featuring spherical calottes (*Figure 21*), made of Zerodur (glass-ceramic). The so-called calotte-plate and cube are designed by PTB based on the concept of ball plates for calibration of coordinate measuring machines. The calotte plate and cube are suitable to determine several characteristic parameters at the same time (e.g. errors in sphere distances, sphere diameters as well as form errors). They can be measured in different positions in the measurement volume, to determine spatial distribution of errors, similar to the use of ball plates for CMMs [69].

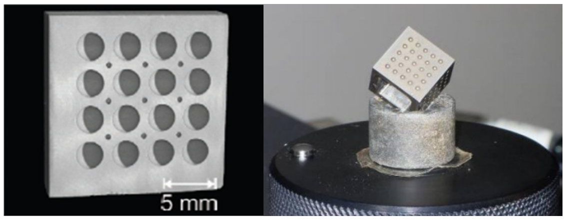

FIGURE 21: CALOTTE PLATE PTB [69] (LEFT); CALOTTE CUBE [70] (RIGHT)

The PTB calotte cube also has been used to test the influence of data filtering on dimensional measurements with CT [70]. Filters under investigation were median filters on projections as well as filters during filtered back projection and filters on the reconstructed volume. The form as well as the length measurement error improved compared to the unfiltered data set.

A calotte cube has been employed in the first Interlaboratory Comparison of Computed Tomography Systems for Dimensional Metrology, organized by the University of Padova (*Figure 22*) [71, 72].

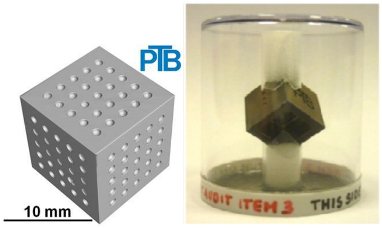

FIGURE 22: PTB CUBE, USED IN THE FIRST CT AUDIT [71, 72]

Also Hiller [37] used this object to investigate the influence of different parameters on the CT accuracy.

Neuschaefer-Rube et al. compared the procedures and standards for the testing of tactile and optical micro-sensors and micro-computed tomography (micro-CT) systems for coordinate metrology based on measurements of these calibrated objects [73].

2.5 Dismountable workpiece-near reference body (mini-cylinder head)

All calibrated objects mentioned higher only contain simple regular geometries (planes, cylinders and spheres), are not similar to real workpieces and do not contain any freeform shaped parts, being a challenging measurement task for CT and other sensors. Moreover, CT enabling to measure the inside of objects, asks for the study of properties of CT measurements in the interior of the geometry.

The cast freeform shaped part shown in *Figure 23* is especially designed for the study of the inside of objects, made out of different materials.

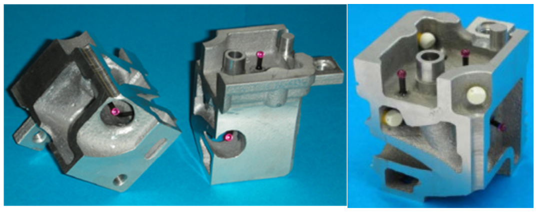

FIGURE 23: DISMOUNTABLE WORKPIECE-NEAR REFERENCE BODY [74] (LEFT); MINI-CYLINDER HEAD WITH ZTA SPHERES [75] (RIGHT)

The designers claim this workpiece looking similar to a real industrial product can be used as a sensitive verification tool for checking the entire measurement process of industrial CT measurements for a given product [74].

To investigate especially the CT metrology capacities for multi-material objects, this calibrated object has been extended with three ZTA spheres (Zirconia Toughened Alumina) [75]: see *Figure* 23. The study illustrates the benefits of using reference standards embodying complex features also for the application multi-material analysis.

This object can be applied for dimensional measurement as well as defect detection with CT, within one single calibrated object. This test piece is especially suited for measuring real industrial geometries and casting-defects with CT systems [76].

2.6 MODULAR TEST PART

The modular test parts, shown in *Figure 24*, are specifically designed for evaluating the metrological performance of CT systems. The motivation in developing the test parts was to individually quantify different types of CT-induced measurement errors and their influence on the measurement results [77].

FIGURE 24: 2 MODULAR TEST PART SETS IN POLYOXYMETHYLENE AND ALUMINUM ALLOY [77]

2.7 MICRO FIBER GAUGE

An advantage of Computed Tomography (CT) is the coordinate measurement capability of small inner structures, which are not accessible with classical measurement techniques. Measurements of parts with sizes of a few millimeters are feasible [78, 79].

However, also for micro parts challenges regarding traceability, uncertainty estimation and standardization still are existent [80, 81].

Therefore, scanning and measuring of micro parts, ask for dedicated calibrated objects. Marinello presents a new concept of micro-artefact, the fiber gauge, consisting of a set of optical fibers sticking out from a flat surface: *Figure 25* [82]. Carmignato presents, based on this object, a procedure for determining the length measurement errors of X-ray microtomography systems [83].

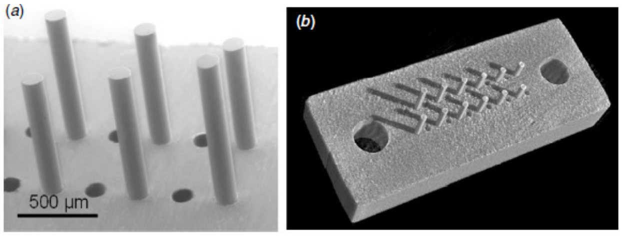

FIGURE 25: MICRO FIBRE GAUGE WITH CYLINDERS ARRANGED IN TWO ROWS [83]

2.8 CT AUDIT

In the frame of the first Interlaboratory Comparison of Computed Tomography Systems for Dimensional Metrology, four objects have been presented as verification objects for the evaluation of different hardware systems and measurement procedures [71].

Another CT intercomparison was organized by DTU (Denmark). Two different object (one plastic and one metallic part) – see last two objects in table on next pages – were presented aiming to collect information about measurement performance in state-of-the-art industrial X-ray Computed Tomography (CT) [84].

2.9 CONCLUSION

Based on all the information above, an overview of the existing verification objects for rescaling and edge correction is presented below. From this table, it can be seen most objects are designed to do either rescaling or edge detection. An object suitable for both, voxel size and edge correction, was still missing at the time the ‘cactus end gage’ was presented. Besides the “sphere forest” presented by Frank Welkenhuyzen of our group and the Lego brick introduced recently in the last CT audit, no object was suitable to perform both tasks (rescaling and edge correction). In the next chapter the ‘cactus end gage’, especially designed to fill this gap will be presented. Remark: Now, also other objects are suitable for performing both tasks (e.g. panflute, …) provided that they are made of the material of interest.

Picture	Material	E/S	Ed/Sc	Size	Aim / Influence	Paper
E = Conclusions based on real experiments; S = conclusions based on simulations ***Ed = Object used for edge detection; Sc = Object used for scaling (rescaling)***						
	Aluminum	E	Ed	Left: Ø30/20 mm Right: Ø20/10 mm	*Aim: Determining CT threshold*	[61]
	Ceramic spheres	E	Sc	Ø30 mm Distance between spheres: 100 mm	*Aim: Assessment of scale errors* Repeatability over time: 38% of voxel size (39 µm) [62]	[61], [62], [63]
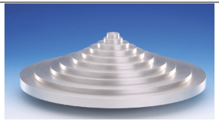	Aluminum	E	Ed	Ø300 mm Height: 200 mm	*Aim: CT system analysis*	[61]
	Aluminum	E	Ed	220 x 220 x 160 mm	*Aim: Testing algorithms for edge detection and data evaluation methods.*	[85]
	Aluminum	E	Ed	100 x 100 x 100 mm	*Aim: Testing algorithms for edge detection and data evaluation methods.*	[85]

Picture	Material	E/S	Ed/Sc	Size	Aim / Influence	Paper
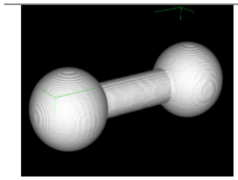	?	E	Sc	?	*Aim: Check influence of detector tilt.* Up to 24% of the voxel size for a detector tilt of 1 pixel.	[35]
		S			*Aim: Check influence of detector exposure time.* The longer the exposure time, the smaller the relative measurement errors. At an exposure time of 400 ms, the results are comparable to a simulation without noise.	
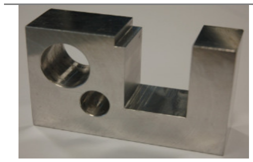	Aluminum	S	Ed	30 x 100 x 60 mm	*Aim:* *-Testing algorithms for edge detection and data evaluation methods.* *- Influence of hardware source prefiltration* ($4\sigma = 1\ \mu m$)	[85] [35]
	Carbon fibre bar, rubin balls	E	Sc	Total length: 8,7678 mm	*Aim: Determining the length measurement property of the CT system.* Repeatability of scaling factor: 30% of voxel size over 8 measurements. (Scanned on different days, including repositioning).	[64]

Picture	Material	E/S	Ed/Sc	Size	Aim / Influence	Paper
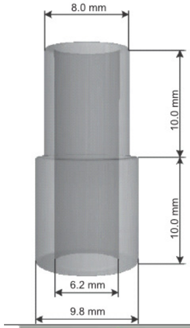	Steel alloy (X20Cr13)	E	Ed	Ø$_{inner}$ 6,2 mm Ø$_{outer,top}$ 8,0 mm Ø$_{outer,bottom}$ 9,8 mm	*Aim: Comparability tests for simulation platform to estimate measurement uncertainty.* Max. 0,05% of voxel size (29,6 µm)	[39]
	27 ruby spheres mounted on carbon shafts	E	Sc	?	*Aim: Test CT hardware stability over time* The test piece was measured 50 times; the deviation from the calibrated value was < $\left(5+\frac{L}{50}\right)\mu m$	[65]

Picture	Material	E/S	Ed/Sc	Size	Aim / Influence	Paper
	Spheres in Al_2O_3, Si_3N_4 en ZrO_2 on carbon fibre rods	E/S	Ed/Sc	Max. distance 105 mm	*Aim: Analyzing the accuracy of single and multi-material CT measurements.* For single material, accuracies up to 10-15 µm are achieved. In the case of multi material this accuracy deteriorates to 70-80 µm.	[66]
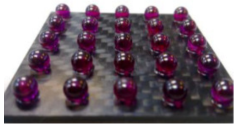	25 ruby spheres on carbon plate	E	Sc	Distance between spheres 10 mm	*Aim: Investigating influence of image quality (spatial resolution and pixel noise) on the measuring errors in a CT system.* Spatial resolution is dominant factor. Sphere distance errors up to ± 30 µm (voxel size 28 µm). *Aim: Metrological performance testing of industrial CT systems.* Sphere distance errors up to ± 12µm, depending on workpiece orientation.	[68] [67]

Picture	Material	E/S	Ed/Sc	Size	Aim / Influence	Paper
Calotte plate 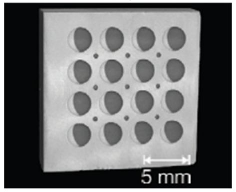	Zerodur calotte plate	E	Ed	Ø 3 mm calottes 20 x 20 mm	*Aim: Used to check sphere distance errors, errors in sphere diameters, probing errors and to correct measurement errors.* Length measurement error of 0,5%. Residual calotte distance errors (after scaling correction) of ±6,5 µm (is 50% of voxel size of 30 µm)	[69]
Calotte cube 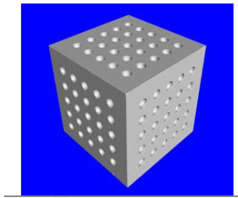	Titanium	E	Ed	10 x 10 x 10 mm	*Aim: Checking influence of data filtering on dimensional measurements with CT.* *Aim: Examining and discussing accuracy and traceability of CT dimensional measurements (CT audit).*	[70] [71]
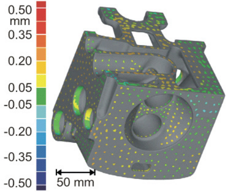	Aluminum	E	Ed	150 x 160 x 170 mm	*Aim: To compare different CT system performances.*	[69]

Picture	Material	E/S	Ed/Sc	Size	Aim / Influence	Paper
CT Tetrahedron 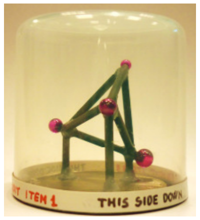	Ruby spheres on carbon fibre frame	E	Sc	Diameters 3-5 mm Distances 25 mm	*Aim: Examining and discussing accuracy and traceability of CT dimensional measurements (CT audit) – measuring sphere diameters and distances between spheres.* Mean error on distance EL: 52,2 µm Mean error on diameter ED: 18,1 µm	[71]
Pan flute gauge 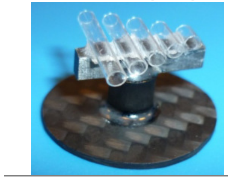	Glass tubes on a carbon fibre frame	E	Ed	Length tubes 2,5 - 12,5 mm $Ø_{inner}$ 1,5 mm $Ø_{outer}$ 1,9 mm	*Aim: Examining and discussing accuracy and traceability of CT dimensional measurements (CT audit) – measuring tube lengths and (inner and outer) diameters.*	[71]
QFM cylinder 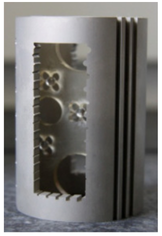	Titanium cylinder with sapphire balls	E		Height 80 mm $Ø_{inner}$ 40 mm $Ø_{outer}$ 50 mm 4 mm spheres	*Aim: Examining and discussing accuracy and traceability of CT dimensional measurements (CT audit) – measuring diameters and sphere distances.*	[71]

Picture	Material	E/S	Ed/Sc	Size	Aim / Influence	Paper
Micro tetrahedron 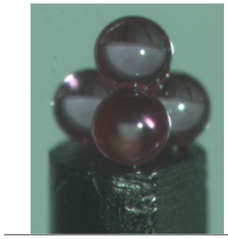	4 ruby spheres	E	Sc	Sphere diameter 0,5 mm	*Aim: Verification, error assessment and correction.*	[75]
Mini-cylinder head segment 	Cylinder head in aluminum, ZTA (Zirconia Toughened Alumina) spheres	E	Ed	Diameter ZTA spheres 6,1 mm	*Aim: Study properties of CT measurements of complex freeform multi-material objects.* Deviations on sphere diameters in the order of 70% of the voxel size (voxel size 54 µm) are measured.	[74], [75]
					Aim: Testing casting-defects and geometry in one scan.	[76]
Micro fibre gauge 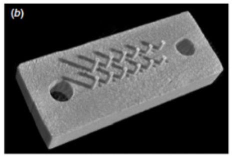	Glass fibres	E	Ed	Fibre diameters 125 µm	*Aim: Correction of systematic errors.*	[83]

Picture	Material	E/S	Ed/Sc	Size	Aim / Influence	Paper
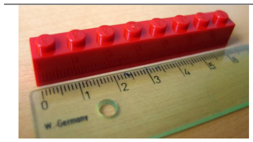	Polymer	E	Ed/Sc	Length 56 mm	*Aims: Test applicability of CT for measurements on small, industrial objects.* *Evaluation of impact of instrument settings and operator decisions on the measurements.* *Investigation of measurements errors and their causes.* *Collect and share knowledge on traceability of measurements using industrial CT.*	[84]
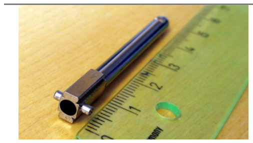	Metal	E	Ed	Length 46 mm		[84]

3. MEASUREMENT UNCERTAINTY

3.1 TRACEABILITY

A dimensional measurement is traceable if the result of a measurement can be referred to the SI unit of length, the unit length meter. In practice, traceability means the ability to define a valid statement about the measurement uncertainty of the measured value.

Traceability is defined by the BIPM International Vocabulary of Metrology (VIM) [86] (BIPM 2012).

"Traceability is the property of the result of a measurement whereby it can be related to stated references, usually national or international standards, through a documented unbroken chain of comparisons all having stated uncertainties." [86]

Achieving traceability is crucial for all complex measurement techniques. For conventional measuring techniques, such as coordinate measuring machines using tactile probes, traceability can, among others, be achieved using model-based uncertainty budgets.

These approaches can as a matter of principle be used to estimate the measurement uncertainty for computed tomography, although entailing difficulties and incompleteness, since the parameters influencing a CT measurement are significantly different compared to other measuring techniques.

At the other hand, a dedicated approach to estimate the measurement uncertainty of a CT measurement, hence a technique to trace back these measurements to the unit of length is indispensable for industrial CT in its process to grow to a measurement technique competing with conventional measuring machines.

3.2 MEASUREMENT UNCERTAINTY

Definition

The definition of measurement uncertainty can be formulated as follows: *"Measurement uncertainty is a non-negative parameter characterizing the dispersion of the quantity values being attributed to a measurand, based on the information used." [86]*

Measurement uncertainty for dimensional computed tomography comprises many components. If a series of measurements can be performed, resulting in quantitative values, the uncertainty can be evaluated by calculating the standard deviation of the statistical distribution of the measured values (Type A evaluation). Other components can be evaluated by experience or other information (Type B evaluation).

Standardization

To evaluate measurement uncertainty, international standards and guidelines have been established. For CT for non-destructive testing (NDT) international standards are available (e.g. ISO 15708). However, the requirements on dimensional CT are different from NDT.

While ISO is working on acceptance and verification tests for CMM with a CT sensor, the only available guideline for uncertainty determination specific for dimensional computed tomography measurements is the VDI/VDE 2630 part 2.1 [87].

Since for many years internationally standardized procedures on error and uncertainty quantification were not available, existing standards for conventional measuring machines are still often 'translated' to applications for industrial computed tomography [88, 89].

Performing many CT scans is very time consuming. Schmitt et al. [90] have therefore suggested applying ISO TS 14253-2 [91] for dimensional CT measurements and they partially minimized the analysis effort by means of simulations. [90] describes how simulations can be used to investigate the effect of random errors on the measurement result of bore holes. For the proposed test part the elaborate experimental effort to define the expanded measurement uncertainty can be reduced by partially relying on simulations for certain influencing factors, but the results are not transferrable to workpieces of other size, shape and material.

Uncertainty evaluation

Franz et al. [92], Härtig and Krystek [93], and Hiller and Reindl [94] estimate measurement uncertainty using simulations. Others use calibrated workpieces to estimate measurement uncertainty [95, 96, 97, 98]

Although simulations of CT measurements can limit the effort for the time consuming measurements needed to estimate the measurement uncertainty, up to now, none of the presented works using simulations is including all influencing factors and is validated to real measurements by a sufficient number of simulations.

Besides applying standards for conventional measuring machines to CT machines, other means to verify the accuracy of CT systems for metrology applications are employed [99]. Comparing different CT measurements or the CT measurement with another reference measurement instrument is often used [57, 100, 101].

4. OBJECTIVES AND SCOPE OF THE THESIS

Being able to define the measurement uncertainty is indispensable for dimensional metrology. Computed Tomography is characterized by two main uncertainty contributors: the rescaling of the voxel size, and the determination of the edge between the workpiece and the background voxels.

In uncertainty determination of conventional measurement instruments, guidelines and standards often refer to calibrated workpieces for uncertainty determination, or to ensure traceability.

The last decade, many verification objects for CT have been presented, but before this work was presented none of the existing objects is capable of estimating both the error on the voxel size and on the edge determination.

Besides the lack of verification objects, also standards and guidelines are still incomplete, or cannot provide a general model to estimate measurement uncertainty coming from both main uncertainty contributors.

This dissertation tries to give an answer to this knowledge gap. The objectives of this thesis can be formulated as follows:

> **Objective 1:** Presenting a verification object which can do both rescaling and edge detection
>
> **Objective 2:** Presenting a conceptual framework for measurement uncertainty determination based on the ISO-GUM for dimensional measurements with Computed Tomography
>
> > *Objective 2.1:* Identifying the different factors contributing to the rescale error, developing a procedure for estimating their contribution to the task-specific measurement uncertainty, and illustrating these contributions by experiments.
> >
> > *Objective 2.2:* Identifying the different factors contributing to edge offsets, developing a procedure for estimating their contribution to the task-specific measurement uncertainty, and illustrating these contributions by experiments.

The first chapter gave an general overview of Computed Tomography (CT), followed by the state of the art on dimensional measurements with CT (Chapter 2). Chapter 3 introduces the 'cactus workpiece', designed to be able to do both rescaling and edge detection and introduces the conceptual framework for uncertainty determination based on the two main contributors.

The next two chapters (Chapter 4 and 5) elaborate on the presented framework for uncertainty determination, zooming in on the estimation of the uncertainty on the voxel size and number of voxels respectively. The two main uncertainty contributors are further subdivided into the different sub-terms out of which these main influences are composed (uniform and non-uniform systematic and random errors).

The last chapter summarizes the main conclusions of this work.

"Every line is the perfect length if you don't measure it."
Marty Rubin

CHAPTER 3: A REFERENCE PART GEOMETRY FOR SIMULTANEOUS DETERMINATION OF SCALE AND EDGE-OFFSET CORRECTION

INTRODUCTION

The two main uncertainty contributors in dimensional metrology with CT are known as the uncertainty on the voxel size and on the edge detection (edge offset).

Before this work was presented, no verification object presented in Chapter 2 was able to be used for both voxel size and edge correction. In this chapter, a verification object 'cactus end gage' is presented.

Based on a series of experimental measurements, it is shown how this object can be used for both error corrections (on the voxel size and on the edge).

Both steps are applied to an industrial workpiece, before giving the conceptual framework for CT uncertainty determination, based on the uncertainty on the voxel size and the number of voxels.

1. TEST OBJECT

1.1 INTRODUCTION OF TEST PART ‘CACTUS END GAGE’

The geometry of the proposed test object is shown in *Figure 26*. This verification object is a prismatic aluminum part (45x45x45mm) with through grooves in the shape of a “cactus”, and is referred to as the ‘cactus end gage’, in analogy of end gages used to calibrate coordinate measuring machines (CMMs). The object is designed to have both internal and external features and edge dependent as well as edge independent distances. The object is subdivided in 8 zones horizontally (numbered from 1 to 8), and 6 zones vertically (numbered from A to F). In zone D, the object has eight internal parallel surfaces mutually separated by 5 mm. The features measured on the test object are the horizontal distances between those surfaces, e.g. distance 1-5, measured in zones C or D.

(A) (B)

FIGURE 26 : FRONT VIEW (A) AND 3D MODEL (B) OF THE TEST OBJECT

The measurement parameters for the test object are summarized in *Table 1* (using a Nikon Metrology 225 CT scanner with Varian 2520 detector).

TABLE 1: MEASUREMENT PARAMETERS FOR THE TEST OBJECT

Measurement parameter	**Value**
Acceleration voltage	180 kV
Tube current	35 µA
Number of projections	3010 (≈ 0,12°/step)
Integration time (exposure)	1000 ms
Physical filter	0.5mm Cu
Focal spot size	± 5µm
Voxel size	39.7 µm

1.2. EDGE DEPENDENT AND EDGE INDEPENDENT DISTANCES

The verification object depicted in *Figure 26* comprises some distances that will be influenced by changing the segmentation/edge detection (edge dependent distances or bidirectional lengths), and other distances that will theoretically not (edge independent distances or unidirectional lengths). This distinction is important for the remainder of the dissertation. For edge independent distances, the measurement result is independent of the chosen grey value for the segmentation between material and the surrounding air or edge offset errors, while still affected by voxel size errors (e.g. *Figure 27* A). For other distances, however, the measurement result is heavily dependent on the edge determination step (e.g. *Figure 27* B), hence a potential edge offset needs to be corrected.

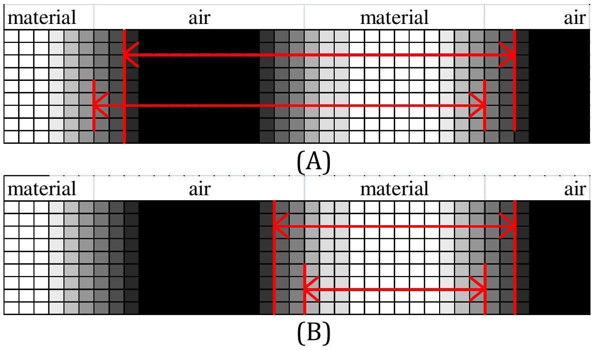

FIGURE 27: DISTANCES CAN BE CLASSIFIED AS EITHER MINIMALLY (A) OR HEAVILY (B) DEPENDENT ON THE EDGE DETECTION

The categorization into *edge dependent* and *edge independent* distances can be made by classifying the surfaces as transitions between Air and Material (AM-type) or vice versa between Material and Air (MA-type).

The test part (cactus end gage) is designed to have different such transitions. Starting from the left hand side of *Figure 27* B, we measure the distance between a MA-type and an AM-type transition, e.g. the width of a groove. Similarly, a distance between an AM-type and a MA-type transition could represent a wall thickness.

2. VOXEL SIZE CORRECTION METHODOLOGY

2.1. INTRODUCTION TO VOXEL SIZE CORRECTION

During the acquisition of the 2D X-ray images, the object is placed between the source and the detector. In analogy with a light source, the closer the object is brought to the source, the bigger will be the (shadow) image on the screen (detector), see *Figure 28*.

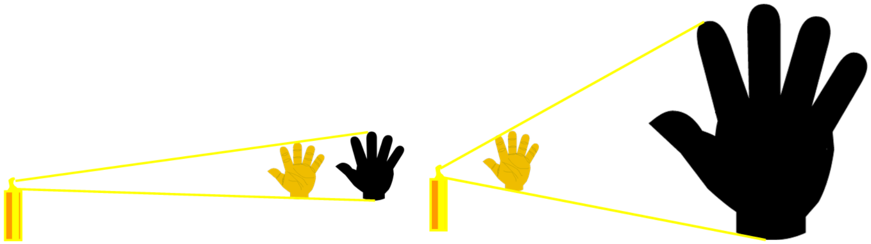

FIGURE 28: INFLUENCE OF POSITION IN THE MACHINE ON MAGNIFICATION

If the position of the workpiece between source and detector is perfectly known, the voxel size is known and a voxel size correction is superfluous. In practice however, this position is never known exactly, asking for a **voxel size correction** step, to correct the voxel size in the 3D CT model. This voxel size correction (determination of the correct magnification factor) can be performed either based on a calibrated length on a separate object, or on the object itself, but should always be based on an edge independent distance (e.g. edge independent distance between two parallel planes as explained in § 1.2 above or distance between two sphere centers that is, by definition, edge independent).

Since the measured length L is determined by the product of the number of voxels n and the voxel size l_x, the voxel size is directly related to the measured value and so a voxel size correction is essential for an accurate CT measurement.

$$\mathrm{L} = \mathrm{n}.\,\mathrm{l_x}$$

where n is a real, positive number, $n \in \mathbb{R}^+$.

2.2. *Voxel size correction methodology*

As stated before, the voxel size correction should be based (preferentially) on an edge independent distance, to avoid over or under scaling the voxel model.

In view of the interdependency of edge detection and voxel size correction described above, the voxel size correction step has been determined as follows:

$$\mathrm{CT}_{\mathrm{i,j}}^{\mathrm{RS}} = \mathrm{CT}_{\mathrm{i,j}} \cdot \frac{\mathrm{CMM}_{,\mathrm{ab}}}{\mathrm{CT}_{\mathrm{a,b}}}$$

where $CT_{i,j}$ represents the distance between plane *i* and plane *j* of the cactus end gage on the original voxel model after edge detection, $CMM_{a,b}$ represents the distance between planes a and b (where b = a+2m with $m \in \mathbb{N}$) measured with a reference measurement instrument (e.g. a tactile CMM), which is also measured in the CT model $CT_{a,b}$. $CT_{i,j}^{RS}$ is the measured distance on the CT model after rescaling. The planes *a* and *b* represent transitions of the same type (AM/AM or MA/MA), and are mutually as remote as possible in order to reduce the influence of random or residual systematic errors on the magnification factor. The longest available distance is preferred for rescaling. In the verification object (cactus end gage), both distances (1,7) and (2,8) are appropriate (see *Figure 26*). In this study, the average of both is used, to minimize the influence of random errors, hence:

$$\mathrm{CT}_{\mathrm{i,j}}^{\mathrm{RS}} = \mathrm{CT}_{\mathrm{i,j}} \cdot \mathrm{average}\left(\frac{\mathrm{CMM}_{1,7}}{\mathrm{CT}_{1,7}}, \frac{\mathrm{CMM}_{2,8}}{\mathrm{CT}_{2,8}}\right)$$

The deviations between the calibrated CT values and the CMM reference values (with Mitutoyo FN905 3D CMM), depicted in *Figure 29*, clearly visualize that the initial edge detection method does not result in a correct edge. Whereas all distances between transitions of the same type (AM/AM or MA/MA) are measured relatively correctly, the distances AM/MA are all too small while the distances MA/AM are too large. In contrast to what was expected, no influence of the height (amount of material to penetrate) could be observed.

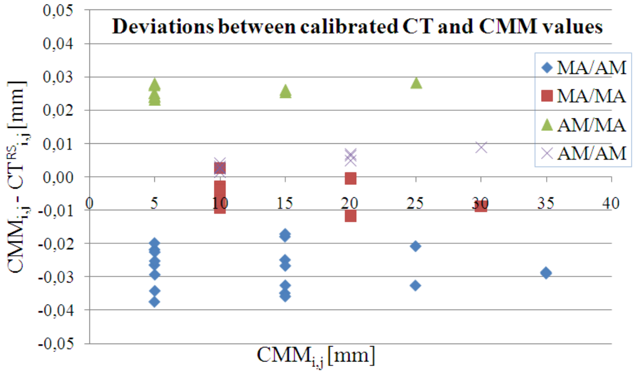

FIGURE 29: DEVIATION BETWEEN RESCALED CT AND CMM VALUES

The edge dependent distances ask, in addition to a voxel size correction, for a correction on the edge. The next section will discuss the edge correction methodology.

3. EDGE CORRECTION METHODOLOGY

3.1. INTRODUCTION TO EDGE DETECTION

Once the voxel size has been corrected, in the following step, in some cases, a **correction on the edge** is necessary. In the software, the edge detection can be performed initially by using a *global or local thresholding* method.

By using a *global thresholding*, one single grey value in between the grey value for the background and the grey value for the material peak, in the histogram representing all voxels of the 3D model, is used as segmentation of the model, e.g. in *Figure 30*. For artefact affected datasets *global thresholding* is yielding no satisfying results [102].

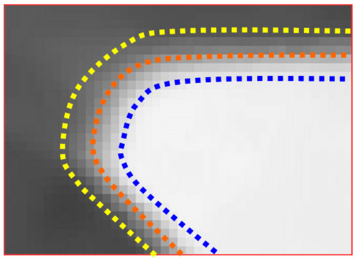

FIGURE 30: EDGE DETECTION

Besides global thresholding, also *local thresholding* techniques exist. These local or advanced edge detection algorithms vary the edge grey value locally to correct for artifacts that influence the measurement. Nevertheless, even for mono-material objects, this advanced thresholding method is often inadequate to find the correct edge. An additional correction step can be used to correct for this wrong edge determination, resulting in an edge correction step.

3.2. EDGE CORRECTION METHODOLOGY

Notice that such edge correction step is not required for all distances, only for edge dependent distances (distances that change with changing the grey value used for the thresholding, e.g. the diameter of a sphere). When an edge is incorrectly defined (wrong grey value), the distance in *Figure 27* B will be either too large or too small, whereas the distance shown in *Figure 27* A will be much less or even not influenced by the threshold grey value.

Figure 29 also led to this conclusion. A correction term for the edge offset in this case can be determined based on the measured deviations.

Hence,

$$\mathrm{CT}_{\mathrm{i,j}}^{\mathrm{Corr}} = \mathrm{CT}_{\mathrm{i,j}}^{\mathrm{RS}} \pm (\mathrm{CMM}_{\mathrm{x,y}} - \mathrm{CT}_{\mathrm{x,y}}^{\mathrm{RS}})$$

Where $CT_{i,j}^{Corr}$ represents the distance between plane *i* and plane *j* with j = i+2m+1 after edge correction. The planes *x* and *y* with y = x+2m+1 represent transitions of different type (AM/MA or MA/AM), and are mutually as close as possible in order to reduce the influence of residual scaling errors on the edge correction term. The sign is positive if both distances *(i,j)* and *(x,y)* are AM/MA or MA/AM and negative otherwise.

In order to reduce the effect of random errors, more than one distance (*x,y*) can be used dependent on the availability of reference data. Considering the appropriate signs, the general formula for using *n* distances is:

$$\mathrm{CT}_{\mathrm{i,j}}^{\mathrm{Corr}} = \mathrm{CT}_{\mathrm{i,j}}^{\mathrm{RS}} \pm \frac{\sum_{\mathrm{k=1}}^{\mathrm{n}} \mathrm{abs}\left(\mathrm{CMM}_{\mathrm{x_k,y_k}} - \mathrm{CT}_{\mathrm{x_k,y_k}}^{\mathrm{RS}}\right)}{\mathrm{n}}$$

Figure 31 provides an overview of the range of correction terms obtained when varying *n* from 1 to 7 of the smallest distances of the test part. For the remainder of this chapter, *n*=7 has been used. This implies a maximum repeatability and independence of the random selection of reference planes. However, it also represents a best-case scenario.

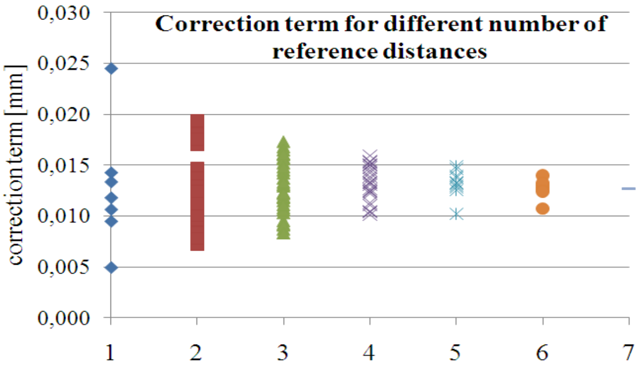

FIGURE 31: INFLUENCE OF THE NUMBER OF REFERENCE DISTANCES ON THE CORRECTION TERM

Figure 31 allows assessing the maximum systematic error that could be introduced when lowering *n*. For example, *n*=1 would entail a maximum additional systematic error of ±12µm (half of the maximum error). Errors after correction (with n=7) are given in *Figure 32*.

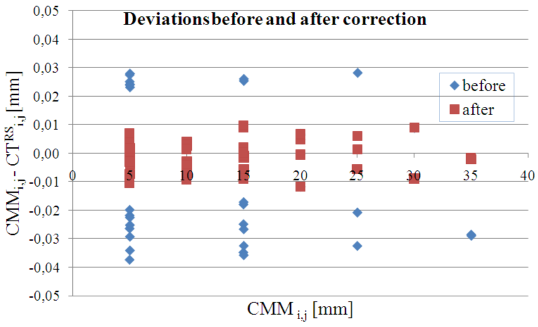

FIGURE 32: COMPARISION OF CALIBRATED CT AND CMM VALUES BEFORE (SAME AS FIGURE 29) AND AFTER CORRECTION (N=7)

4. INFLUENCE OF MEASUREMENT PARAMETERS: X-RAY SOURCE SETTINGS

In this section, the proposed test object is used to quantify experimentally the influence of the X-ray source current and voltage settings within the proposed measurement procedure (indicated at the right on the graphs voltage (in kV) – current (in µA)). Notice that two different physical parts of the test object have been used for the analyses described above and below respectively, which explains small deviations between the reported numerical values.

The settings (voltage and current) to measure a workpiece are user-defined. The voltage needs to be sufficient to penetrate the workpiece, whereas the current determines the contrast of the image. Meanwhile, saturation needs to be avoided.

Between these limits, different combinations of voltage and current have been tested. The values shown in *Figure 33* and *Figure 34* refer to all 5 mm distances between subsequent planes in zone D of the test object.

Figure 33 shows the deviations between the CT-values and the reference CMM-values after rescaling (voxel correction) but before edge correction. The deviation increases with both increased voltage and increased current settings. After edge correction using the distance between planes 4 and 5, however, no more trend can be observed (*Figure 34*). In addition, all deviations are reduced to levels that are comparable to the CMM reference measurement uncertainty. The MPE value of the Mitutoyo CMM used for the reference measurements is (4.2 + 5L*10^{-3}) µm. Notice that the deviation on the distance 4-5 is evidently reduced to zero.

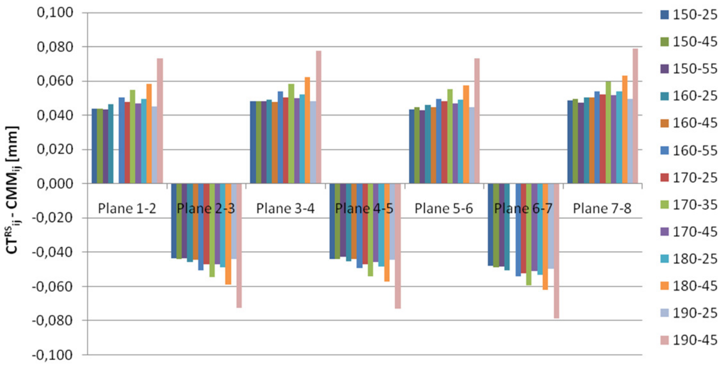

FIGURE 33: DEVIATIONS OF RESCALED CT VALUES **BEFORE EDGE CORRECTION** FROM THE CMM REFERENCE MEASUREMENTS FOR DIFFERENT VOLTAGE AND CURRENT SETTINGS (USING 0,5 MM CU FILTER)

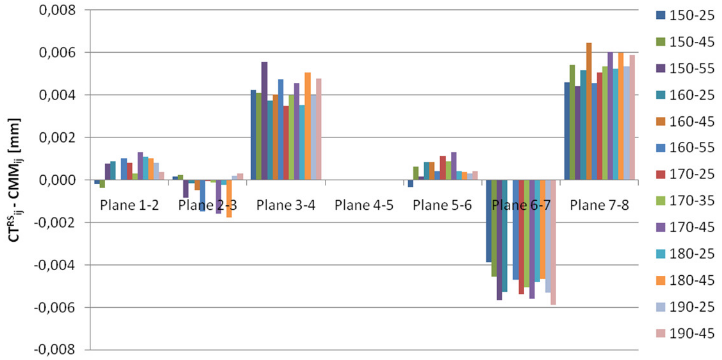

FIGURE 34: DEVIATIONS OF RESCALED CT VALUES **AFTER EDGE CORRECTION** FROM THE CMM REFERENCE MEASUREMENTS FOR DIFFERENT VOLTAGE AND CURRENT SETTINGS (USING 0.5 MM CU FILTER). NOTICE THE SCALE DIFFERENCE WITH FIGURE 33)

5. APPLICATION TO AN INDUSTRIAL OBJECT

To validate this procedure, it was applied on an industrial workpiece, a nozzle manufactured with additive manufacturing by LayerWise (3D Systems) [103], depicted in *Figure 35*.

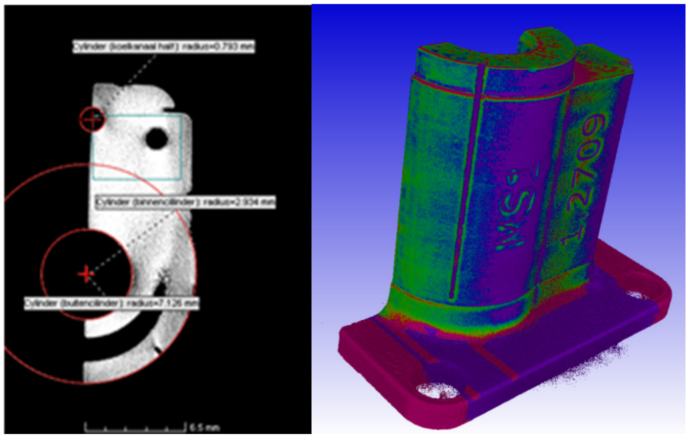

FIGURE 35: CT SLICE AND COMPARISON OF LASER SCANNING MEASUREMENT AND CT MODEL OF INDUSTRIAL WORKPIECE – NOZZLE (PRODUCED BY LAYERWISE-3D SYSTEMS [103])

The measurement results are represented in *Figure 36*, showing in blue the results before correction; i.e. the measurements on the voxel model immediately after reconstruction. After correction for the voxel size (which is dependent on the position of the rotation table between the source and the detector) the result is slightly better for the internal features (but worse for the outer distance). The voxel size correction factor was calculated based on the measurement of the sphere center distance of two spheres on a separate object, scanned just before the measurement of the nozzle.

Afterwards, an edge correction is performed based on a reference measurement of thickness of the straight part (on top in *Figure 35* at the left) on a CMM (Mitutoyo FN905 3D CMM) with a laser scanner probe. This workpiece was measured with a laser scanner, instead of a tactile probe because of the complex shape of this object. The edge dependent distance used for the correction was the distance between the left and right side of the rectangular part of object (on the top, in *Figure 35*, left). After edge correction, the accuracy improves significantly, showing the strength of this method.

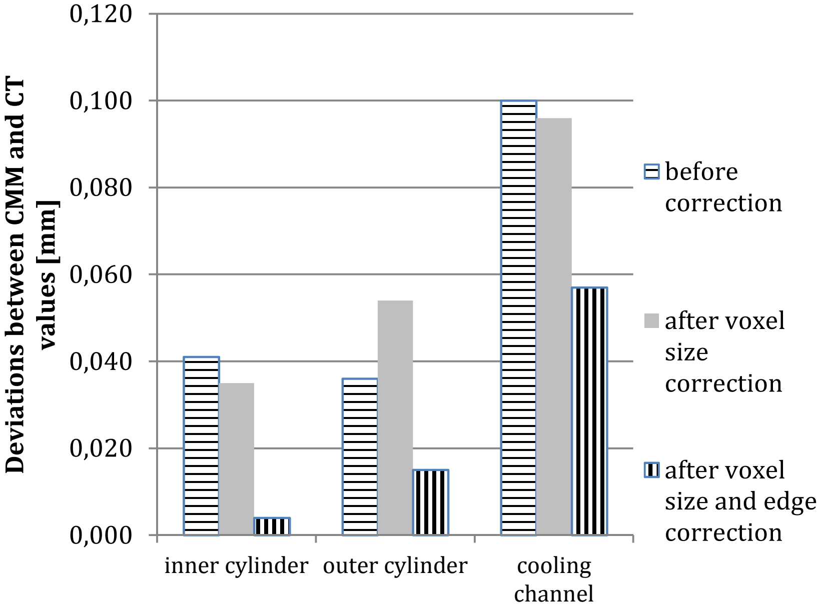

FIGURE 36: MEASUREMENT RESULTS INDUSTRIAL WORKPIECE – NOZZLE

6. PRESENTED FRAMEWORK FOR CT MEASUREMENT UNCERTAINTY EVALUATION

This section will zoom in on the proposed framework for measurement uncertainty determination in CT metrology, based on a GUM-based analytical uncertainty equation, including all possible CT related effects on the CT measurement.

Starting from the basic equation to describe the measurement result of a CT measurement, this procedure allows to include, identify and quantify every single CT related uncertainty contributor and can be applied to every workpiece (not limited to academic test parts).

Since a CT model is a voxel model, the result L of a CT dimensional measurement can basically be interpreted as the product of the number of voxels $n \in \mathbb{R}^+$ and the voxel size l_v. It is important to emphasize that n not necessarily represents an integer, since intra-voxel interpolation is used for edge detection to cope with partial volume effects.

$$L = n \cdot l_v \tag{1}$$

Based on this equation, it becomes clear the uncertainty on the measured length is determined by the uncertainty on the voxel size and the uncertainty on the number of voxels.

Starting from this equation, the combined standard uncertainty u_L on the measured length L can be calculated according to the Guide to the Expression of Uncertainty in Measurement GUM [101], based on

$$u_L^2 = \sum_{i=1}^{N} \left(\frac{\partial L}{\partial x_i}\right)^2 \cdot u_{x_i}^2 + 2 \sum_{i=1}^{N-1} \sum_{j=i+1}^{N} \left(\frac{\partial L}{\partial x_i}\right)\left(\frac{\partial L}{\partial x_j}\right) u(x_i, x_j) \tag{2}$$

Applying (2) on (1) yields

$$u_L^2 = n^2 \cdot u_{l_v}^2 + l_v^2 \cdot u_n^2 + 2 \cdot n \cdot l_v \cdot u(n, l_v) \tag{3}$$

where the input quantities x_i with associated uncertainty u_{x_i} are supposed to be uncorrelated, i.e. having a covariance $u(n, l_v) = 0$, which reduces (3) to

$$u_L^2 = l_v^2 \cdot u_n^2 + n^2 \cdot u_{l_v}^2 \tag{4}$$

where u_{l_v} is the uncertainty on the voxel size (determined by the rescaling) and u_n is the uncertainty on the number of voxels (related to the edge detection).

Equation (4) emphasizes that the uncertainty on the measured length L consists of two terms, caused by respectively the uncertainty on the voxel size and the uncertainty on the edge detection. Both uncertainty contributors can be further subdivided into uniform and non-uniform systematic and random errors, as illustrated in the next two chapters.

Chapter 4 will elaborate on the different sub-terms, which are together responsible for the uncertainty on the voxel size.

Chapter 5 will zoom in on the different sub-terms determining the uncertainty on the number of voxels.

7. CONCLUSIONS

This chapter introduced the main steps of a CT measurement procedure, focusing on the voxel size correction and edge detection steps. These concepts were explained based on a verification object (cactus end gage), designed for this purpose. It allows to correct for scale errors (voxel correction) as well as for offset errors (edge correction). Unlike other verification methods that use different reference objects made from different materials (e.g. ceramic ball bar for scaling and aluminum bush for thresholding), a single reference part was proposed here for both, allowing scaling and thresholding correction to be performed with a single material object with the same properties as real workpieces. Furthermore, the workpiece allows to measure internal as well as external reference measurements.

It was shown that the proposed rescaling and edge correction method significantly improves the accuracy of the measurements for the proposed test object. The correction method also works for an industrial workpiece, although the remaining errors are bigger, due to other influencing factors. By investigating the influence of the X-ray source settings it became clear that machine setting influences (current and voltage) are largely compensated for in the proposed verification procedure.

This chapter concludes with the conceptual framework for CT uncertainty determination, based on the uncertainty on the voxel size and the number of voxels. In the next two chapters, these two main uncertainty contributors will be subdivided into different sub-factors, and the method will be illustrated based on experimental data on two ball plates.

"An optimist will tell you the glass is half-full; the pessimist, half-empty; and the engineer will tell you the glass is twice the size it needs to be"

CHAPTER 4: MEASUREMENT UNCERTAINTY - UNCERTAINTY ON THE VOXEL SIZE U_{L_V}

INTRODUCTION

As presented in the previous chapter, the conceptual framework for CT measurement uncertainty, based on the ISO-GUM starts from the product of the voxel size and the number of voxels as the description of every CT measurement. The first uncertainty contributor is further subdivided in this chapter into an uncertainty contributor due to random errors and on uniform and non-uniform systematic errors.

Since the uncertainty on the voxel size is strongly dependent on the measurement procedure, this chapter starts, after an introduction of the presented workpiece for the estimation of the uncertainty on the voxel size, with an overview of the typical CT measurement procedures.

Based on different measurements, the uncertainty on the voxel size and the different subcategories are illustrated and quantified in this chapter.

1. DESCRIPTION OF THE WORKPIECE

Most concepts and methods captured in this chapter are illustrated based on the same workpiece, a carbon fibre plate with 25 ruby or steel spheres. Carbon fibre plate and ruby spheres minimize scatter artefacts because of their low densities and shape; using 25 spheres allows to measure a lot of distances (of different length) in one scan. A picture of the plate with the ruby spheres, can be found in *Figure 37*. The ball plates both consist of 25 spheres in 5 rows and 5 columns at about 10 mm interdistance. Several center point distances are defined. The numbering of the spheres and distances is included in the schematic representations of the plates (in *Figure 38* till *Figure 40*).

- 2 long distances include both diagonals (sphere 1-25 and sphere 5-21)
- 10 middle-long distances consist of the distance between sphere 1-5, 6-10, … and 1-21, 2-22, …
- 40 short distance include all horizontal and vertical distances between two adjacent spheres.
-

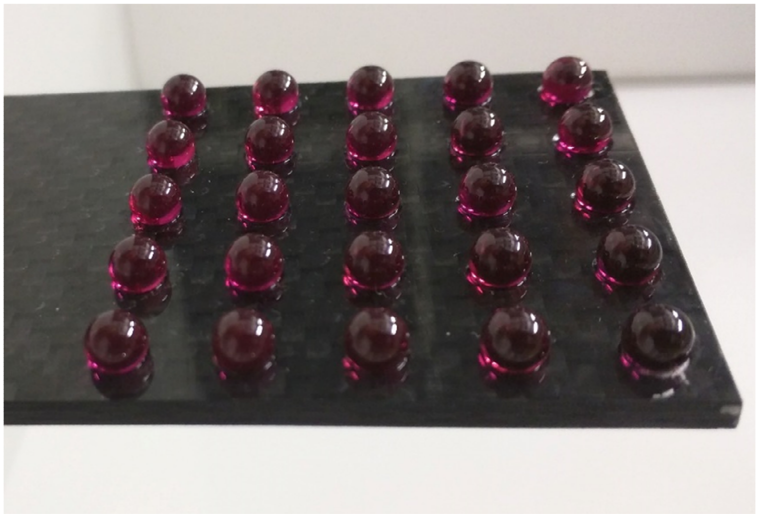

FIGURE 37: PICTURE OF RUBY BALL PLATE

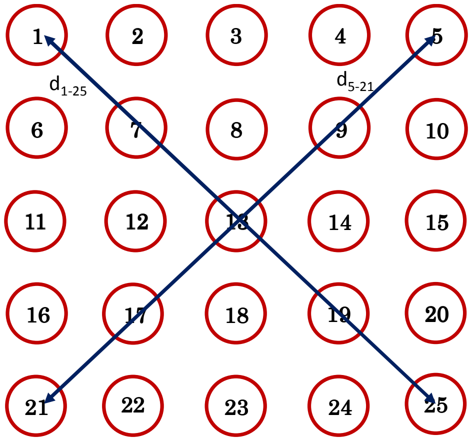

FIGURE 38: SCHEMATIC REPRESENTATION OF BALL PLATE, INCLUDING NUMBERING OF DIAGONALS

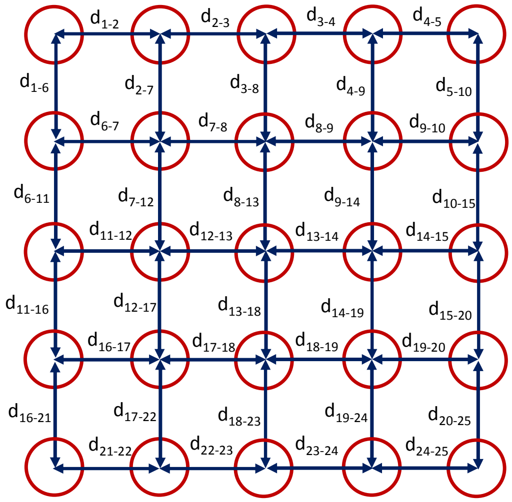

FIGURE 39: SHORT DISTANCES (40)

In the graphs, the 40 small center point distances are numbered according to the table below (*Table 2*).

TABLE 2: NUMBERING SHORT DISTANCES IN GRAPHS

d_{1-2}	1	**d_{13-14}**	11	**d_{1-6}**	21	**d_{13-18}**	31
d_{2-3}	2	**d_{14-15}**	12	**d_{6-11}**	22	**d_{18-23}**	32
d_{3-4}	3	**d_{16-17}**	13	**d_{11-16}**	23	**d_{4-9}**	33
d_{4-5}	4	**d_{17-18}**	14	**d_{16-21}**	24	**d_{9-14}**	34
d_{6-7}	5	**d_{18-19}**	15	**d_{2-7}**	25	**d_{14-19}**	35
d_{7-8}	6	**d_{19-20}**	16	**d_{7-12}**	26	**d_{19-24}**	36
d_{8-9}	7	**d_{21-22}**	17	**d_{12-17}**	27	**d_{5-10}**	37
d_{9-10}	8	**d_{22-23}**	18	**d_{17-22}**	28	**d_{10-15}**	38
d_{11-12}	9	**d_{23-24}**	19	**d_{3-8}**	29	**d_{15-20}**	39
d_{12-13}	10	**d_{24-25}**	20	**d_{8-13}**	30	**d_{20-25}**	40

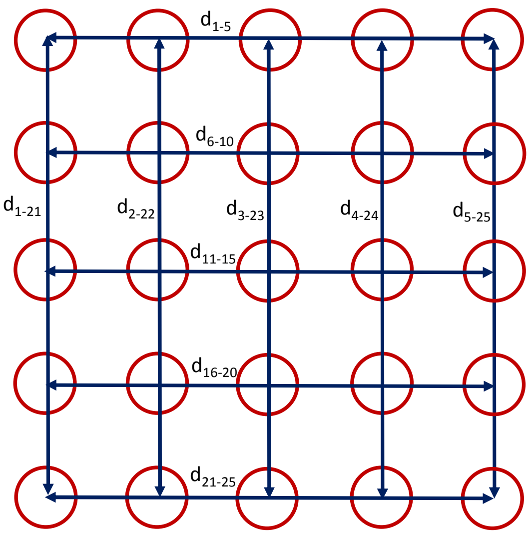

FIGURE 40: MIDDLE LONG DISTANCES (10)

The numbering of the middle-long distances in the graphs is according to *Table 3*.

TABLE 3: NUMBERING OF THE MIDDLE-LONG DISTANCES

d_{1-5}	1	**d_{1-21}**	6
d_{6-10}	2	**d_{2-22}**	7
d_{11-15}	3	**d_{3-23}**	8
d_{16-20}	4	**d_{4-24}**	9
d_{21-25}	5	**d_{5-25}**	10

The ball plates are measured with the following settings (*Table 4*):

TABLE 4: MEASUREMENT SETTINGS BALL PLATE MEASUREMENTS (USING A NIKON METROLOGY XTH 225ST CT SCANNER)

PARAMETERS	**CHOSEN SETTINGS**	
	Ruby	***Steel***
# PROJECTIONS	720	720
THRESHOLDING	ISO 50% + adv. mode	ISO 50% + adv. mode
HARDWARE FILTER	0,1 mm Cu filter	1 mm Cu filter
BEAM HARDENING CORRECTION	None	None
VOLTAGE	130 kV	220 kV
CURRENT	180 µA	110 µA

2. SOURCES OF UNCERTAINTY ON THE VOXEL SIZE

The voxel size l_v is determined primarily by the position of the rotation stage with the workpiece between X-ray source and detector. An evident contributor to the uncertainty on the voxel size l_v stems from errors on the magnification axis. Incorrect positioning of the rotation stage along the magnification axis results in a uniform magnification error over the entire voxel space.

To illustrate this, the workpiece (with steel spheres) described in Section 1 of this Chapter was measured 6 times, at 6 different positions on the magnification axis (150, 219, 318, 419, 519 and 600 mm). All 40 short distances were determined with the software VGStudio MAX, and plotted in *Figure 41*. The workpiece was tilted over about 35 degrees during scanning, such that sphere number 1 was at the top.

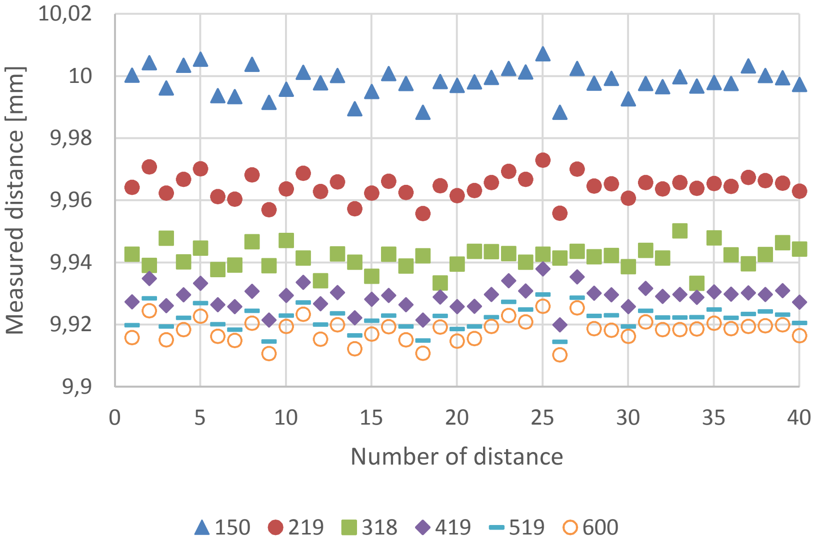

FIGURE 41: RESULTS OF 40 SHORT BALL DISTANCES AT 6 DIFFERENT MAGNIFICIATION POSITIONS

From *Figure 41*, it is clear that the magnification axis is not calibrated correctly. For this reason, a correction of the voxel size is mandatory. How this correction can be applied will be explained in this chapter.

Verification and compensation steps can minimize the systematic component of this magnification-axis related error, yet uncertainties will remain.

Since the uncertainty components are inherently dependent on the applied measurement procedure, three procedures will be used to illustrate the forthcoming discussions. **Procedure 1** concerns scanning an object for voxel size correction together with the workpiece on the rotation stage of the CT device or using an edge independent distance on the workpiece itself to rescale. **Procedure 2** involves scanning both separately yet consecutively without changing the position of the rotation stage. **Procedure 3** concerns periodic (e.g. monthly) verification using the same type of artefact (illustrated in *Figure 42*).

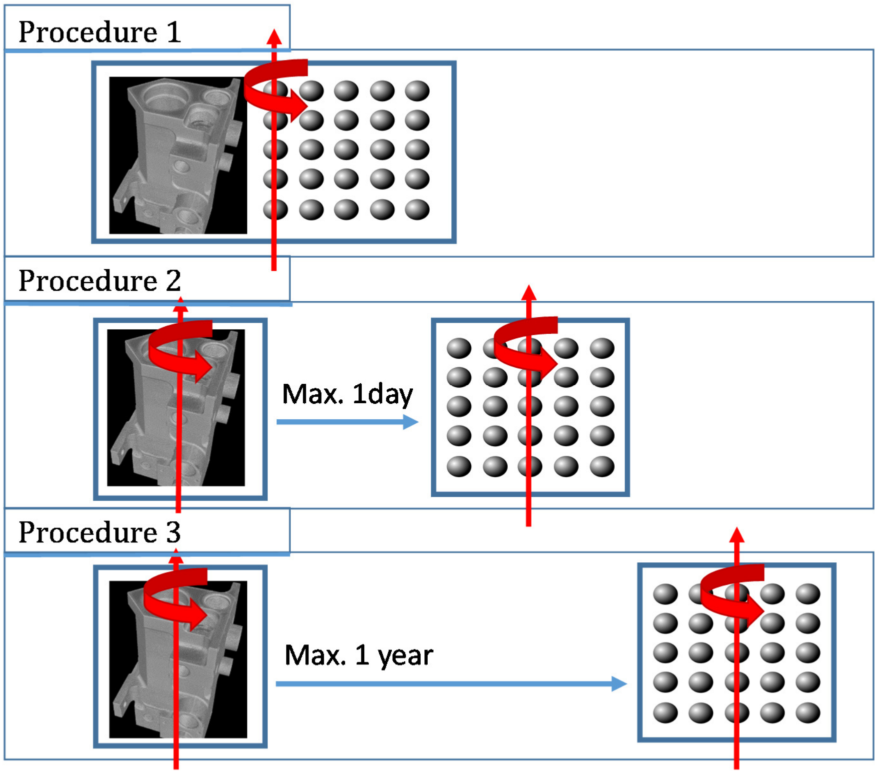

FIGURE 42: PROCEDURES 1-3

Notice that the described concepts can be used mutatis mutandis for other verification procedures.

In each case, the voxel size is determined by the ratio of the reference measurement of a rescaling length (e.g. the distance between the center points of two spheres, which will be used in most cases in this dissertation) and the number of voxels representing this verification length on the CT model:

$$\mathrm{l_v} = \frac{\mathrm{L_{cal}}}{\mathrm{n_{cal}}}$$

$\mathrm{L_{cal}}$ represents the calibrated distance between both sphere center points and $\mathrm{n_{cal}} \in \mathbb{R}^{+}$ the number of voxels between both sphere center points on the voxel model of the verification object. In general, the combined standard uncertainty $\mathrm{u_{l_v}}$ on the measured length $\mathrm{l_v}$ can be calculated according to the GUM [101], based on (1), where the input quantities $\mathrm{x_i}$ with associated uncertainty $\mathrm{u_{x_i}}$ are supposed to be uncorrelated, i.e. all covariances = 0:

$$\mathrm{u_{l_v}^2} = \sum_{\mathrm{i=1}}^{\mathrm{N}} \left(\frac{\partial \mathrm{l_v}}{\partial \mathrm{x_i}}\right)^2 \cdot \mathrm{u_{x_i}^2} \tag{1}$$

The uncertainty on the voxel size is thus:

$$\mathrm{u_{l_v}^2} = \left(\frac{1}{\mathrm{n_{cal}}} \cdot \mathrm{u_{L_{cal}}}\right)^2 + \left(\frac{1}{\mathrm{n_{cal}}^2} \cdot \mathrm{L_{cal}} \cdot \mathrm{u_{n_{cal}}}\right)^2 \tag{2}$$

which can be rewritten as :

$$\frac{\mathrm{u_{l_v}^2}}{\mathrm{l_v^2}} = \frac{\mathrm{u_{L_{cal}}^2}}{\mathrm{L_{cal}^2}} + \frac{\mathrm{u_{n_{cal}}^2}}{\mathrm{n_{cal}^2}}$$

In the following discussion, $\mathrm{u_{n_{cal}}}$ will be further subdivided into a random component $\mathrm{u_{n_{cal,random}}}$, and a systematic component $\mathrm{u_{n_{cal,sys}}}$, which is further subdivided in a uniform and a non-uniform component $\mathrm{u_{n_{cal,sys,uniform}}}$ and $\mathrm{u_{n_{cal,sys,non-uniform}}}$, which can be root-sum-squared to yield $\mathrm{u_{n_{cal}}}$.

$$\frac{\mathrm{u_{l_v}^2}}{\mathrm{l_v^2}} = \frac{\mathrm{u_{L_{cal}}^2}}{\mathrm{L_{cal}^2}} + \frac{\left(\mathrm{u_{n_{cal,random}}^2} + \mathrm{u_{n_{cal,FPE}}^2} + \mathrm{u_{n_{cal,non-uniform}}^2}\right)}{\mathrm{n_{cal}^2}}$$

The following sections elaborate on $\mathrm{u_{L_{cal}}}$ (the uncertainty on the verification length, Section 3), $u_{n_{cal,random}}$ (the uncertainty on the repeatability of the voxel size determination, Section 4), and $u_{n_{cal,sys}}^2$ (the uncertainty due to systematic errors, Section 5 and Section 6 for the non-uniform and uniform term respectively).

3. $U_{L_{CAL}}$: THE UNCERTAINTY ON THE VERIFICATION LENGTH

The uncertainty $u_{L_{cal}}$ is the uncertainty on the reference measurement of the verification length (*Figure 43*) performed using a conventional (reference) measurement instrument, such as a CMM (Coordinate Measuring Machine) or an Abbe comparator. It can be determined based on the available standards for the reference measurement instrument used (e.g. on the MPE of the instrument determined according to ISO 10360), and is equal for all verification procedures described.

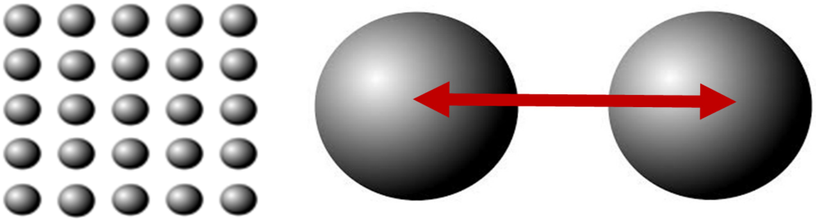

FIGURE 43: TEST OBJECT WITH CALIBRATED SPHERES

All lengths have been measured using a conventional tactile coordinate measuring machine (CMM) Mitutoyo FN-905. The maximum permissible error (MPE) of 4,2 micrometer + 5 micrometer/meter is used to estimate the standard uncertainty on the reference measurement (type B error).

Since there is no specific knowledge about the possible values within the interval between the upper and lower limits, it can only be assumed it is equally probable for L_{cal} to lie anywhere within it; a uniform or rectangular distribution of possible values is assumed [101]. Calculating the uncertainty for the longest distance between two spheres on the ball plate (±50 mm) in that case yields $u_{L_{cal}} = \frac{4{,}2\ \mu m + \frac{5}{20}}{\sqrt{3}} = 2{,}60\ \mu m$. Hence, for a short distance of ±10 mm the use of this verification object implies $\frac{4{,}2\ \mu m + \frac{5}{100}}{\sqrt{3}} = 2{,}45\ \mu m$ or $0{,}245\ \mu m$ of uncertainty per mm length of the measurand.

Accurate manufacturing or a more accurate reference measurement of the rescaling object can allow reducing this term to very small values.

Errors stemming from temperature influences can easily be incorporated in this discussion by realizing that uniform expansions of either workpiece or verification object correspond to the use of an inadequate calibrated length, hence inducing uniform voxel size errors.

4. $U_{N_{CAL,RANDOM}}$: THE UNCERTAINTY ON THE REPEATABILITY OF THE VOXEL SIZE DETERMINATION

Even when utilizing a rescaling object with negligible uncertainty, voxel size correction bears inherent uncertainties. A random error contribution to the uncertainty on the voxel size concerns the repeatability of the verification measurement. The repeatability of the number of voxels representing the distance between two adjacent marked spheres of the set-up depicted in Figure 37 is different for the different measurement procedures.

4.1 $u_{n_{cal,random}}$ USING PROCEDURE 1

In **Procedure 1**, where the rescaling object is measured together with the measured object (workpiece), the repeatability is limited to the repeated observations in VGStudio MAX on the same voxel model. The differences are often hardly noticeable. Measuring a certain sphere distance ten times in the software, yield ten times exactly the same value, up to 1 nm.

Two distances were calculated 5 times in the software VGStudio MAX, for both the sphere plate with ruby and steel spheres. The measurement settings are listed in *Table 4*. A short distance (the distance between sphere 15 and 16) in the middle of the plate, and a middle long distance (the distance between sphere 1 and 5) at one side of the plate were measured.

All four results yield 5 times exactly the same result. The results are summarized in Table 5.

TABLE 5: RESULTS OF REPEATABILITY OF SPHERE DISTANCES IN VOLUME GRAPHICS

	DISTANCE SPHERE 15-16	**DISTANCE SPHERE 1-5**
RUBY PLATE	10,00130 mm	40,00470 mm
STEEL PLATE	9,86802 mm	40,04380 mm

This result is confirmed many times with different, but similar objects. In each case, 5 observations of the distance between the spheres in the software gives 5 times exactly the same result, up to less than 1 nm. The workpieces used, and the measurement settings are listed in *Table 6*.

TABLE 6: WORKPIECES AND MEASUREMENT SETTINGS ILLUSTRATION REPEATABILITY ON VOXEL SIZE FOR PROCEDURE 1

Row of steel **spheres**	
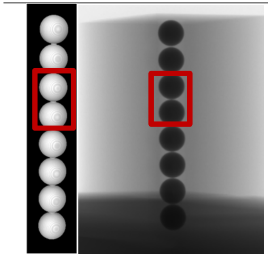	**Measurement settings:** 150 kV – 65 µA ISO50% - Local thresholding No hardware filter No beam hardening correction Magnification position 330 1000 projections
2 ruby **spheres**	
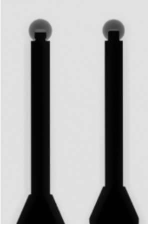	**Measurement settings:** 70 kV – 50 µA No ISO50% - Local thresholding No hardware filter No beam hardening correction Magnification position 330 1000 projections
Plastic **spheres enclosed in light foam**	
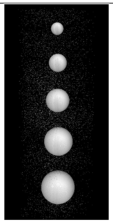	**Measurement settings:** 55 kV – 100 µA No ISO50% - Global thresholding No hardware filter No beam hardening correction Magnification position 200 1000 projections

The ISO50% value could not be used for the last to cases in *Table 6*, because of the differences in density between the steel pins and ruby spheres and the plastic spheres and surrounding foam respectively, however, this has no impact on the repeatability.

Even for plastic spheres, enclosed in a light foam with a density that is only slightly different from the density of the spheres, the distance measurement between two spheres is repeatable up to 1 nm, for good measurement conditions.

Procedure 1 implies scanning the workpiece and the rescaling object in one measurement. The material of the rescaling object can be chosen such that the measurement settings apply for both the workpiece and the rescaling object. As shown in this paragraph, this will not affect the uncertainty on the repeatability of the voxel size.

The uncertainty $u_{n_{cal,random}}$ is often negligible when Procedure 1 is employed. Using an edge independent distance on the workpiece itself gives – in most cases - higher values for this uncertainty contributor.

4.2 $u_{n_{cal,random}}$ USING PROCEDURE 2

Sometimes, it's impossible to scan the workpiece together with the rescaling object, nor to use a distance on the object itself for rescaling. In these cases, the workpiece and rescaling object are scanned consecutively without changing the position of the magnification axis. The repeatability in procedure 2 is represented by the measurements of the same distance on voxel models reconstructed from different scans that were taken.

During a repeatability test, 5 consecutive scans were made of the object (with steel spheres) described in Section 1 (voxel size 71,9 µm). In between two scans, the position of the magnification axis was not changed. Taking one short distance, in the middle of the plate (distance 12 between sphere 14 and 15), the standard uncertainty $u_{n_{cal,random}} = s(q_k)$ is calculated to be 0,00474 (voxels), see *Figure 44*.

$$s(q_k) = \sqrt{\frac{1}{n-1}\sum_{j=1}^{n}(q_j - \bar{q})^2} = \sqrt{\frac{1}{5-1}\sum_{j=1}^{5}\left(q_j - 134{,}2\right)^2}$$

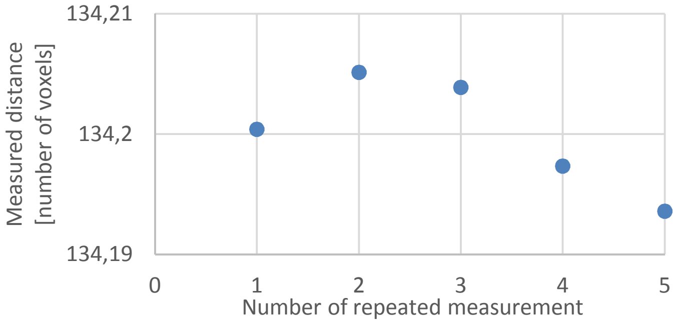

FIGURE 44: REPEATABILITY OF SPHERE DISTANCE OVER 5 CONSECUTIVE MEASUREMENTS OF STEEL BALL PLATE

The standard uncertainty was calculated for each of the 40 short distances and plotted in *Figure 45*. Except for one outlier (distance 40 = the distance between sphere 20 and 25) the uncertainty (defined as 1σ or 1 s and calculated with equation (1)) on the repeatability of the voxel determination is less than 0,01 voxels for a distance of ±135 voxels (±10 mm), when procedure 2 is applied, scanning the rescaling object and workpiece in consecutive scans, without changing the position of the magnification axis.

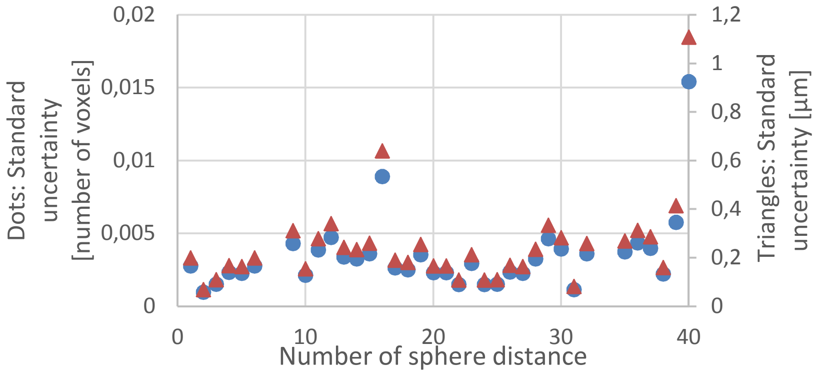

FIGURE 45: STANDARD UNCERTAINTY OF 40 SHORT SPHERE CENTER DISTANCES (DISTANCE 12, SEE FIGURE 44 IN RED)

Three distances have an uncertainty of more than 0,005 voxels (distance 16, 39 and 40). These are the distances between spheres 19-20, 15-20 and 20-25 respectively (see Table 2), all including sphere 20. Probably this has to do with a reference measurement of the position of sphere 20.

The same analysis was repeated at two other positions on the magnification axis. The conclusion is confirmed, as illustrated on *Figure 46*.

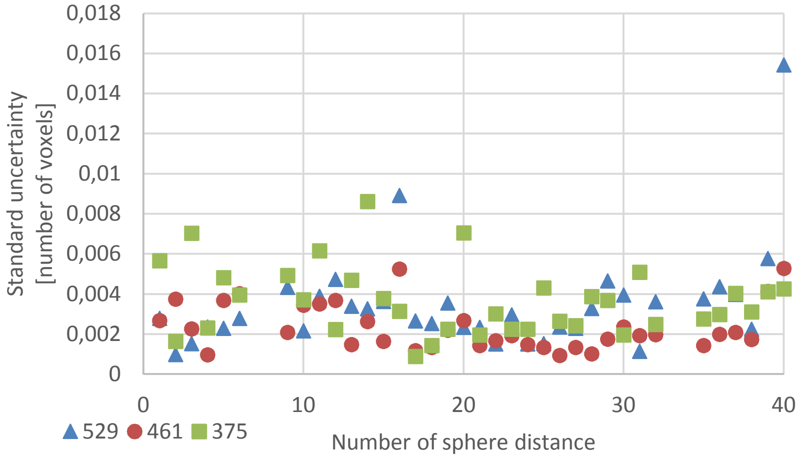

FIGURE 46: STANDARD UNCERTAINTY OF 40 SHORT SPHERE CENTER DISTANCES AT 3 DIFFERENT POSITIONS OF THE MAGNIFICATION AXIS (375, 461, 529)

This experiment was repeated with another rescaling object, which is often used, a row of steel spheres, depicted in *Table 6*, top. The measurement settings are listed in *Table 7*.

TABLE 7: MEASUREMENT SETTINGS UNCERTAINTY ON REPEATABILITY WITH ROW OF STEEL SPHERES

Measurement settings
180 kV – 100 µA
ISO50% - Local thresholding
No hardware filter
No beam hardening correction
Magnification position 170, 240, 350, 500
1000 projections

The results of distance measurements between sphere 3 and 4 (from top to bottom) for the 5 consecutive measurements is given in *Figure 47*. These measurement results result in a standard uncertainty on the voxel size of 0,00366; 0,00920; 0,0137 and 0,00363 voxels for magnification positions 170, 240, 350 and 500 respectively.

Except for the measurement of the row of spheres at magnification position 350, it can be concluded for these experiments the standard uncertainty, characterizing the repeatability for the measurements described here, in this case, is below 0,01 voxel, or less than 1% of the voxel size when procedure 2 is applied.

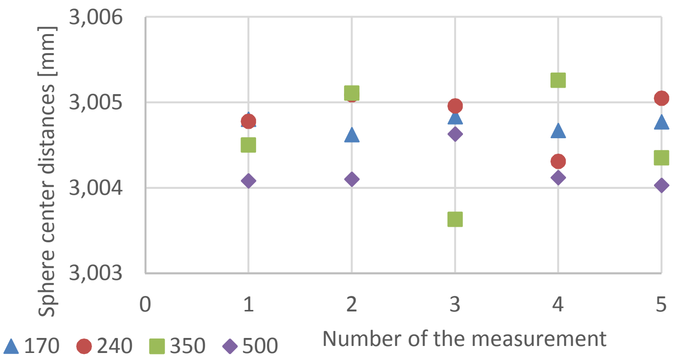

FIGURE 47: REPEATABILITY OF SPHERE DISTANCE OVER 5 CONSECUTIVE MEASUREMENTS AT MAGNIFICATIONS 170, 240, 350 AND 500

4.3 $u_{n_{cal,random}}$ USING PROCEDURE 3

The last case represents measurements of the same distance on voxel models reconstructed from different scans that were taken at different days, with repeated repositioning of the rotation stage along the magnification axis.

The experimental standard deviation and the standard uncertainty in this case are slightly bigger compared to procedure 2, and equal to 0,017 voxels, see *Figure 48*. This value is applicable for this object when **Procedure 3** is applied.

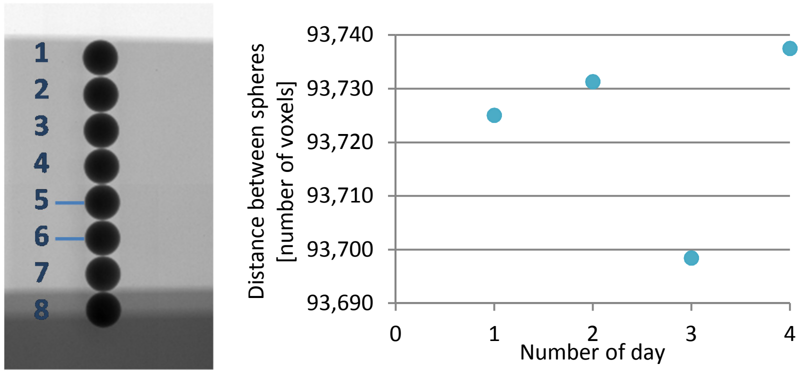

FIGURE 48: REPEATABILITY OF DISTANCE BETWEEN SPHERES OVER DIFFERENT DAYS (**PROCEDURE 3**)

The main measurement settings were as listed inTable 8.

TABLE 8: MEASUREMENT SETTINGS FIGURE 48

Measurement settings
180 kV – 65 µA
ISO50% - Local thresholding
0,1 mm Cu filter
No beam hardening correction
Magnification position 222
1000 projections

In practice, a change of filament, operator, … will have an effect on the chosen parameters, and this can give slightly different results for the measured distances.

4.4 Critical contemplation about ‘edge independent distances’

In Chapter 2, an overview of influence factors on the dimensional measurements with computed tomography is given. Some of these parameters clearly hinder the correct rescaling of the workpiece, e.g. errors on the magnification axis. Other parameters are expected only to influence the edge detection without affecting the rescaling of the CT volume. However, several experiments indicate that the measurement of distance between spheres is influenced by the value chosen by the operator for these factors.

The first parameter which was studied was the **thresholding method**. Where local adaptive thresholding was used for most measurements in this dissertation, also global thresholding (using one single grey value for the edge detection) is widely used. Both methods are compared using the ball plate with ruby spheres (measurement settings listed in *Table 4*, magnification position 150). The same measurement was first analyzed using local thresholding, and based on the same reconstruction, in the software VGStudio MAX, the edge detection method was changed to global thresholding and all the sphere center distances were measured again.

All 52 sphere center distances were considered. The first 2 distances on *Figure 49* are the (longest) diagonals, the next 10 measurements are the 'middle-long' distances as listed in *Table 3*, the next, last 40 measurements are the 'short' distances (see *Table 2*). For each distance, the difference between the measured distance with global and local thresholding is plotted. Although no influence of the thresholding and thus no differences are expected, it is clear that also "edge independent" distances are influenced by the thresholding method. Differences are most pronounced for the longest distances (distance 1 and 2) and middle long distances (distance 3 to 12).

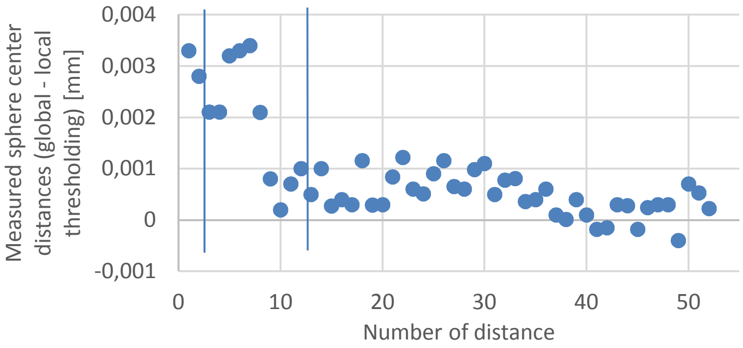

FIGURE 49: SPHERE CENTER DISTANCES ON RUBY PLATE (GLOBAL – LOCAL THRESHOLDING) – DISTANCES AS DEFINED IN FIGURES 38, 40 AND 39 RESPECTIVELY

Secondly, the effect of the **beam hardening correction** was studied. Differences up to 1 µm are observed when the same distance is measured after applying beam hardening correction 2 or beam hardening correction 1 (i.e. no beam hardening correction) in the software CT Pro (*Figure 50*).

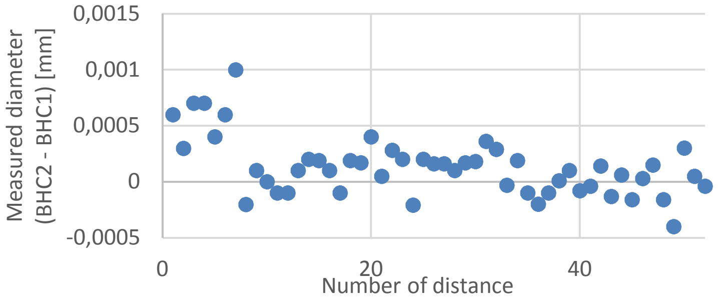

FIGURE 50: SPHERE CENTER DISTANCES ON RUBY PLATE (RECEONSTRUCTED WITH BHC 2 – BHC 1) - DISTANCES AS DEFINED IN FIGURES 38, 40 AND 39 RESPECTIVELY

For most measurements in this dissertation, no beam hardening correction is used (unless stated otherwise).

Besides the beam hardening correction, which should have no influence on the measured value of an "edge independent distance", also the **noise reduction algorithm in the software** will influence the measurement result. Differences between measurements with different noise reduction algorithms up to ±1 µm are measured, see *Figure 51*.

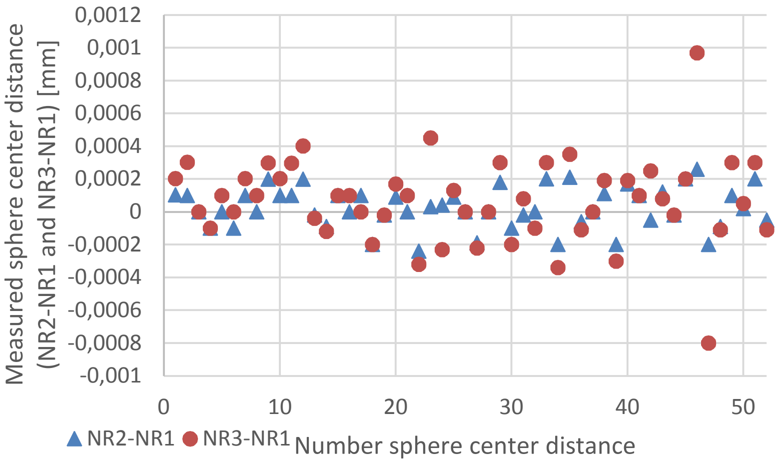

FIGURE 51: SPHERE CENTER DISTANCES ON RUBY PLATE FOR DIFFERENT NOISE REDUCTION ALGORITHMS (NR 2 – NR1 AND NR 3 – NR 1) - DISTANCES AS DEFINED IN FIGURES 38, 40 AND 39 RESPECTIVELY

While "edge independent distances" (e.g. sphere center distances) are expected to be independent of some parameters influencing only the edge, from the analysis above it is clear they are influenced. Differences between measurements with different settings for the edge detection method (global versus local thresholding), the beam hardening correction or noise reduction algorithm in the reconstruction software turns out to be larger than the repeatability in the software VGStudio MAX, which is often 0 for sphere center distances.

CONCLUSION

The uncertainty on the repeatability of the voxel size is dependent on the measurement procedure used, and will be the smallest for procedure 1 and the largest for procedure 2 and 3. For procedure 1, this uncertainty contributor is nearly zero, independent of the material of the verification object, the position on the magnification axis and the thresholding method (global versus local thresholding).

5. $U_{N_{\mathrm{CAL,SYS,NON-UNIFORM}}}$: THE NON-UNIFORMITY OF THE VOXEL-SIZE

5.1 EXAMPLE OF MEASURED NON-UNIFORMITY OF VOXEL-SIZES

Until now, it was assumed that all voxels of the entire CT-model represent the same 'real' distance. The uncertainty sources introduced in the previous sections lead to uniform voxel-size errors: all voxels are subject to the same (yet potentially slightly wrong) resizing. However, the voxel size can also suffer from non-uniformity. An artefact consisting of three rows of steel spheres was measured on a CT device (see *Figure 52*). The distances between adjacent spheres are measured and plotted. Although all spheres have the same size (diameter 4mm ±1µm), a clear trend can be observed. A misalignment between the detector and the rotation axis in the CT machine results in non-uniform voxel sizes over the CT voxel space. These non-uniform, yet systematic errors are more tedious to compensate than the uniform deformations discussed in the next section.

According to the GUM [101], Section F.2.4.5, an equivalent uncertainty can be calculated when corrections for a calibration curve are not applied. "In such situations the result of the measurement is often reported as $Y(t) = y(t) \pm [U_{\mathrm{max}} + b_{\mathrm{max}}]$, where the subscript "max" indicates that the maximum value of U and the maximum value of the known correction b over the range of values of t are used." For this measurement, the maximum value for the correction is approximately 6 µm (see *Figure 52*), this corresponds to an additional uncertainty of 6 µm over a (sphere center) distance of 4 mm (0,15 %).

On *Figure 52*, the same 'trend' was observed for all three rows, which proves that the cause is the non-uniformity of the voxel size, due to a misalignment of the detector.

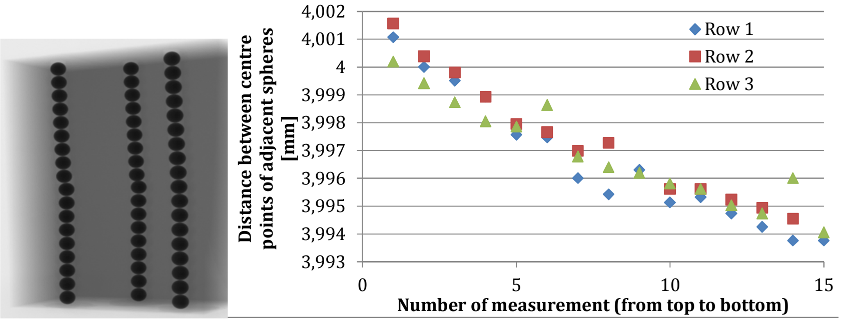

FIGURE 52: NON-UNIFORM SYSTEMATIC ERROR INTRODUCED BY A MISALIGNMENT BETWEEN DETECTOR AND ROTATION AXIS – MEASUREMENT OF 3 ROWS OF STEEL SPHERES

To ensure that the cause of this uncertainty is not inherent to only one measurement, this same object was measured three times, at the same position on the magnification axis. Only one row of steel spheres was measured three times. The results are plotted in *Figure 53*. Since all three measurements show the same 'trend', the cause is not due to a (possible) problem in one of the measurements.

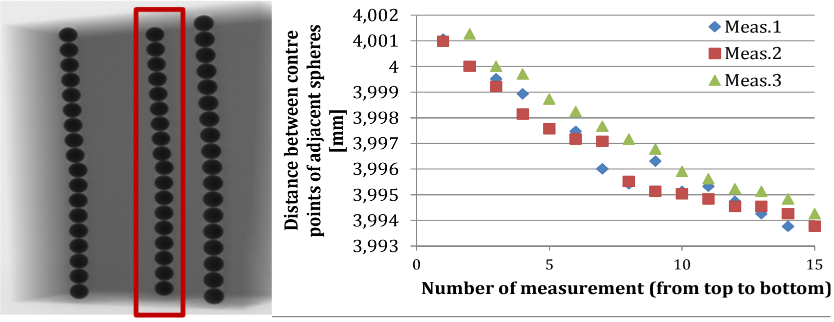

FIGURE 53: NON-UNIFORM SYSTEMATIC ERROR INTRODUCED BY A MISALIGNMENT BETWEEN DETECTOR AND ROTATION AXIS – 3 MEASUREMENTS OF ONE ROW OF STEEL SPHERES

To exclude the possibility that this systematic error is due to a problem at only one position on the magnification axis, this object was measured at different positions (325, 350 and 500). In each case, only one row of spheres was measured, and for each of the measurements, the same 'trend' in the measurement results could be observed (*Figure 54*).

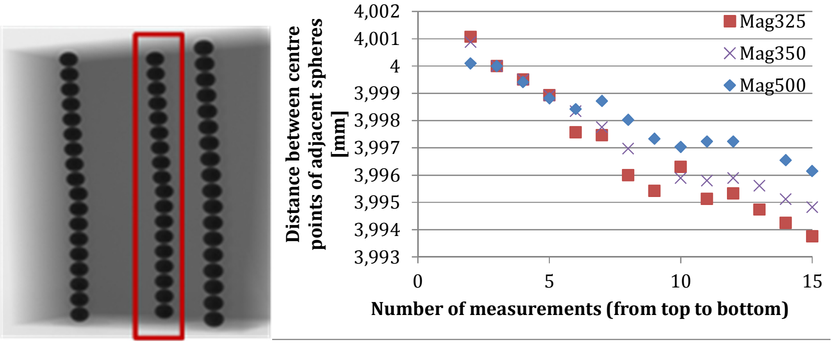

FIGURE 54: NON-UNIFORM SYSTEMATIC ERROR INTRODUCED BY A MISALIGNMENT BETWEEN DETECTOR AND ROTATION AXIS – 3 MEASUREMENTS OF ONE ROW OF STEEL SPHERES AT THREE DIFFERENT MAGNIFICATIONS

Remark: this 'trend' is not present for each and every measurement. For some measurements, this term is much smaller, or even hardly noticeable.

5.2 DESCRIPTION OF PROCEDURE TO DETECT NON-UNIFORM SYSTEMATIC ERRORS

Since the trend observed in the measurements illustrated in *Figure 52* to *Figure 54* are not always present, a procedure is presented to detect systematic non-uniform errors causing an uncertainty on the voxel size.

Description of the procedure to detect non-uniform deformations of the voxel size

First, it should be checked whether the average rescale factor can be used as an estimate for the overall rescale factor.

For each single short distance, the rescale factor (RS) can be calculated as follows:

$$RS_i = \frac{d_{i,CT}}{d_{i,CMM}} \qquad \text{for i = 1…40}$$

Where RS_i is the rescale factor on distance i, $d_{i,CT}$ is the distance i between two adjacent spheres, measured with computed tomography and $d_{i,CMM}$ is the same distance i, measured with the reference measurement instrument (here CMM). These rescale factor can be calculated for 40 distances, resulting in 40 rescaling factors.

When these rescaling factors follow a normal distribution, the mean of these rescale factors can be used as an estimate for the overall rescale factor.

Whether the rescale factors follow the normal distribution is tested using the Lilliefors algorithm (based on Kolmogorov-Smirnov test).

Based on the hypothesis test, and seen on the normal probability plots (in *Figure 55*, normal probability plot for magnification position 318), it can be stated with significance level $\alpha = 0.05$ that the rescale factors come from a normal distribution.

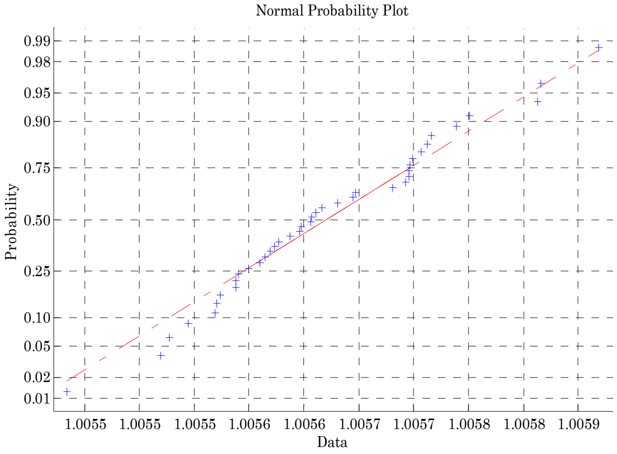

FIGURE 55: NORMAL PROBABILITY PLOT FOR MAGNIFICATION = 318

It is clear from the analysis above the rescale factors are distributed following a normal distribution. This implies the average rescale factor $\overline{\overline{RS}}$, calculated based on those 40 rescale factors can be used as an estimate of the overall rescale factor.

$$\overline{\overline{RS}} = \frac{\sum_{i=1}^{40} RS_i}{40}$$

The deviations on the distances Δd are calculated to be

$$d_{i,CT} \cdot \overline{\overline{RS}} - d_{i,CMM} = \Delta d$$

and plotted for all 40 distances (defined in Table 2) in *Figure 56* at magnification position 318.

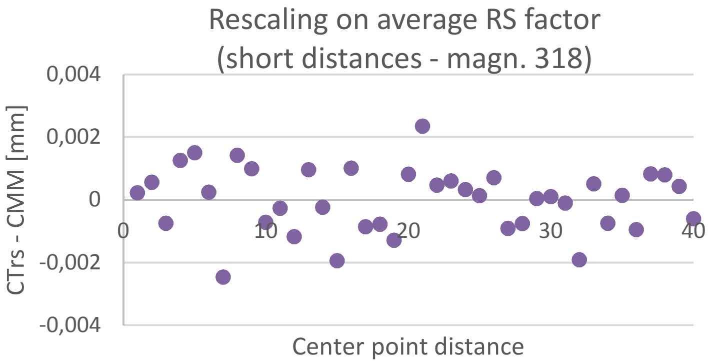

FIGURE 56: RESCALING ON AVERAGE RESCALE (RS) FACTOR, CALCULATED ON ALL (40) SHORT DISTANCES

All deviations between the rescaled CT and CMM (reference) values are smaller than ± 3 µm, and thus smaller than the uncertainty of the CMM (reference) values. From this, it can be concluded that in this case there is no additional uncertainty due to non-uniform errors in the rescaling.

A more convenient way to do rescaling is using a long distance on the object to calculate the rescale factor. Using a long distance to calculate the rescale factor reduces the errors because of a possible rescale error.

Rescaling using either one or the other diagonal (*Figure 57* and *Figure 58*) gives the same result: the deviations are smaller than the uncertainty of the CMM (reference) values.

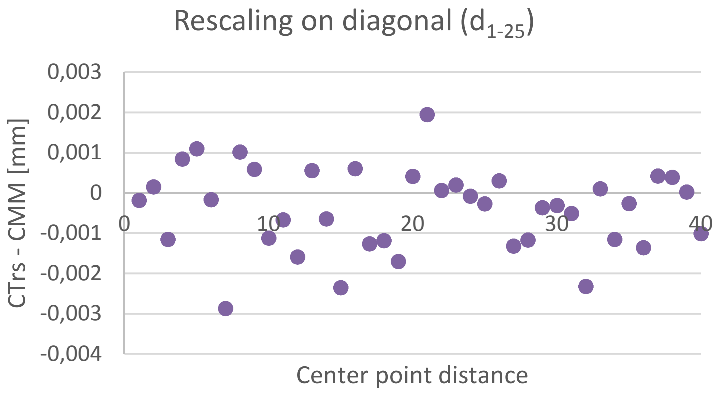

FIGURE 57: DEVIATIONS FROM REFERENCE (CMM) VALUES AFTER RESCALING ON DIAGONAL (D1-25)

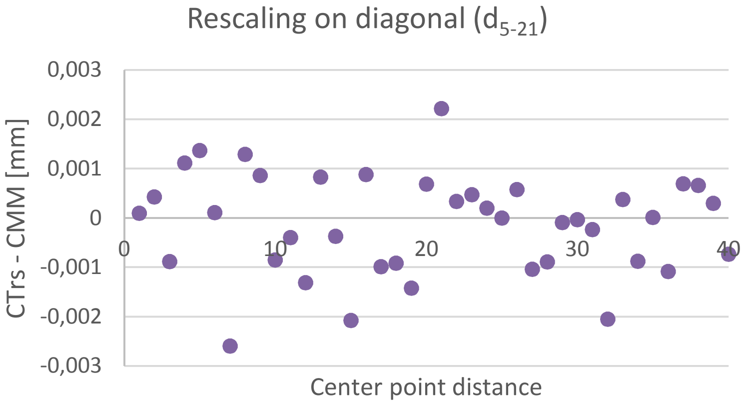

FIGURE 58: DEVIATIONS FROM REFERENCE (CMM) VALUES AFTER RESCALING ON DIAGONAL (D_{5-21})

Different magnification positions

After testing this procedure for one magnification position, 4 other positions along the magnification axis were added. At all 5 positions, the distribution of the rescale factors was tested using the Lilliefors algorithm (based on Kolmogorov-Smirnov test), see *Figure 59*.

In Table 9, the p-values for the Lilliefors test at different magnifications can be found, clearly showing the rescale factors follow (for all magnifications) the normal distribution.

TABLE 9: P-VALUES FOR LILLIEFORS TEST

magnification	**p-value**
219	> 0.05
318	> 0.05
419	0.3385
519	0.1327
600	> 0.05

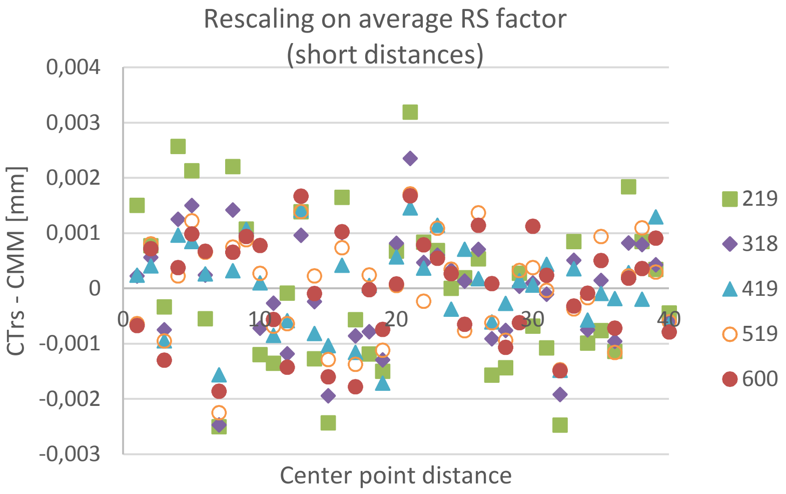

FIGURE 59: DEVIATIONS FROM REFERENCE (CMM) RESCALING ON AVERAGE RESCALING FACTOR, FOR 5 DIFFERENT MAGNIFICATION POSITIONS

Conclusion

Based on the analysis in this paragraph, it can be concluded that there are no non-uniform systematic errors to be taken into account in the calculation of the uncertainty of the rescale factor. The observed non-systematic errors in *Figure 52* to *Figure 54* are only present if there is a misalignment of the detector, and no other non-uniform systematic errors were observed.

6. $U_{N_{CAL,SYS,UNIFORM}}$: SYSTEMATIC, UNIFORM DEFORMATIONS OF THE VOXEL SIZE

A typical uniform deformation of the voxel size is the observed variations over the length of the magnification axis. Using the verification object with the ruby spheres, and analyzing the relative error on the distance between spheres 1 and 2, the error is clearly dependent on the position on the magnification axis, indicating a misalignment of the magnification axis, due to wrong calibration, see *Figure 60*. This systematic error can be measured by a laser interferometer and corrected for. Once corrected, this term is eliminated from the total uncertainty on the voxel size.

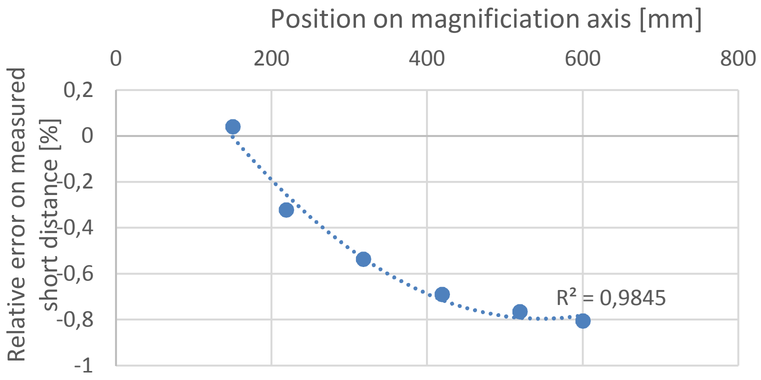

FIGURE 60: RELATIVE ERROR (ERROR OVER MEASURED LENGTH) FOR SPHERE DISTANCE 1-2 AT 6 DIFFERENT POSITIONS ON THE MAGNIFICATION AXIS

When this error is not corrected, the uncertainty in this case is an additional $\frac{0{,}8\%}{\sqrt{3}} = 0{,}46\ \%$, or $4{,}6\ \mu\text{m/mm}$ since the distribution is not known and a rectangular distribution is assumed.

This uncertainty contributor only will be important when procedure 3 is applied. In case procedure 1 or 2 is used, only one position on the magnification axis will be used, and a possible error is compensated by the verification of the voxel size itself.

7. QUANTIFICATION OF UNCERTAINTY CONTRIBUTORS – RESUME

7.1 QUANTIFICATION OF THE UNCERTAINTY CONTRIBUTORS

To determine the measurement uncertainty on the voxel size, the following (sub)terms are present, depending on the followed measurement procedure. Although most uncertainty contributors are present for each procedure, the absolute values for the different (standard) uncertainties are quite different for the different measurement procedures. A summary of the representative examples of this chapter is provided in*Table* 10.

TABLE 10: OVERVIEW OF UNCERTAINTY CONTRIBUTORS FOR DIFFERENT MEASUREMENT PROCEDURES (IN µM/MM)

	$\mathbf{u_{L_{cal}}}$	$\mathbf{u_{n_{cal,random}}}$	$\mathbf{u_{n_{cal,sys}}}$	$\mathbf{u_{n_{cal,sys}}}$
			Non-unif.	Uniform
Procedure 1 **Verification object and measured object in one set-up**	0,25	≈ 0	1 (0,1 %)	/
Procedure 2 **2 consecutive measurements of verification object and measurement object**	0,25	< 0,25 (<0,025%)	1 (0,1 %)	/
Procedure 3 **Periodic verification**	0,25	± 0,18 (± 0,018%)	1 (0,1 %)	4,6 (0,46%)

The uncertainty on the calibrated length is dependent on the verification object used and on the accuracy of the conventional measurement instrument used to measure L_{cal} (e.g. MPE-value of measurement instrument). The more accurate the object can be produced, and the more accurate the reference measurement, the lower will be $\mathbf{u_{L_{cal}}}$.

The uncertainty due to the repeatability of the voxel size correction $\mathbf{u_{n_{cal,random}}}$ is strongly dependent on the measurement procedure. Procedure 1, measuring the verification object and measured object in one set-up implies low values for $\mathbf{u_{n_{cal,random}}}$. However, this cannot always be realized without changing the resolution. Placing the verification object on top of next to the measured object, sometimes ask for changing the magnification.

Due to a misalignment of the detector, important non-uniform systematic errors can be present (§ 5.1). At the other hand, this uncertainty contributor is not always present in that order of magnitude. And moreover, since this is a systematic error, it can – in most cases – be compensated, eliminating it from the total uncertainty.

Combining those standard uncertainties and assuming the different uncertainty contributors are uncorrelated, one can - according to the GUM – combine them as follows

$$u_c = \sqrt{\left(u_{n_{cal,random}}\right)^2 + \left(u_{n_{cal,sys,non-uniform}}\right)^2 + \left(u_{n_{cal,sys,uniform}}\right)^2}\,.$$

Equation 1

Resulting in the combined standard uncertainties listed in

Table 11.

TABLE 11: COMBINED STANDARD UNCERTAINTIES (IN μM/MM)

	u_c
Procedure 1	1 (0,1%)
Procedure 2	1,3 (0,13%)
Procedure 3	4,7 (0,47%)

For procedure 3, the combined standard uncertainty u_c is mainly determined by the uncertainty due the systematic uncertainty on the voxel size if present. Since this systematic error can be compensated (partly) in many cases, it makes sense also to consider the combined standard uncertainty excluding the term $u_{n_{cal,sys}}$. Excluding this term (after compensation), the uncertainty for procedure 3 is similar to the uncertainty for procedure 2.

Based on these values, the uncertainty on the voxel size can be determined using

$$u_{l_v} = \sqrt{\left(\frac{u_{L_{cal}}^2}{L_{cal}^2} + \frac{\left(u_{n_{cal,random}}^2 + u_{n_{cal,sys,unif.}}^2 + u_{n_{cal,sys,non-unif.}}^2\right)}{n_{cal}^2}\right) l_v^2}$$

If the verification length L_{cal} is assumed to be 10 mm in this example and the voxel size is taken to be 30 μm, which is a realistic value for many industrial workpieces, the uncertainty on the voxel size of one voxel u_{l_v} is 0,0076 μm (for procedure 1 and 2) and 0,0086 μm (for procedure 3) per voxel. A distance of 10 mm contains 333 voxels of 30 μm, resulting in an uncertainty on the total length of 2,5 to 2,9 μm.

7.2 TIME ESTIMATION FOR THE DETERMINATION OF THE UNCERTAINTY CONTRIBUTORS

Although the values in Table 10 are based on real measurements, and are a good indication of the order of magnitude of the different uncertainty contributors, the values can change from case to case. Often, it is desirable to calculate (some of) the different uncertainty contributors for a specific workpiece.

Table 12 gives an overview of the estimated time needed for the quantification of the different uncertainty factors during the analysis of the measurement data (excluding the time for the CT measurement on the machine, unless these are extra scans that should be taken).

The information needed to calculate the uncertainty in procedure 1 all can be extracted from only one single measurement, were both the workpiece and the rescaling object are measured at once. No additional CT measurement is needed; all information can be collected from some additional data analysis in the software Volume Graphics.

From *Table 12*, the estimated time for $\mathrm{u}_{\mathrm{n}_{\mathrm{cal,random}}}$ for procedures 2 and 3 is striking. For procedure 2 and 3 at least 5 additional CT scans of the verification object are inevitable to collect all information to calculate the uncertainty on the voxel size. Working with CT scans with 1000 projections, 1 hour per additional scan is counted including scanning, reconstruction and data analysis. 5 scans required for the analysis makes 5 hours. If one wants to limit the random uncertainty to the uncertainty on one day, this asks for a big effort in time. But this time effort is not necessary for each new workpiece measurement. Previous information can be used for a series of measurements, e.g. during one month or until a filament replacement. If this information is collected once a month, roughly one day per month (5 % of the time) should be foreseen for these verification tests. The additional measurement time per scan reduces in that case to a few minutes, which is acceptable.

Since the rescaling object is not scanned together with the workpiece for procedure 2 and 3, an additional hour is included for the additional measurement of the spheres to determine $\mathbf{u}_{\mathbf{n}_{\mathbf{cal,sys,non-uniform}}}$. If also $\mathbf{u}_{\mathbf{n}_{\mathbf{cal,random}}}$ is determined, one of the measurements used to evaluate $\mathbf{u}_{\mathbf{n}_{\mathbf{cal,random}}}$ can be used for the calculation of $\mathbf{u}_{\mathbf{n}_{\mathbf{cal,non-uniform}}}$.

For procedure 3, also $\mathbf{u}_{\mathbf{n}_{\mathbf{cal,sys,uniform}}}$ needs to be determined periodically. 5 measurements on 5 different magnification positions are needed for the evaluation of $\mathbf{u}_{\mathbf{n}_{\mathbf{cal,sys,uniform}}}$.

TABLE 12: TIME ESTIMATION FOR THE OBSERVATIONS OF THE DIFFERENT UNCERTAINTY CONTRIBUTORS

	$\mathbf{u}_{\mathbf{n}_{\mathbf{cal,random}}}$	$\mathbf{u}_{\mathbf{n}_{\mathbf{cal,sys}}}$	$\mathbf{u}_{\mathbf{n}_{\mathbf{cal,sys}}}$
		Non-uniform	Uniform
Procedure1	5 min	1 h	/
Procedure2	5 h (1 day)	1 h	/
Procedure3	5 h (≠ days)	1 h	5 h (1 day)

8. CONCLUSIONS

In this Chapter, the different uncertainty contributors for the uncertainty on the voxel size are enumerated, explained and illustrated with experiments (real measurements). The combined standard uncertainty, as well as the time needed for the quantification is different for the different measurement procedures. The procedure is chosen based on the specifications of the measured object and the time available (on the machine and for data analysis).

Procedure 1 can be followed if the machine settings and object geometry allow to scan the verification object and the workpiece in one set-up. Only one measurement on the machine is necessary.

If the resolution is decreased too much by placing the verification object on top of the workpiece (to prevent both objects influencing each other) or if the machine settings do not allow to scan both in the same set-up, **Procedure 2** should be followed. 2 measurements instead of only one has a big impact on the total measurement time needed, but on the other hand, the uncertainty is not increased significantly due to two consecutive measurements.

If the available time only allows to do one scan, and the verification object cannot be scanned together with the workpiece, **Procedure 3** is suggested. This procedure is faster than the previous one, but an additional uncertainty is introduced due to the uncertainty on the repeatability of the voxel size determination, which only can rely on previous knowledge and will be mainly determined by the accuracy of the magnification axis.

Depending on the measurement procedure and the uncertainty contributors present, the uncertainty on the voxel size ranges between 0,0076 µm and 0,0086 µm on a voxel size of 30 µm.

"Rien n'est moins sûr que l'incertain."
Pierre Dac

CHAPTER 5: UNCERTAINTY ON THE NUMBER OF VOXELS U_N

INTRODUCTION

After the discussion of the uncertainty on the voxel size in the previous chapter, this chapter elaborates on the uncertainty on the number of voxels.

This uncertainty on the number of voxels is further subdivided in uncertainty due to random errors, and (uniform and non-uniform) systematic errors. For each for these uncertainty contributors, several measurements on both industrial and academic workpieces are presented, including the calculation of the standard uncertainty for each example.

How to calculate this part of the total uncertainty for a real object, is illustrated for 2 cases in Section 5. Section 6 shows how to calculate the combined standard uncertainty, starting from the different contributors to the total uncertainty on the number of voxels.

1. UNCERTAINTY ON THE NUMBER OF VOXELS U_N

The number of voxels n enclosed in a certain distance is determined by the edge detection step of the measurement procedure. The number of voxels $n \in \mathbb{R}^+$ not necessarily (even seldom) represents an integer. It is commonly asserted that the uncertainty on CT measurements is limited to ±3 voxels. However, far better accuracies have been reported, depending on the distance type (unidirectional or bidirectional), the measurement procedure, calibration strategy, etc.

The following sections will distinguish between uncertainty contributors stemming from uniform systematic errors ($u_{n_{uniform}}$), non-uniform systematic errors ($u_{n_{non-uniform}}$), and random errors ($u_{n_{random}}$). When taking into account the sensitivity coefficient or voxel size l_v, the uncertainties can be expressed in length units as $u_n \cdot l_v$, which is more comprehensible and used throughout the remainder of this chapter.

Different objects are used to illustrate the different uncertainty contributors. It becomes clear that the ball plates with ruby and steel spheres introduced in Chapter 4 can be used to quantify many of the sub-terms described in this chapter. The numbering of the spheres in the graphs is conform *Figure 61*.

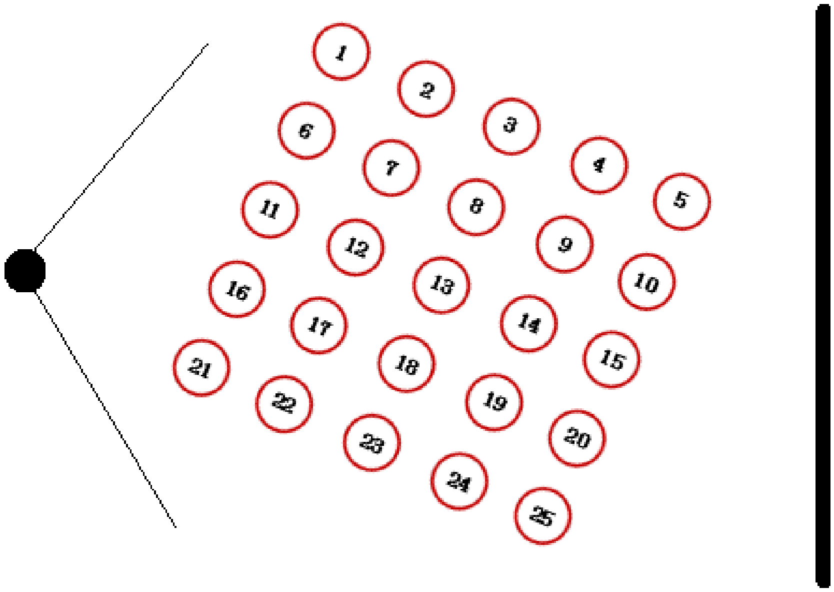

FIGURE 61: NUMBERING AND ORIENTATION OF SPHERES ON BALL PLATE (SOURCE AT THE LEFT, DETECTOR AT THE RIGHT)

2. $u_{n_{random}}$: THE UNCERTAINTY STEMMING FROM RANDOM ERRORS

The random error component of the uncertainty on the number of voxels originates from variability between consecutive reconstructions and calculations of a feature in CT software (e.g. VGStudio MAX). The random error is dependent of the noise level; this is similar to the determination of $\mathrm{u}_{\mathrm{n}_{\mathrm{cal,random}}}$ for calibration Procedure 1, explained in the previous chapter. However, whereas the latter yielded negligible uncertainties due to well-chosen objects (calibrated spheres), $\mathrm{u}_{\mathrm{n}_{\mathrm{random}}} \cdot \mathrm{l}_{\mathrm{v}}$ can amount several micrometers.

The noise level is strongly dependent on the amount of surrounding (disturbing) material, the use of a beam hardening corrections filter and is different for different features (internal features often contain more noise than external features). The procedure how to calculate $\mathrm{u}_{\mathrm{n}_{\mathrm{random}}}$, or the uncertainty due to random errors is the same in all cases, the values can be strongly different due to different scatter leading to bigger random variability.

INFLUENCE OF SURROUNDING ('DISTURBING') MATERIAL

As extensively demonstrated in the previous chapter, the uncertainty due to different observations (measurements) in the software of sphere distances is – in some cases – negligible. As will be illustrated below, this also holds true for the measurement of sphere diameters.

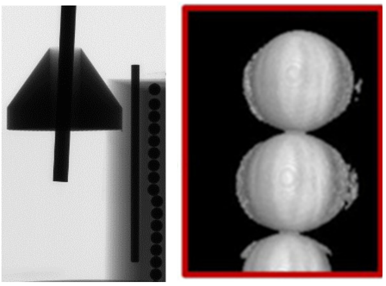

FIGURE 62: INFLUENCING MATERIAL IN THE SURROUNDING OF THE SPHERES, INTRODUCING UNCERTAINTIES DUE TO RANDOM ERRORS ON THE SPHERE DIAMETER (NUMBER OF VOXELS)

TABLE 13: MEASUREMENT SETTINGS OF TEST OBJECT WITH PINS, CONE AND ROW OF STEEL SPHERES (FIGURE 62)

Measurement settings
110 kV
60 µA
1000 projections
No hardware filter
no software BHC
Voxel size = 52,5 µm

To test these influence a stack of spheres has been positioned aside of a truncated cone with a central cylindrical pin (*Figure 62*). The sphere diameters and sphere distances have been measured with the settings of *Table 13*.

Measuring sphere number 8 (counted from the top), which is not influenced by the cone on the top of the figure, gives 10 times exactly the same result in the software VolumeGraphics (4,01356 mm). No uncertainty stemming from random errors is present. However, for sphere number 3 (at the top), measuring the diameter (number of voxels) several times, gives different results, introducing an uncertainty *(Figure 63*). The standard deviation of these distance measurements (observations in the software) is 0,19 µm

$$s(q_k) = \sqrt{\frac{1}{n-1}\sum_{j=1}^{n}\left(q_j - \bar{q}\right)^2} = \sqrt{\frac{1}{8-1}\sum_{j=1}^{5}\left(q_j - 4{,}025\right)^2} = 0{,}19\ \mu\mathrm{m}$$

introducing a standard uncertainty of 0,19 µm on a measured length (diameter) of 4 mm, or a relative standard uncertainty of 0,0475 µm/mm. The position of the object on the magnification axis was 300 for this measurement (*Table 13*). For this machine, the voxel size is determined to be 52 µm/voxel at this position. The uncertainty in this case is 0,00365 voxels (for a measured distance of 4 mm).

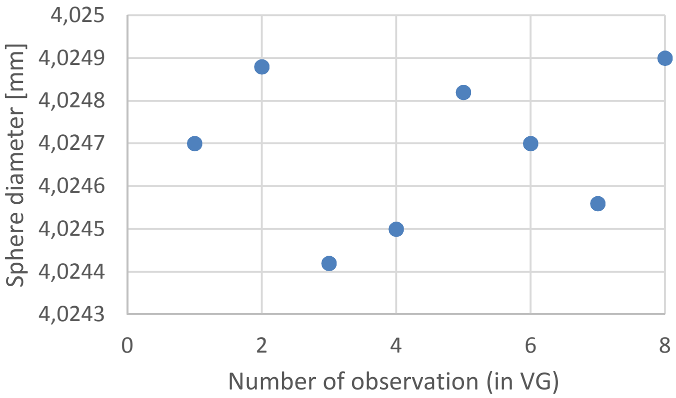

FIGURE 63: 8 CONSECUTIVE MEASUREMENTS (WITHOUT RESCALING) IN VOLUME GRAPHICS OF THE SPHERE DIAMETER OF SPHERE 3 (TOP)

One can notice that also the bottom spheres are influenced by surrounding material. The X-rays penetrating the bottom spheres, also have penetrated the thin cylindrical pin. However, this cylinder has a limited diameter and is 'far' away from the spheres, so the amount of rotation steps where both objects are scanned by the same X-rays is limited, preventing any influence on the measured spheres. This is confirmed by the experiment depicted in *Figure 93,* where at the one hand the distance to the disturbing material (end gage) was changed and at the other hand the thickness of the end gage to study the effect on the uncertainty on the measured diameter of the spheres.

For the ball plates introduced in Chapter 4, the uncertainty of the spheres is negligible, since the repeatability of the diameter measurements was for each of the 25 spheres exactly the same for 10 observations up to 1 nm. However some spheres are influenced by surrounding spheres, the number of projections where the spheres were affecting each other was too small to see the effect of increased variability due to scatter on the diameter measurements (for steel as well as for the ruby spheres).

Also for the measurement of cylinders, the random errors are dependent on the amount of 'disturbing' material.

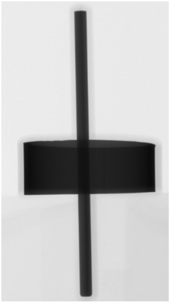

FIGURE 64: STEEL CYLINDER WITH STEEL SURROUNDING MATERIAL

Measurement settings
170 kV
35 µA
1000 projections
no hardware filter
no software BHC
Voxel size = 47,6 µm

TABLE 14: MEASUREMENT SETTINGS (FIGURE 64)

Measuring the diameter of the inner cylinder depicted in *Figure 64* different times (using settings as listed in *Table 14*) as a circle on a slice above the outer hollow cylinder leads to an uncertainty of zero. 10 observations (measurements) in the software VolumeGraphics give the same result. Measuring the diameter at the height of the surrounding cylinder introduces a standard uncertainty due to random errors of 0,21 µm on a measured diameter of 3 mm, see *Figure 65*.

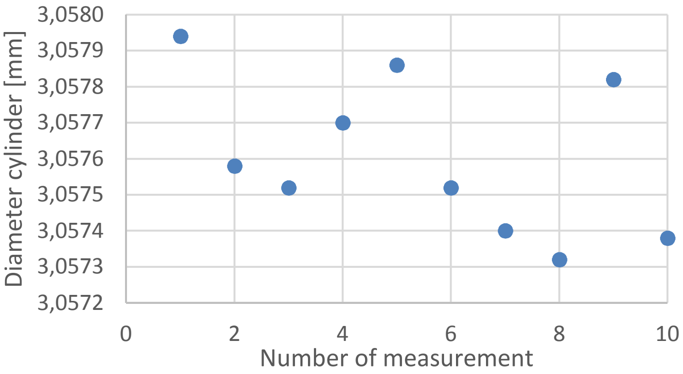

FIGURE 65: VARIABILITY INTRODUCED BY SURROUNDING MATERIAL WHEN MEASURING THE DIAMETER OF THE PIN SHOWN IN FIGURE 64

The effect of the influence of disturbing material is observed not only on steel parts, but also holds true for other materials, e.g. aluminum. To illustrate that, an accurate aluminum inner cylinder, with a hollow surrounding aluminum cylinder around the middle part of the accurate cylinder (*Figure 66*), has been measured with settings as given in *Table 15*.

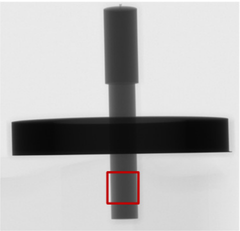

FIGURE 66: ALUMINUM CYLINDER WITH ALUMINUM SURROUNDING MATERIAL

Measurement settings
165 kV
35 µA
magn. 350
1000 projections
no hardware filter
no software BHC

TABLE 15: MEASUREMENT SETTINGS (FIGURE 66)

The standard uncertainty in the zone surrounded by the outer cylinder (in the middle of the inner cylinder) is 4,25 µm for a diameter of about 8 mm. The standard uncertainty for the bottom part of the accurate cylinder is about 0,11 µm on an 8 mm diameter, see *Figure 67*.

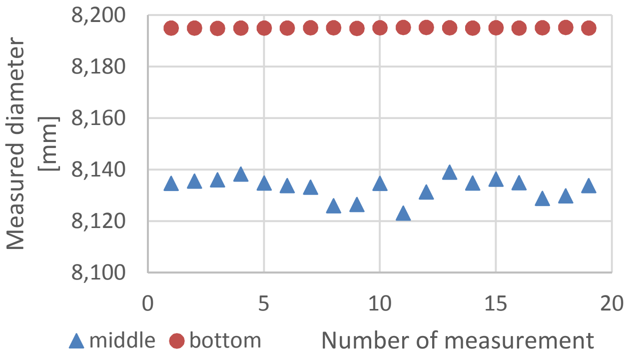

FIGURE 67: UNCERTAINTY DUE TO RANDOM ERRORS ON A CYLINDER, WITH (MIDDLE) AN WITHOUT (BOTTOM) SURROUNDING MATERIAL INFLUENCING THE STANDARD UNCERTAINTY

INFLUENCE OF BEAM HARDENING CORRECTION

Besides surrounding or disturbing material, also the beam hardening correction applied can have an influence on the uncertainty due to random errors.

Using a linear beam hardening correction (preset 2 in the software CT pro) increases the noise level around the cylinder in *Figure 66* at the height of the surrounding material to such a level that the cylinder is no longer measurable.

For the bottom part (without the surrounding cylinder), the diameter was calculated 10 times in the software VolumeGraphics for different beam hardening corrections (same CT measurement/scan and same section of reconstructed voxel model). The 4 beam hardening corrections present in *Figure 68* are the four first presets in the reconstruction software CTpro of Nikon Metrology, used for the reconstruction of the files to a 3D voxel model. Preset one corresponds to no beam hardening correction. Increasing the beam hardening correction (preset 2, 3 and 4) increases here the standard deviation on the measured cylinder diameter (i.e. increased random error) and decreases the average measured diameter (i.e. systematic error on measured diameter), see *Figure 68*. Apparently, other research has proven the beam hardening corrections suggested by the software (presets) are not optimal in many cases [104].

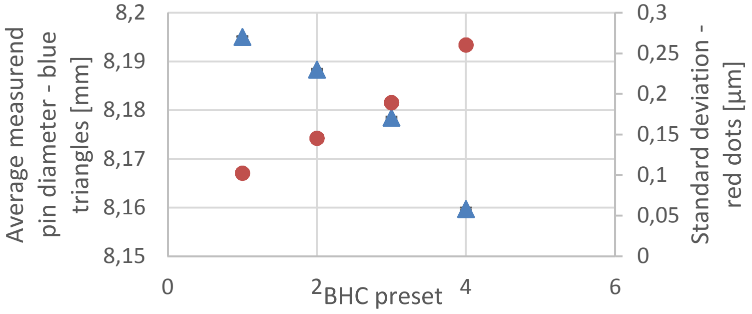

FIGURE 68: DEPENDENCY OF STANDARD DEVIATION (AND AVERAGE MEASURED PIN DIAMETER) FOR DIFFERENT BEAM HARDING CORRECTIONS (BOTTOM PART – WITHOUT SURROUNDING MATERIAL)

INFLUENCE OF FEATURE TYPE (INTERNAL VERSUS EXTERNAL FEATURES)

The random uncertainty on measured dimensions not only is dependent on the measured feature (spheres, cylinders, planes), the beam hardening correction, and the surrounding material, but also some other factors determine the impact of this uncertainty contributor. A clear difference is observed between inner and outer features. To illustrate this, a cylinder head, with internal as well as external features was measured on the 450 kV machine. In contrast to most of the other measurements presented in this text, a higher voltage machine was used, because of the dimensions (and maximal penetration length) of this workpiece. A cylinder head was measured on the 450 kV machine. The measurement parameters are indicated in *Table 16*.

TABLE 16: MEASUREMENT PARAMETERS ALUMINUM CYLINDER HEAD

Measurement settings
405 kV
200 µA
6 mm Cu filter
1000 projections
no software BHC

On this cylinder head, after reconstruction and edge detection, an inner and outer cylinder, indicated on *Figure 69*, are measured in the software Volume Graphics. Each diameter is calculated 20 times using the same scan data.

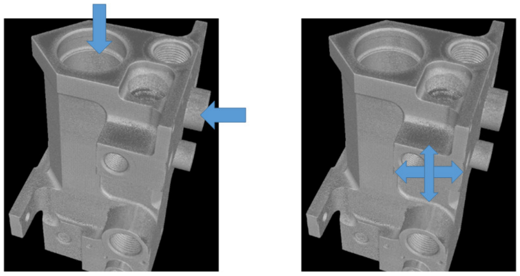

FIGURE 69: CYLINDER HEAD IN ALUMINUM

The calculated diameter of the outer cylinder is shown in *Figure 70*. The range of the 20 observations on the 3D model in the software is 10 µm, the standard deviation and standard uncertainty is 3 µm on a diameter of nearly 10 mm.

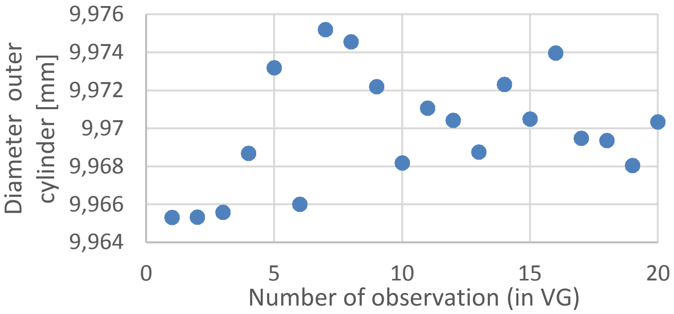

FIGURE 70: 20 CALCULATIONS OF AN OUTER CYLINDER ON A CYLINDER HEAD IN ALUMINUM

For the inner cylinder, the range is 1 mm (notice the different scales between *Figure 70* and *Figure 71*). The standard deviation and standard uncertainty is 266 µm in this case. Notice that the diameter of the inner diameter also is twice as large.

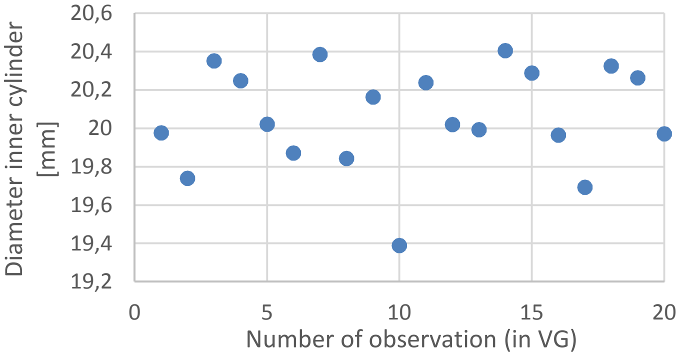

FIGURE 71: DIAMETER OF AN INNER CYLINDER ON A CYLINDER HEAD IN ALUMINUM

Remark: The values of the observed variation (range and standard deviation) above are substantially higher than for the other measurements presented in this chapter. This can be explained by the size of the object and consequently the use of another (more powerful, but less accurate) CT scanner.

INFLUENCE OF FEATURE ORIENTATION

On an industrial workpiece (the cylinder head presented above) a plane-to-plane distance was measured to illustrate the result of the orientation of the feature on the uncertainty due to random errors. A plane-to-plane distance is defined as the distance of one point of one plane, perpendicular to the other plane. 20 observations in the software were made of two plane distances, as indicated on *Figure 69*, right. The measurement parameters are indicated in *Table 16*.

For the horizontal distance, were the planes are oriented perpendicular to the X-ray beam, the standard uncertainty due to random errors is 40 µm, see *Figure 72*.

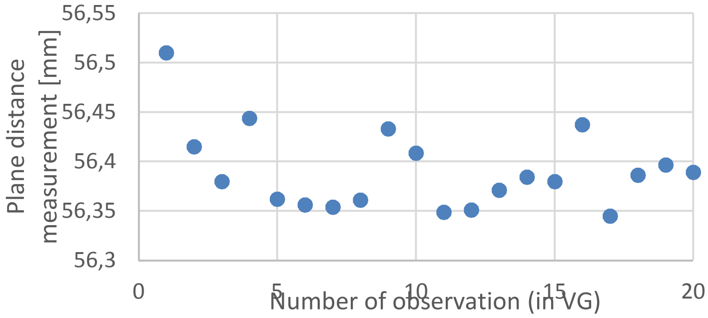

FIGURE 72: PLANE DISTANCE MEASUREMENTS OF PLANES PERPENDICULAR TO THE BEAM

For the planes parallel to the beam, more **noise** is present, resulting in a higher uncertainty, see *Figure 73*.

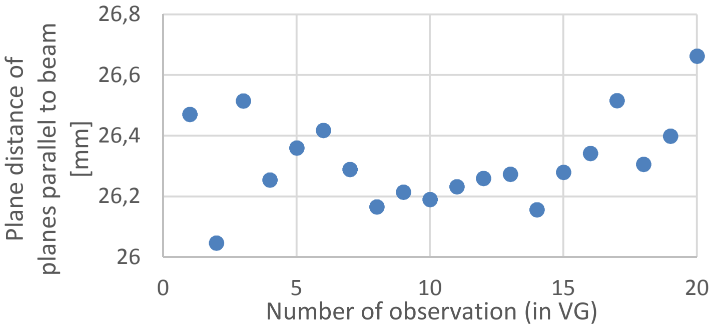

FIGURE 73: PLANE DISTANCE MEASUREMENTS OF PLANES PARALLEL TO THE BEAM

The standard uncertainty increases for this plane distance to 170 µm.

(A Lilliefors test on both datasets confirms they follow a normal distribution.) Based on a chi-square test, the variance is significantly different for both datasets, which implies a determination of the uncertainty on features in one orientation cannot simply be transferred to other features in another direction.

CONCLUSION

The uncertainty stemming from random errors is dependent on different factors. The illustrations in this section show the influence of surrounding material, beam hardening correction, feature, orientation and the location of the measured feature (inner or outer dimensions) on the variability of dimensions calculated with the same CT data (same CT scan or measurement).

The uncertainty due to random errors during calculation is negligible in some cases, but can increase to up to more than 100 µm for other workpieces or features. From this analysis it becomes clear that it is important to quantify this factor for each measurement. The time to estimate this uncertainty contributor is limited to a series of calculations in the analysis software and so takes less than a few minutes. Although this uncertainty cannot be compensated, it can be taken into account in each and every measurement by making 10 (or 20) observations of the feature's dimension in the software (here VGStudio MAX). Each time, different points are selected, which can lead to slightly different results.

One should take into account this uncertainty does not only differs between different CT scans, but can also be significantly different for different features on the same workpiece. It is suggested to calculate this factor for each feature type (sphere, cylinder, plane), and for each feature that differs in orientation (compared to the beam orientation) or position (inner versus outer feature) and whether or not the feature is surrounded by other disturbing material.

Based on 10 observations of the same distance in the software VG, this factor can be determined. How this factor contributes to the total uncertainty on the measured length, is explained in the last paragraph of this chapter.

3. $u_{n_{uniform}}$: THE UNCERTAINTY STEMMING FROM A UNIFORM EDGE OFFSET

An edge-offset is introduced by the different steps of the CT metrology process. CT device settings (X-ray tube voltage and current), hardware filtration type, applied beam hardening correction algorithm, edge detection strategy, etc. all influence the position of the edge of the CT model of the workpiece. Two experienced CT operators will use (slightly) different settings and parameters to measure the same workpiece, since choosing these settings is highly dependent on the users experience, hence introducing additional uncertainty.

The impact of this uniform edge offset on the total uncertainty is illustrated in this paragraph. Based on different measurements, the influence of different parameters on this uncertainty contributor is quantified.

INFLUENCE OF SCANNING SETTINGS (CURRENT AND VOLTAGE)

Measuring the diameters of a row of steel spheres with **different settings** clearly shows the influence of the source settings on the (uniform) edge offset. Measuring the same row of spheres with 5 different settings yields deviations of up to 10 µm for 4 mm spheres (*Figure 74*). For each of the 5 measurements, 1000 projections are taken, and no hardware nor software beam hardening correction was applied.

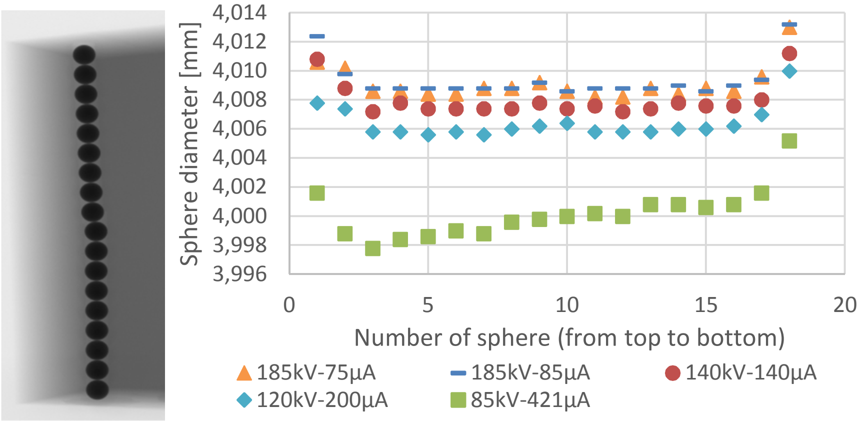

FIGURE 74: SPHERE DIAMETER MEASUREMENTS FOR DIFFERENT VOLTAGE AND CURRENT SETTINGS (FROM TOP TO BOTTOM SPHERE)

In contrast to the determination of the standard uncertainty due to random errors, which estimated based on repeated observations (Type A evaluation), the uncertainty related to a uniform edge offset is determined based on previous measurement data (type B evaluation).

Often, it's possible to estimate only the bounds (upper and lower limits) without specific knowledge of the possible values within this interval a_- to a_+. When a rectangular distribution of possible values is assumed, it is equally probably for a value to lie anywhere in the interval. The expected value is the midpoint of the interval, with an associated variance [101]

$u(x_i)^2 = \frac{(a_+ - a_-)^2}{12}$ and standard uncertainty $u(x_i) = \sqrt{\frac{(a_+ - a_-)^2}{12}}$

For the previous experiments, different settings ranging from 'high' to 'low' settings give an interval of measurement results of 10 µm, resulting in a variance of 8,3 µm, and a standard uncertainty of 2,88 µm on a 4 mm distance.

Not only sphere measurements are affected by the measurement settings, also for plane distances, these findings are confirmed.

Below, an example of a distance measurement between two planes of a ‘cactus step-gage’ (*Figure 75*) is shown. In this case, deviations of up to 70 µm were recorded on a reference distance of 5 mm (voxel size 40 µm).

The standard uncertainty in this case is calculated to be 20 µm although the range of settings used is tighter than in the case of sphere diameters (*Figure 74*).

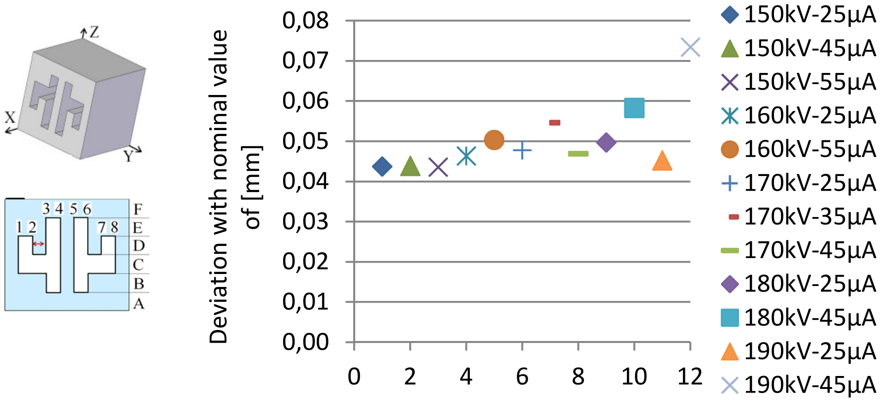

FIGURE 75. DEVIATIONS OF CT VALUES FROM CMM REFRENCE MEASUREMENTS FOR DIFFERENT VOLTAGE AND CURRENT SETTINGS (BASED ON [105])

INFLUENCE OF THRESHOLDING METHOD

In the next experiment, the influence of the **thresholding technique (global versus local thresholding)** was investigated by measuring steel spheres of different sizes. The steel spheres with different diameters were measured in one set-up (*Figure 76*), using no hardware filter (other settings are reported in *Figure 82*).

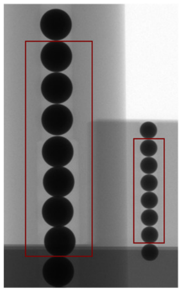

FIGURE 76: STEEL SPHERES WITH DIFFERENT DIAMETERS, MEASURED IN ONE SET-UP (3MM AND 6MM DIAMETER)

Not only a different edge offset for different diameters is observed, also a different edge offset is measured for different measurement settings (voltage and current). For this first series of measurements, a local thresholding method is used, adapting the edge value locally, as for most of the measurements presented in this chapter.

The measurements represent the average value over the different spheres of the same size. The error bars in *Figure 77* are 1σ values over the measurements of the different spheres. The error bars give an indication of the variation over the row of spheres. For some measurements, all spheres in one row gave exactly the same measurement result (for the diameter measurement), resulting in an error bar of size 0.

The conclusions are the same for the 3 mm and the 6 mm spheres. No significant difference is observed for spheres of different sizes.

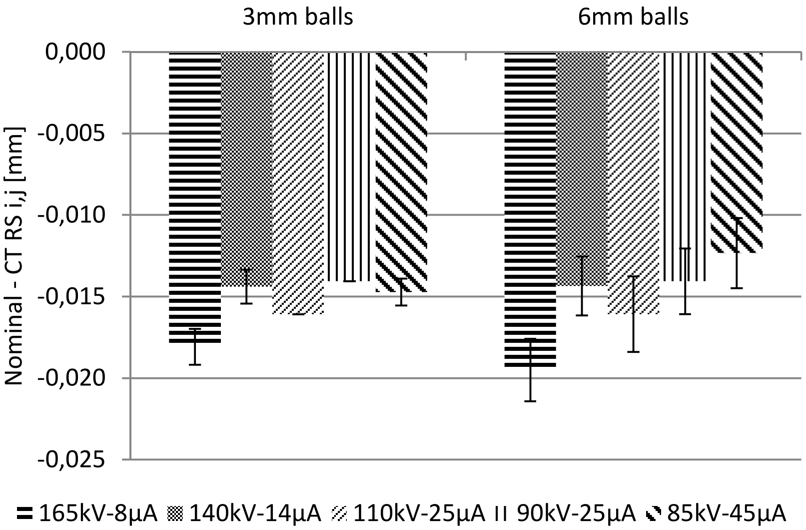

FIGURE 77: SPHERE DIAMETER MEASUREMENTS WITH DIFFERENT SETTINGS, MEASURED WITH LOCAL THRESHOLDING, **WITHOUT** BEAM HARDENING CORRECTION

When using a local adaptive thresholding method, a uniform systematic edge offset of -15 µm ± 5 µm is measured, resulting in a standard uncertainty of 2,9 µm when we expect the exact value to be equally spread over the interval of differences with the real value.

This same set-up was measured also with a global thresholding technique. Notice the difference in the scales of the Y-axis between *Figure 77* and *Figure 78*. The edge offset is around seven times bigger for a global thresholding technique.

The standard uncertainty due to this uniform edge offset is 5,2 µm. Global thresholding results in this case in a bigger uncertainty, compared to local adaptive thresholding.

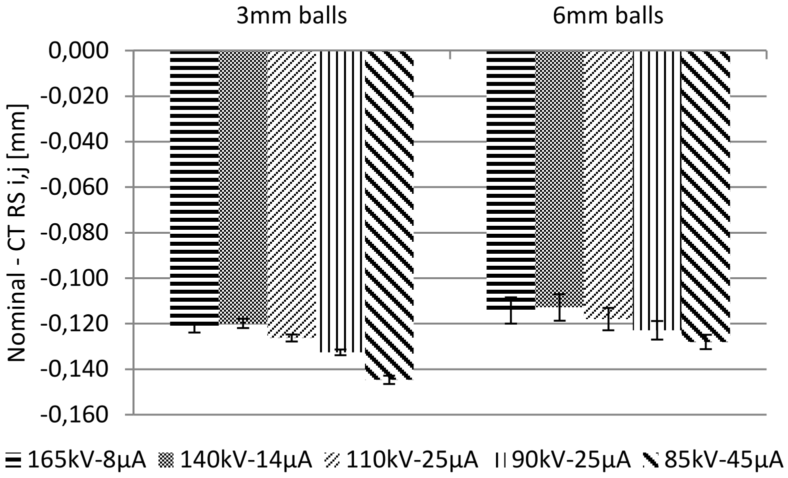

FIGURE 78: SPHERE DIAMETER MEASUREMENTS WITH DIFFERENT SETTINGS, MEASURED WITH GLOBAL THRESHOLDING

INFLUENCE OF BEAM HARDENING CORRECTION

If these same measurements, with local thresholding (*Figure 77*) are measured with **beam hardening correction** (i.e. beam hardening correction preset 2), instead of applying no software beam hardening correction, i.e. preset 1, see *Figure 68*) the edge offset is shifted for about 25 µm.

Without beam hardening correction, the results of the CT measurements were too big, compared to the nominal value. With a beam hardening correction (preset 2), the 3 mm spheres are 10 µm too small, see *Figure 79*.

This edge offset of 25 µm results in a standard uncertainty of 8,8 µm, since we assume a U-shape distribution of possible offsets due to beam hardening correction between 0 and 25 µm.

At the other hand, if one knows on beforehand which beam hardening correction should be applied, this uncertainty reduces to zero. A systematic error which is well known can be compensated for, limiting the total uncertainty.

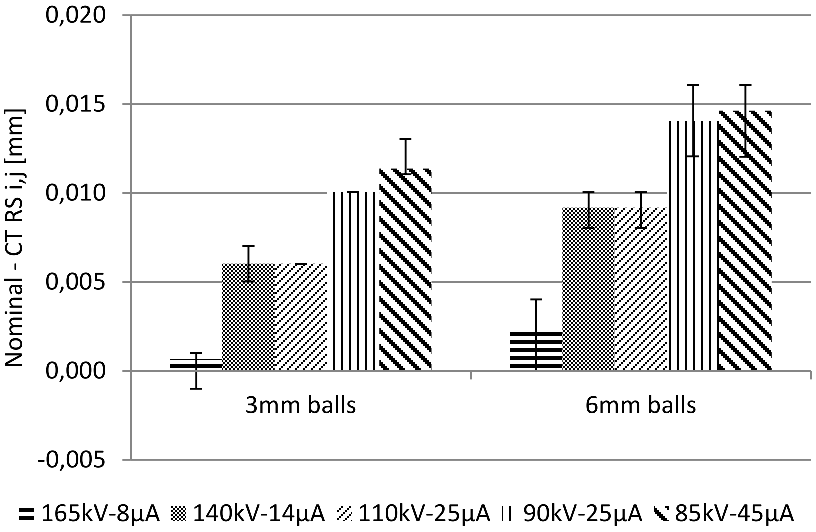

FIGURE 79: SPHERE DIAMETER MEASUREMENTS WITH DIFFERENT SETTINGS, MEASURED WITH LOCAL THRESHOLDING, **WITH** BEAM HARDENING CORRECTION

The influence of **beam hardening correction** applied on the measured data is confirmed by another measurement. An aluminum workpiece (profile) with 4 steel spheres on top (see *Figure 80*) was measured and reconstructed with and without beam hardening correction. One of the spheres was calculated 5 times in the software VolumeGraphics. Here, the measured differences between the measurements with and without beam hardening correction are about 15 µm, resulting in a standard uncertainty of 5,3 µm, when assuming a U-shape distribution within the 15 µm range.

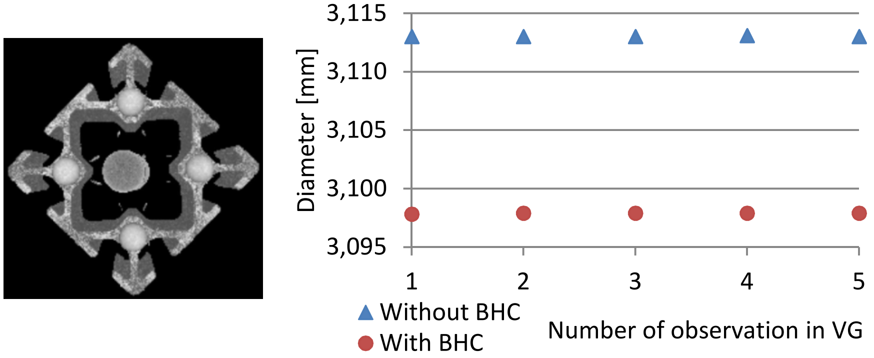

FIGURE 80: SPHERE DIAMETER MEASUREMENTS WITH AND WITHOUT BEAM HARDENING CORRECTION (BHC)

Also for cylinders, the **beam hardening correction** applied on the data during reconstruction introduces and uncertainty on the edge offset value.

An accurate steel cylinder with another stepped aluminum cylinder around part of the accurate cylinder was measured using a 1 mm cupper filter and reconstructed once with and once without beam hardening correction. The result is a shift of the edge offset of up to 8 µm, demonstrating the applied beam hardening correction affects the global edge offset, introducing an uncertainty (*Figure 81*). A standard uncertainty of 2,3 µm (assuming rectangular distribution) should be taken into account in this case if it's not clear on beforehand whether or not a beam hardening correction should be applied.

If a beam hardening correction is applied, also a non-uniform edge offset can be observed, which will be discussed in the next section.

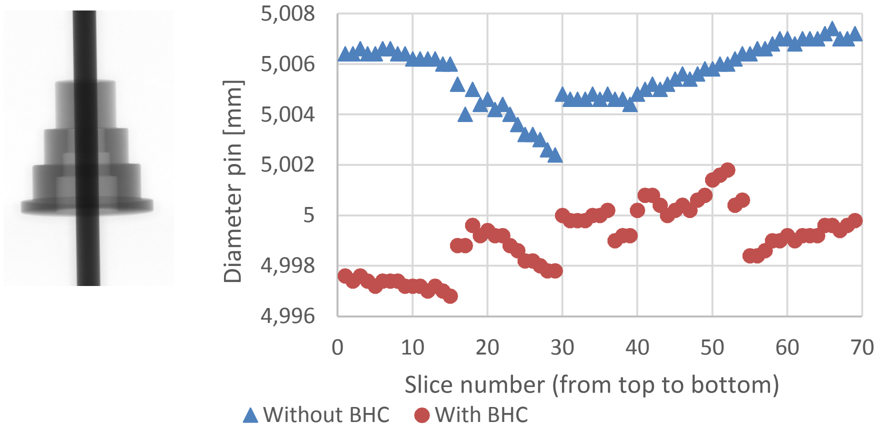

FIGURE 81: STEEL PIN DIAMETER MEASUREMENTS WITH AND WITHOUT BEAM HARDENING CORRECTION (BHC)

Not only the fact whether beam hardening correction is applied or not, also the amount of beam hardening correction influences the uniform edge offset of the measurement. The more correction, the bigger the observed differences. This was extensively discussed in [54] and [106].

INFLUENCE OF HARDWARE FILTER

Using another **hardware filter** also affects the overall edge offset of the measurement. Usually, a hardware filter is chosen by the operator during the set-up of the scan. Which hardware filter gives the best result is often not perfectly known on beforehand. Different filters will give different results, introducing an additional uncertainty.

The measurements of the object depicted in *Figure 76* were repeated using a 1 mm cupper filter (F) (and slightly different settings, see *Figure 82*). Adding this filter introduced an edge offset of more than 10 µm (compared to the measurements without filter), resulting in a standard uncertainty of 2,9 µm, assuming this 10 µm range is the total range due to filtering and a rectangular distribution within this range.

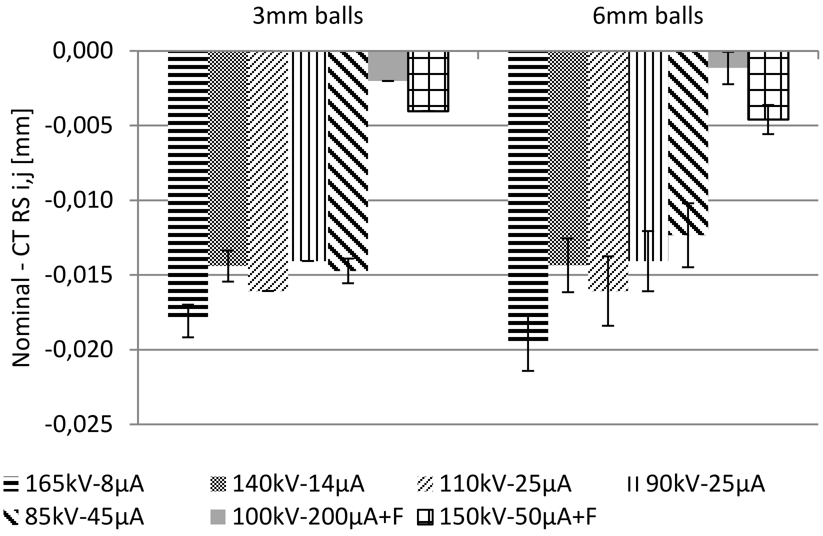

FIGURE 82: SPHERE DIAMETER MEASUREMENTS WITH DIFFERENT SETTINGS, WITH AND WITHOUT HARDWARE FILTER, MEASURED WITH LOCAL THRESHOLDING

The workpiece shown in *Figure 83* was also scanned using two different possible hardware filters. Not only the filter material, but also the measurement settings (current and voltage) differ slightly in both scans, allowing to measure the workpiece with enough contrast in both cases (*Table 17*).

TABLE 17: MEASUREMENT PARAMETERS

1 mm Cu	1 mm Sn
160 kV	200 kV
110 µA	200 µA

The differences between the two measurement set-ups are in this case limited to a few micrometers. The resulting standard uncertainty is limited to less than one micrometer.

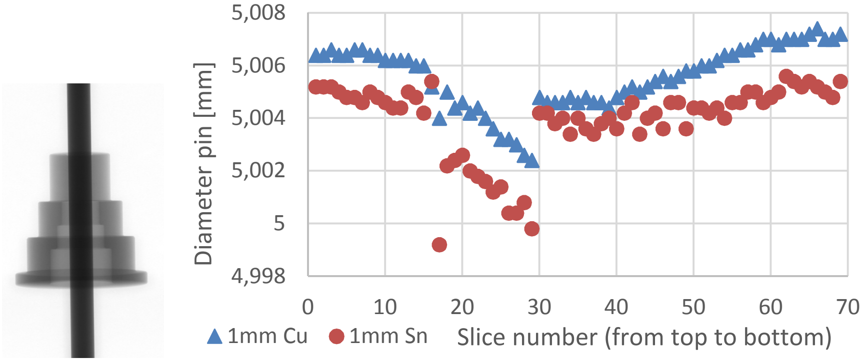

FIGURE 83: STEEL PIN DIAMETER MEASUREMENTS FOR DIFFERENT HARDWARE FILTERS DURING SCANNING

CONCLUSION

A uniform edge offset is determined by the measurement settings (voltage and current), the beam hardening correction (hardware filter and software correction) and thresholding technique (local versus global thresholding).

If it's known on beforehand (e.g. no beam hardening correction is needed), part of the uncertainty introduced by a uniform edge offset is eliminated, or minimized.

While it's feasible to determine the random component of the combined standard uncertainty for each and every measurement (and feature), it would be hard and time-consuming to investigate the upper and lower limits of the interval of possible measurement results due to each of the influencing factors above for every workpiece. To do so, one should for example scan the workpiece with all feasible scanning settings, to investigate the effect on the measurement result. Instead, previous information, gathered by scanning different but similar objects could be used to estimate the effect of a certain parameter.

Remark: since these uniform edge-offsets are systematic errors, once defined, they can be compensated, limiting the total uncertainty due to these systematic errors, or even reducing them to zero. E.g. for some small plastic parts, the beam hardening is limited (or the effect on the measured distance is nearly zero), and the influence of a beam hardening correction is limited (or even inexistent).

For larger batches of the same object, to be measured with CT, it can be useful to perform a series of measurements under different, but realistic conditions (settings, filtering, software BHC, …) to estimate this uncertainty contributor and/or to eliminate from the total uncertainty budget.

4. $u_{n_{non-uniform}}$: NON-UNIFORM EDGE-OFFSETS

NON-UNIFORM VOXEL SIZE

Besides a uniform edge-offset, in some cases also a non-uniform edge offset contributes to the total uncertainty on the measured value.

A first cause of non-uniform edge-offsets on spheres are misalignments in the machine hardware or detector. Once more, an artefact consisting of a row of steel spheres (*Figure 84*), was measured on a CT device (settings as in *Table 18*). The sphere diameters are measured and plotted. Although all spheres have the same size (diameter 4 mm ±1 µm), a clear trend in the measured diameters can be observed. A misalignment between the detector and the rotation axis in the CT machine results in non-uniform voxel sizes over the CT voxel space. These non-uniform, yet systematic errors are more tedious to compensate, and so in most cases indeed contribute to the total uncertainty.

TABLE 18: MEASUREMENT SETTINGS ROWS OF STEEL SPHERES (FIGURE 84)

Measurement settings
180 kV
180 µA
No hardware filter
1000 projections
no software BHC
Voxel size = 46,8 µm

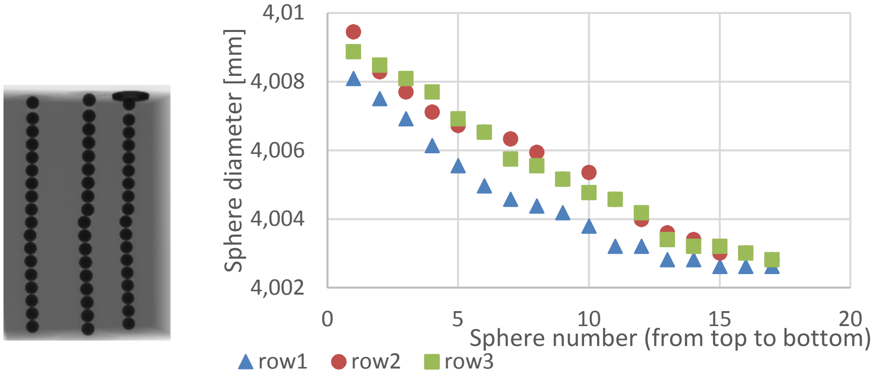

FIGURE 84: EFFECT OF MISALIGNMENT OF THE DETECTOR CAUSING A NON-UNIFORM EDGE-OFFSET

When this edge offset cannot be corrected, and a rectangular (or uniform) distribution is assumed (any possible value can lie wherever in the interval determined by the upper and lower limits), in this case the standard uncertainty due to the non-uniform edge-offset is 2 µm. The range of measurements (2a) is 7 µm.

$$u(x_i) = \frac{a}{\sqrt{3}} = \frac{3{,}5\ \mu m}{\sqrt{3}} = 2\ \mu m$$

assuming a rectangular distribution of the measured diameters.

INFLUENCE OF SURROUNDING ('DISTURBING') MATERIAL

In the frame of the non-uniform edge-offsets, the influence of the **workpiece geometry** also needs to be discussed. Without influence of any other material in the neighborhood of a sphere, the uncertainty on the measured diameter is limited, and no non-uniform edge offset is observed.

This effect has been reported by Dewulf et. al. [87], who investigated the influence of surrounding material on the measurement of a steel cylinder. A systematic error on the number of voxels included in the diameter of the inner steel pin arises due to the surrounding material around one part of the object. To illustrate this influence on the measurement uncertainty, an accurate aluminum cylinder with a reference diameter of 8 mm ± 1 µm was surrounded partly by a thick aluminum ring (d_{out} = 50 mm; d_{in} = 40 mm). The ring introduces beam hardening problems, since the beam has other properties entering the inner cylinder at the top compared to the bottom, hindering correct edge detection. The measurement was done without any hardware or software filter for beam hardening correction. The measurement settings are summarized in *Table 19*. *Figure 85* represents the diameter of the inner cylinder over different slices: an obvious change in diameter (or number of voxels) can be observed were the inner cylinder leaves the outer one, introducing an uncertainty range of about 10 µm in this case, which coincides with a σ of about 3 µm.

TABLE 19: MEASUREMENT SETTINGS OF CYLINDER WITH SURROUNDING MATERIAL (FIGURE 85)

Measurement settings
185 kV
20 µA
No hardware filter
1000 projections
no software BHC
Voxel size = 43,4 µm

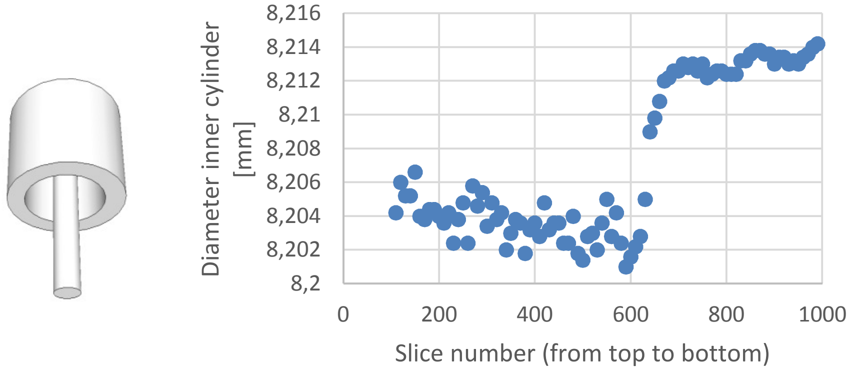

FIGURE 85. DIAMETER OF INNER CYLINDER WITH SURROUNDING MATERIAL (AT THE TOP)

The same conclusion holds true for a steel pin, surrounded by a steel ring (*Figure 86*), proving these observations are material independent. The uncertainty is even bigger for steel than for aluminum, in this case, and is also dependent on the applied software beam hardening correction (BHC1 to BHC4).

The differences in diameter for different beam hardening corrections applied varies from a few to more than 10 µm, but with an appropriate beam hardening correction, (part of) this edge offset can be compensated for, reducing this uncertainty contributor.

TABLE 20: MEASUREMENT SETTINGS STEEL PIN WITH STEEL SURROUNDING (FIGURE 86)

Measurement settings
170 kV
35 µA
No hardware filter
1000 projections
Voxel size = 47,6 µm

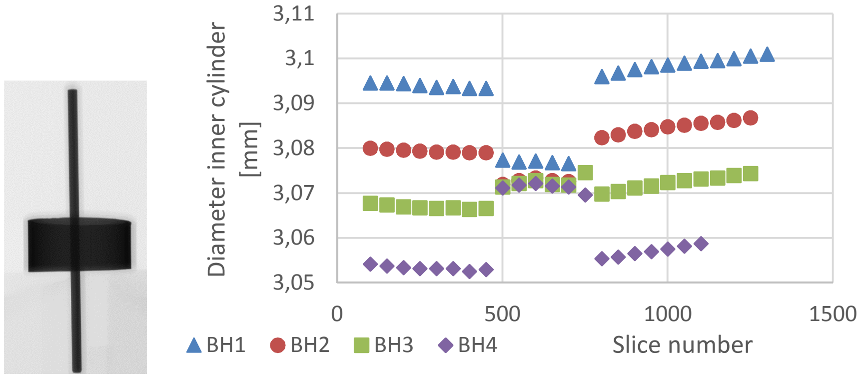

FIGURE 86: STEEL PIN WITH STEEL SURROUNDING HOLLOW CYLINDER FOR DIFFERENT SOFTWARE BEAM HARDENING (BH) CORRECTIONS

To investigate this in more detail, a set-up consisting of an accurate steel pin (measurement object) and a hollow steel cylinder (as surrounding material) was designed. To test the influence of **the amount of surrounding material**, different parts of the surrounding cylinder were cut, leaving a full (1/1), 7/8th, 3/4th, ½ and 1/4th of the cylinder around the steel pin. The surrounding cylinder was located in the middle of the pin (see *Figure 87*).

FIGURE 87: PART OF STEEL HOLLOW CYLINDER (1/4 TH) AROUND ACCURATE STEEL PIN

For the different situations, the top view is shown below (*Figure 88*).

FIGURE 88: CHANGING AMOUNT OF SURROUNDING MATERIAL AROUND AN ACCURATE STEEL PIN (TOP VIEW)

The diameter of the pin was measured from bottom to top, and the result is shown in *Figure 89*. The measurement settings are listed in *Table 21*. The errors induces in the middle part (where the surrounding material is present) are related to the amount of material. The outer hollow cylinder is acting as a hardware beam hardening filter, making the measured diameters smaller, which is consistent with previous results [87]. The beam hardening effect is, for most cases (except for the last case with only 1/4th of the hollow cylinder) overcompensating the effect of the induced noise. Only this situation (1/4th of the hollow cylinder), the noise is making the inner cylinder bigger.

TABLE 21: MEASUREMENT SETTINGS STEEL PIN SURROUNDED BY VARYING SURROUNDING MATERIAL (FIGURE 87 AND FIGURE 88)

Measurement settings
185 kV
300 µA
No hardware filter
1000 projections
Voxel size = 47,4 µm

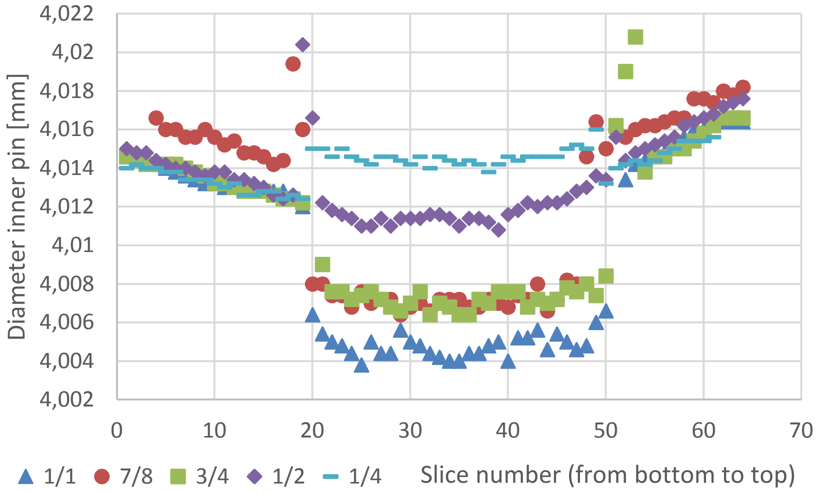

FIGURE 89: DIAMETER OF ACCURATE PIN SURROUNDED BY OTHER MATERIAL – INFLUENCE OF SURROUNDING MATERIAL ON SPHERE DIAMETERS

Where a lot of surrounding material is present (more than ½ of the whole cylinder, the beam hardening effect makes the diameter of the inner pin smaller. The less the surrounding material, the smaller the error, compared to the diameter of the cylinder at the non-influenced zones (top and bottom).

In the worst case, when the inner cylinder is completely surrounded by the outer cylinder (1/1), the difference in diameter between the situations with and without disturbing material is about 10 µm, inducing an uncertainty of 2,9 µm. Depending on different parameters (workpiece material, amount of surrounding material, beam hardening correction applied, ...) estimating the uncertainty due to surrounding material is difficult, hence an additional uncertainty should be taken into account when a feature of interest is influenced by another object or another part of the same object.

In some cases, influences are seen on the workpiece itself. On the workpiece presented in Chapter 4 (ball plate with steel spheres), some spheres are influenced by other spheres on the same workpiece. The measured diameter on the spheres is clearly dependent on the position on the ball plate, see *Figure 90*. But, also the form errors seem to follow the same "pattern"; low form errors for the spheres that do not overlap in any projection with other spheres, and the biggest form error for the spheres in the middle of the plate, hindered by other spheres of the ball plate.

The form error is defined here as the range of the fitpoints used by the software VGStudio MAX to define the sphere. After selecting 10 points manually, the software automatically adds about 1000 points to define one sphere. The range of these 1000 points is used as the form error on the sphere.

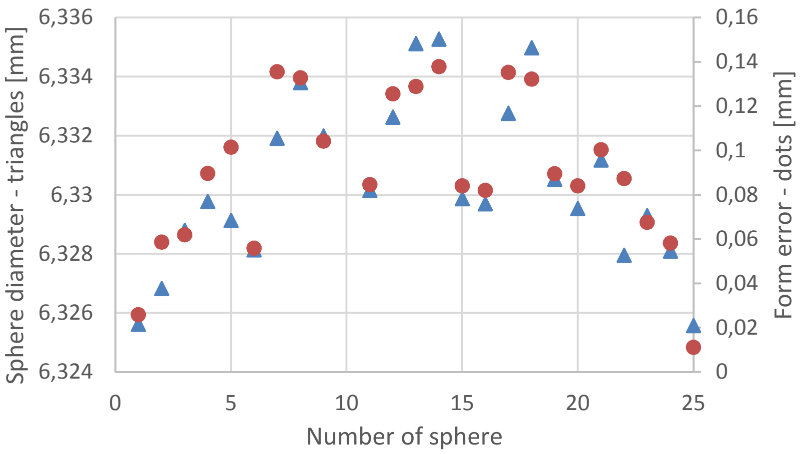

FIGURE 90: MEASUREMENT OF STEEL BALL PLATE – SHPERE DIAMETERS (TRIANGLES – LEFT AXIS) AND FORM ERROR (DOTS – RIGHT AXIS)

Based on this workpiece, where some spheres are clearly influenced by others spheres, a systematic approach to account for this uncertainty contributor is proposed below.

In a first step, the measured diameters and form errors are plotted for all 25 spheres of the steel ball plate in *Figure 91*, visualizing the correlation between both, resulting in an R^2 value of more than 85%.

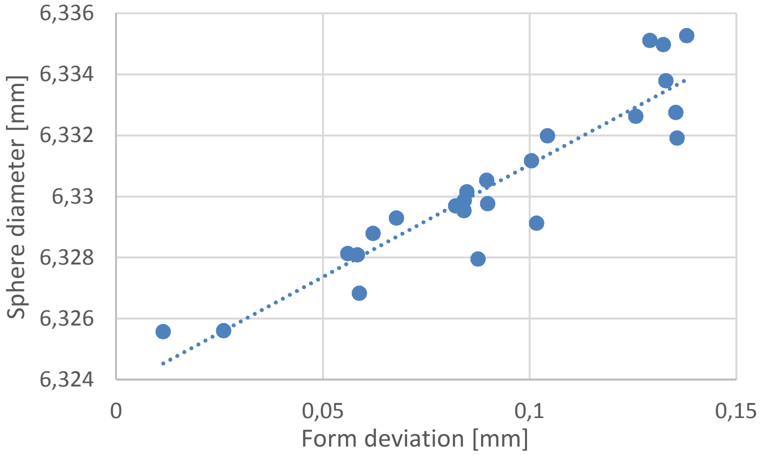

FIGURE 91: CORRELATION BETWEEN FORM DEVIATION AND SPHERE DIAMETER

Instead of calculating the uncertainty for one single sphere, the information of all spheres of the workpiece is taken into account. Using the information the sphere diameter and form error are correlated, the confidence interval for the mean value of y (sphere diameter) for a certain value of x (form error) is defined by

$$(\widehat{m}x_p + \widehat{b}) \pm t_{\frac{\alpha}{2},n-2}\, S_{y,x}\sqrt{1 + \frac{1}{n} + \frac{(x_p - \bar{x})^2}{S_{xx}}}$$

where $\widehat{m}$ is the least square estimator of the slope; $\widehat{b}$ is the least square estimator of the intercept. $S_{y;x}$ is the standard variation of the predicted y-value for each x in the regression.

$$S_{y,x}^2 = \left(\frac{1}{n-2}\right)\sum_{i=1}^{n}(y_i - \hat{y}_i)^2$$

$$SS_{xx} = \sum_{i=1}^{n}(x_i - \bar{x})^2$$

Applying to the data in *Figure 91*, the intervals are calculated an plotted in *Figure 92*.

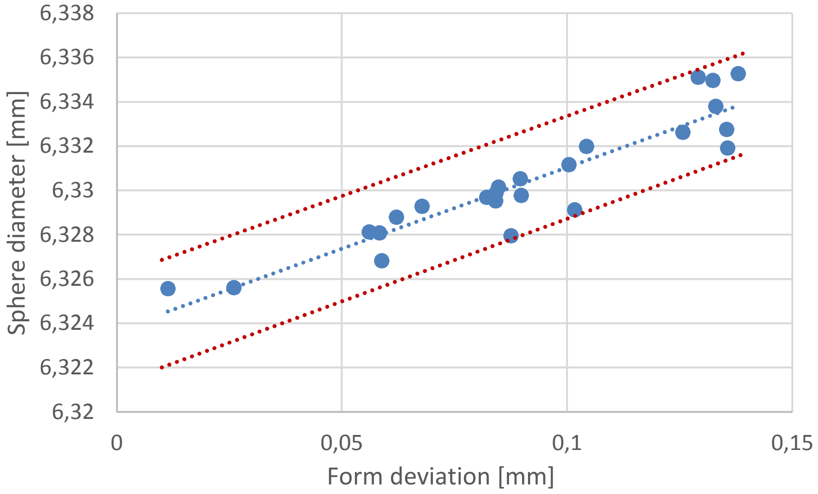

FIGURE 92: PREDICTION INTERVAL AROUND LEAST SQUARE FIT OF CORRELATION BETWEEN FORM DEVIATION AND SPHERE DIAMETER

To calculate the standard uncertainty based on this uncertainty interval, it is assumed that it is equally probable for the possible values x_i to lie anywhere in this interval (uniform or rectangular distribution). The standard uncertainty of this interval ranging from −a to +a is calculated to be $\frac{a}{\sqrt{3}} = 1{,}44\ \mu m$.

5. APPLICATIONS

This procedure of the estimation of the uncertainty on the number of voxels is applied on two other, different workpieces, both containing steel spheres, which are influenced by surrounding material.

CASE 1: Row of spheres with surrounding material (end gage)

A second case illustrating the procedure to determine the uncertainty on sphere diameters (number of voxels) concerns again a row of spheres, in this case influenced by a steel end gage next to the spheres (*Figure 93*). The spheres were numbered from top to bottom, were the bottom spheres overlap in some orientation positions with the end gage. The last sphere is only partly overlapping with the end gage, which will result in a different measured diameter.

Uncertainty on the number of voxels due to random errors, $u_{n_{random}}$

A set-up with a row of accurate steel spheres, in combination with an end gage, influencing the bottom spheres has been measured (*Figure 93*) to investigate the effect of surrounding material on $\mathrm{u}_{\mathrm{n}_{\mathrm{random}}}$. The measurement settings can be found in *Table 22*.

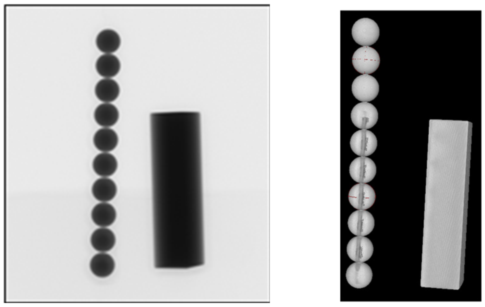

FIGURE 93: 2D X-RAY IMAGE AND 3D RECONSTRUCTED VOXEL MODEL OF A ROW OF STEEL SPHERES AND STEEL END GAGE IN 1 MEASUREMENT SET-UP

TABLE 22: MEASUREMENT SETTINGS OF ROW OF STEEL SPHERES WITH STEEL END GAGE (FIGURE 93)

Measurement settings
175 kV
300 µA
1000 projections
0,5 mm Cu filter
No software BHC
Voxel size = 46,7 µm

Measuring the second sphere, counted from the top, gives – as in the previous example – 10 times exactly the same result for all measurements. No uncertainties due to random errors are introduced in this case. Measuring the 7th sphere leads to the measurement results in *Figure 94*. The standard deviation, and so the standard uncertainty due to the random errors introduced by the end gage is 0,17 µm over a measured length of 5 mm in this case. Increasing the distance between the spheres and the end gage with 10 mm, or reducing the thickness of the end gage from 7 to 5 mm reduces this uncertainty to negligible values. No effect of the disturbing material can be observed if the distance between both is too small and the amount of disturbing material is too less.

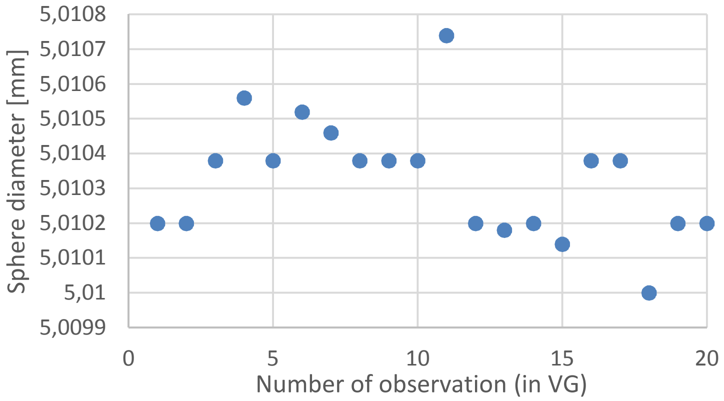

FIGURE 94: 20 CONSECUTIVE MEASUREMENTS (WITHOUT RESCALING) IN VOLUME GRAPHICS OF THE SPHERE DIAMETER OF SPHERE 7 (COUNTED FROM THE TOP) INFLUENCED BY THE MATERIAL OF THE END GAGE

Uncertainty on the number of voxels due to systematic errors, $u_{n_{sys}}$

Plotting the sphere diameters from top to bottom (*Figure 95* – left axis, blue triangles), no uniform, systematic errors seems to be present. However, a clear non-uniform error on the voxel size is clearly visible, knowing the first three spheres are not affected by the surrounding material, the last six sphere overlap in some orientations with the material of the end gage.

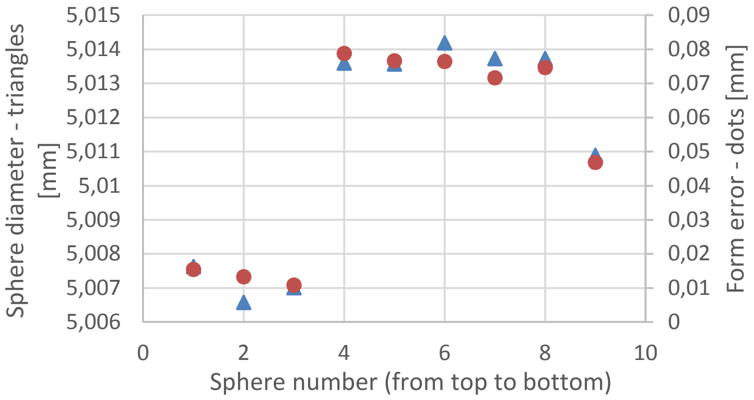

FIGURE 95: MEASURED SPHERE DIAMETERS (LEFT AXIS – TRIANGLES) AND FORM ERRORS (RIGHT AXIS – DOTS) (FROM TOP TO BOTTOM)

For each of the spheres, the diameter was measured, as well as the form error (*Figure 95* – right axis, red dots). Plotting the diameter and form error on the same graph, a good correlation between both is expected. This correlation is confirmed in *Figure 96*, resulting in a R^2 value of 0,99.

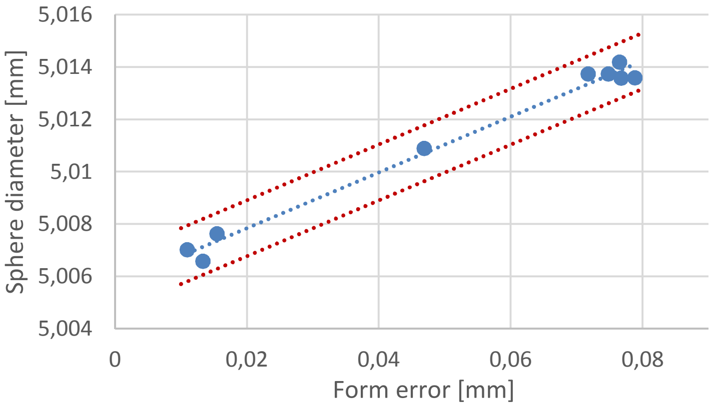

FIGURE 96: CORRELEATION BETWEEN SPHERE DIAMETER AND FORM ERROR FOR A ROW OF SPHERES INFLUENCED BY SURROUNDING MATERIAL (END GAGE)

Although the range of the variation on the diameters is 8 µm, the 95% variability interval on the relation between diameter and form error is only 2 µm wide (assuming no uncertainty on the form error), which allows to give a realistic uncertainty on the sphere diameter, without over-estimating this uncertainty contributor.

How these different terms are combined to the total expanded uncertainty, is shown in Section 6.

CASE 2: Row of spheres with adjacent material (cone)

To investigate the effect of the noise on the size error, a workpiece with spheres, and some 'adjacent material' was used (shown in *Figure 97*, left).

The error on the measured sphere diameter induced by the adjacent material, was measured in the software VGStudio MAX. The top spheres are at the same height as the thickest part of the aluminum cone, the spheres at the bottom are located below the cone.

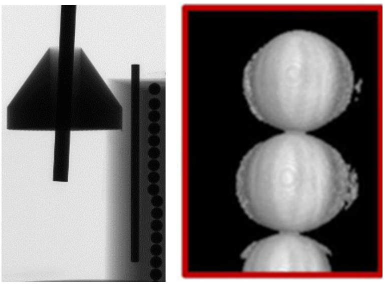

FIGURE 97: TEST OBJECT CONSISTING OF TWO PINS, AN ALUMINUM CONE AND A ROW OF STEEL SPHERES

The measurement settings are summarized in *Table 23*.

TABLE 23: MEASUREMENT SETTINGS OF TEST OBJECT WITH PINS, CONE AND ROW OF STEEL SPHERES

Measurement settings
110 kV
60 µA
No hardware filter
1000 projections
no software BHC
Voxel size = 52,5 µm

Due to the adjacent material (the cone in this case), some noise and induced form error can be seen on the 3D voxel model of the spheres (*Figure 97*, right). Plotting the measured sphere diameter for all the spheres (from bottom to top, in *Figure 98* it becomes clear the measured diameter increases with increasing form error. As in the case of the steel ball plate, a correlation between both the sphere diameter and the form error is expected.

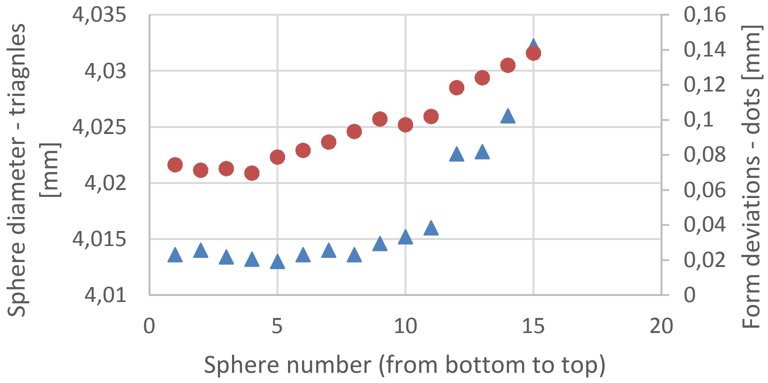

FIGURE 98: MEASURED SPHERE DIAMETERS (LEFT AXIS – TRIANGLES) AND FORM ERRORS (RIGHT AXIS – DOTS) (FROM BOTTOM TO TOP)

Plotting this correlation leads to *Figure 99*. The coefficient of determination (R^2) is 0,84 for this measurement. (The top sphere was excluded, since this sphere encountered effects of the edge of the plastic block in which the spheres were enclosed).

On this graph, not only the trend line for this correlation is plotted, but also the prediction interval is added conform the procedure described above. However the range of diameters for this measurements is 19,2 µm, the estimated uncertainty interval on the relation between diameter and form error is limited to 12 µm, resulting in a standard uncertainty of $\frac{6\ \mu m}{\sqrt{3}} = 3{,}4\ \mu m$ (assuming no uncertainty on the form error).

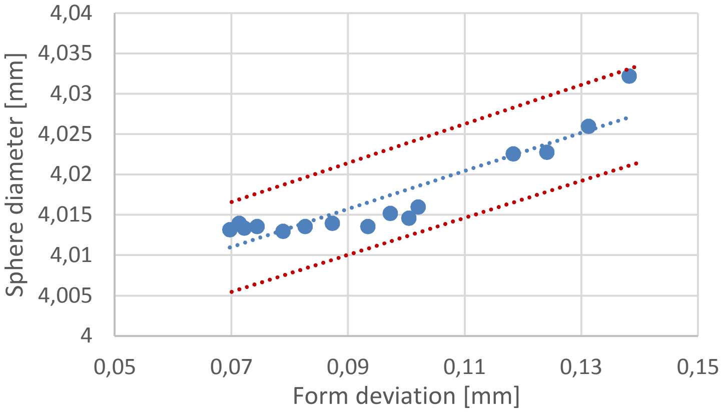

FIGURE 99: CORRELEATION BETWEEN SPHERE DIAMETER AND FORM ERROR FOR A ROW OF SPHERES INFLUENCED BY SURROUNDING MATERIAL (CONE)

This workpiece (*Figure 97*) also contains a steel pin (accurate cylinder). Also for this cylinder, the diameter changed from top to bottom, due to the cone which is overlapping in some orientations, inducing form errors on the cylinder. The same analysis is performed for the cylinder, and the diameters, form errors, trendline ($R^2 > 90\%$) and uncertainty interval are plotted in *Figure 100*). From the figure, it is clear the proposed procedure also can work for other features, not only for spheres.

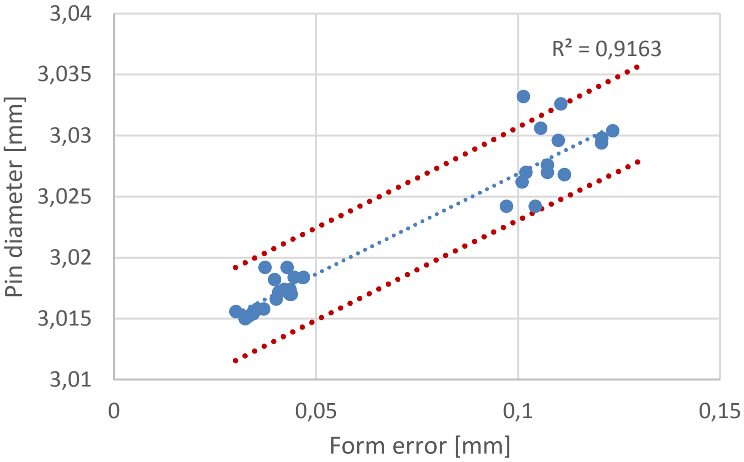

FIGURE 100: CORRELEATION BETWEEN SPHERE DIAMETER AND FORM ERROR FOR AN ACCURATE STEEL PIN (CYLINDER) INFLUENCED BY SURROUNDING MATERIAL (CONE)

CONCLUSION

Non-uniform edge-offsets originates from a non-uniform voxel size over the voxel volume. Deformations and misalignments of the detector or rotation stage (including the mechanical system) can cause uncertainties. If a deformation of misalignment of the mechanical system is expected, it's important to consider this extra uncertainty. By measuring a row of accurate steel spheres, some of these mechanical imperfections can be quantified as shown in this section. Even when known precisely, compensating this non-uniform deformations is rather complex, and out of the scope of this text. However, if these mechanical errors are present, they should be taken into account. Often, a worst case assumption based on the measurement of a row of accurate steel spheres can give a realistic estimation of the uncertainty introduced by these errors. In other cases, for well calibrated, well aligned systems, this term reduces to zero.

Another important contributor to a non-uniform edge-offset is surrounding or disturbing material overlapping partly with the feature of interest in some or all orientations during the CT data acquisition. The procedure presented in this paragraph shows how to take this uncertainty into account, without over-estimating this contribution to the total uncertainty budget.

6. COMBINED STANDARD UNCERTAINTY

The combined standard uncertainty is equal to the positive square root of the combined standard uncertainties obtained from the different uncertainty contributors [101], where all input quantities are assumed to be independent.

$$u_c = \sqrt{\left(u_{n,random}\right)^2 + \left(u_{n,uniform}\right)^2 + \left(u_{n,non-uniform}\right)^2}$$

Each of these three main uncertainty contributors is further subdivided in different subterms, e.g. the uncertainty on the number of voxels due to a systematic, uniform edge offset (if present) can be calculated as

$$u_{n,uniform} = \sqrt{\left(u_{n,unif.,sett.}\right)^2 + \left(u_{n,unif.,thresh.}\right)^2 + \left(u_{n,unif.,BH}\right)^2 + \left(u_{n,unif.,filt.}\right)^2}$$

Illustration for CASE 1

For the first case in the previous section, the different uncertainty contributors influencing the number of voxels were quantified and summarized below in *Table 24* below.

TABLE 24: UNCERTAINTY BUDGET FOR UNCERTAINTY ON NUMBER OF VOXELS FOR CASE 2

Source of uncertainty on the number of voxels	Value ±	Prob. Distr.	Divisor	Standard uncertainty
Uncertainty due to random errors	0,17 µm	Normal	1	0,17 µm
Uncertainty due to uniform systematic errors	≈ 0			≈ 0
Uncertainty due to non-uniform systematic errors	2 µm	Rect.	$\sqrt{3}$	1,15 µm
Combined standard uncertainty		Assumed normal		1,16 µm
Expanded uncertainty		Assumed normal (k=2)		**2,3 µm**

The expanded uncertainty on the spheres of this workpiece, due to random and systematic errors is 2,3 µm over a distance of 5 mm. Knowing the voxel size is 46,7 µm, the uncertainty also can be expressed as 0,049 voxels on the total length, including 107 voxels (5 mm/46,7 µm per voxel).

$$\frac{2{,}3\ \mu\mathrm{m}}{46{,}7\ {}^{\mu\mathrm{m}}/_{\mathrm{voxel}}} = 0{,}049\ \mathrm{voxels}$$

7. CONCLUSIONS

In this chapter, the uncertainty on the number of voxels due to random and systematic errors is quantified for different objects.

The uncertainty stemming from **random errors** due to surrounding material, beam hardening correction, feature, orientation and the location of the measured feature (inner or outer dimensions) are studied. This uncertainty contributor can be estimated by taking several (e.g. 20 or preferably 30 or more when using an extension factor of ±2 or ± 3 to calculate the extended uncertainty) observations in the software VGStudio MAX. Since this only takes a few minutes time, this uncertainty contributor can easily be estimated for each and every measurement.

A **uniform edge offset** can be caused by the measurement settings, the beam hardening correction and thresholding technique. Parts of this uncertainty can be eliminated, based on previous knowledge (e.g. known beam hardening correction to be applied), which makes that this term in some cases can reduce to zero. When this term cannot be compensated for, a rectangular distribution is assumed between the range of measured values allowing to estimate this term for the workpiece which is studied.

Non-uniform edge-offsets can originate from a non-uniform voxel size over the voxel volume due to imperfections in the mechanical system, which is negligible for a well calibrated machine. Another important contributor to a non-uniform edge-offset is surrounding or disturbing material overlapping partly with the feature of interest while scanning, important for most industrial workpieces. This overlap during some (or all) projections causes form errors, that can be used to estimate the induced uncertainty, as is shown for the steel ball plate, and for two applications at the end of this chapter.

"The future is uncertain, but the end is always near."
Jim Morrison

CHAPTER 6: GENERAL CONCLUSIONS

1. CONTEXT OF THE RESEARCH

The most frequently asked questions related to my work during the last years were "How accurate is your CT system?" and "What's the accuracy I can expect when measuring this part with CT?". Two questions that can be translated to "What's the measurement uncertainty of CT for dimensional metrology?"

As long as this question cannot be answered, CT will not be able to 'grow up' from a nice inspection tool, to a valuable, reliable technique for dimensional metrology.

This PhD research aimed to answer the questions above, at least to some extent. Procedures to identify and quantify different contributors to the total uncertainty are presented and illustrated with many CT measurements of different objects.

2. MAIN CONTRIBUTIONS

2.1 VERIFICATION OBJECT FOR VOXEL SIZE AND EDGE CORRECTION

Although many objects have been proposed to be used as verifications objects in CT metrology, up to now, none of the objects presented aimed to be able to correct for both the voxel size and the error on the edge between the workpiece and the background in the 3D voxel model.

In this work, a cactus-like object ("cactus end gage") has been presented which allows to correct for both errors influencing the accuracy of CT measurements. Containing both several unidirectional (or edge-independent) distances and bidirectional (or edge dependent) distances, scanning this object together with or directly after the workpiece of interest allows to correct the voxel size at the one hand and the edge detection error at the other hand.

This cactus end gage could be made out of different materials and in different sizes, to account for the influence of these parameters.

Besides, this object can be used to estimate the effect of other parameters on the total accuracy such as the influence of scanning parameters (current and voltage) and workpiece orientation.

2.2 DETERMINATION OF THE UNCERTAINTY ON THE VOXEL SIZE

The uncertainty on the voxel size strongly depends on the measurement procedure. Three main procedures are identified and elaborated on before starting to describe the procedure to determine the measurement uncertainty on the voxel size.

Both random and systematic errors are contributing to the total uncertainty on the size of the voxels. Random errors are always present, and cannot be compensated for, hence should be taken into account for each and every measurement. However, in some specific cases, the random errors seem to be negligible compared to other terms in the total uncertainty budget.

How to detect and quantify systematic errors is worked out and illustrated based on a ball plate with 25 steel spheres. In some cases, e.g. when the CT machine is not well calibrated, this factor cannot be ignored and should be included in the total uncertainty on the measured length.

2.3 DETERMINATION OF THE UNCERTAINTY ON THE NUMBER OF VOXELS

Also the uncertainty on the number of voxels has many causes; random as well as uniform and non-uniform systematic errors influence to the total uncertainty on the measured length. Random errors are impossible to compensate, but the standard uncertainty due to these random errors can be estimated using a Type A evaluation (according to the GUM). Even for complex parts, this only takes a few minutes for certain measurement procedures.

One important uniform systematic contributor to the uncertainty on the number of voxels (or the uncertainty on the edge between the background and the material) are misalignments in the mechanical system of the CT equipment. A misalignment of the detector (detector not parallel to the axis of rotation), misalignment of the rotation table, … can cause important contributions to the total uncertainty budget. This factor can be eliminated or reduced to negligible values for machines that are perfectly aligned or in case the errors are studied, measured an can be compensated for.

Other uniform systematic errors arise from using different parameters (settings, filtering, beam hardening correction strategies, …). These effects are difficult to predict, and are taken into account after Type B evaluation of the magnitude of these errors.

Finally, non-uniform systematic errors appear when other material is overlapping in some (or all) orientations during the data acquisition process and hence influencing the dimensional measurements of the workpiece of interest. In this work however, the measured diameter of spheres or steel pins is correlated with the form error. A procedure to estimate the uncertainty due to surrounding material is worked out and illustrated based on two cases.

This thesis concludes with the formulas to combine all the different terms of the total uncertainty on the measured length (or diameter).

3. SUGGESTIONS FOR FURTHER RESEARCH

A test object with parallel grooves was presented to correct for errors on the voxel size and on the number of voxels. This workpiece was made in aluminum, and several centimeters in width, height and length. Since it is well known that edge offset errors strongly depend on the workpiece material on the one hand, and the size of the part (penetrated length) on the other hand, a series of test objects, with different size and of different materials could be useful to estimate the error on the measured length (edge offset) more accurately. Besides, also the feature (inner versus outer features, planes versus spheres, …) is important and will all give different results. A good design of an object with different features, that can be scaled to different sizes and made out of different material would be a useful addition to this work.

It was suggested to estimate the random errors for each and every measurement. In some procedures, this only takes a limited amount of time. However, it could be interesting to estimate the random errors e.g. once per month and to use these values instead of evaluating the contribution of the random errors to the total uncertainty for each and every CT measurement. An in depth study on the measurements needed including the design of the objects to use to gather information which is reliable enough to be used for this term of the total uncertainty would be an interesting contribution, in addition to the procedures described above.

Knowing that imperfections in the mechanical system of the CT machine can contribute to an important extend to the total uncertainty on the dimensional measurements, a better understanding of the effects of different misalignments and mechanical errors can help to reduce the total uncertainty and increase the acceptance of CT as a competitive measuring instrument.

This work investigated how to estimate the uncertainty on the edge detection due to surrounding material around the workpiece of interest. The measured diameter of spheres is correlated to the measured form error. Using this information, an uncertainty interval can be defined. This procedure has been investigated for a ball plate, and is illustrated using several other workpieces containing sphere. For one object, also for a pin, the same procedures seems to give good results. However, it turns out that for some other pin measurements, there still is a correlation between measured diameter and form error, but the relation is inversed; bigger form errors lead in some cases to smaller diameters. A further investigation of this technique for pin and other features (plane distances) could help in further develop a better understanding of the measurement uncertainty of dimensional CT.

4. GENERAL CONCLUSION

Being started at the very beginning of the life of CT as a tool for dimensional metrology, this work has presented a framework to quantify the measurement uncertainty for dimensional measurements with Computed Tomography.

However, for real world, complex parts, giving a correct, realistic uncertainty budget for some features is still challenging. Yet, a lot of work can be done to further estimate the total uncertainty for each and every feature, to answer the question “how accurate will be the measurement result for a new industrial part”…

REFERENCES

[1] Wikipedia, http://en.wikipedia.org/wiki/Computed_tomography, visited September 29th, 2013.

[2] Website Nikon Metrology, http://www.nikonmetrology.com, visited October 1st, 2013.

[3] MUDERS, J., HESSER, J., LACHNER, A., REINHART, C., Accuracy Evaluation and Exploration of Measurement Uncertainty for Exact Helical Cone Beam Reconstruction Using Katsevich Filtered Backprojection in Comparison to Circular Feldkamp Reconstruction with Respect to Industrial CT Metrology, International Symposium on Digital Industrial Radiology and Computed Tomography - Mo.2.2.

[4] OBRIST, A. F., FLISCH, A., HOFMANN, J., Point cloud reconstruction with sub-pixel accuracy by slice-adaptive thresholding of X-ray computed tomography images, NDT&E International 37, p. 373–380, 2004.

[5] REINHART, C., Industrial computer tomography – a universal inspection tool, 17th World Conference on Nondestructive Testing, Shanghai, China, 25-28 Oct, 2008.

[6] http://www.iis.fraunhofer.de/en/bf/xrt/system/xxl-ct.html, visited, October 21st, 2013.

[7] Phoenix, http://www.phoenix-xray.com, visited July 5th, 2013.

[8] Metris, http://www.metris.com, visited June 26th, 2013.

[9] HANKE R., FUCHS T., UHLMANN N., X-ray based methods for non-destructive testing and material characterization, Nuclear Instruments and Methods in Physics Research 591, p. 14–18, 2008.

[10] K. Holt. X-ray production&emission. http://www.elcamino.edu/faculty/kholt/RT%20111%20presentations/X-Ray%20Production%20&%20Emission_W4.ppt

[11] KRUTH, J.-P., BARTSCHER, M., CARMIGNATO, S., SCHMITT, R., DE CHIFFRE, L., WECHENMANN, A., Computed tomography for dimensional metrology, CIRP Annals - Manufacturing Technology, Volume 60, Issue 2, p. 821-842, 2011.

[12] REINHART, C., Industrial computer tomography - A universal inspection tool, 17th World Conference on Nondestructive Testing (WCNDT2008), Shanghai, China, 2008.

[13] CARMIGNATO, S., DREOSSI, D., MANCINI, L., MARINELLO, F., TOMBA, G., SAVIO, E., Testing of X-ray microtomography systems using a traceable geometrical standard, Measurement Science and Technology 20, 084021, (7pp), 2010.

[14] ANDREU, V., GEORGI, B., LETTENBAUER, H., YAGÜE, J.A., Analysis of the error sources of a Computer Tomography Machine, Iberprecis S.L., Spain; Carl Zeiss, Germany; Univ. of Zaragoza, Spain.

[15] WELKENHUYZEN, F., KIEKENS, K., PIERLET, M., DEWULF, W., BLEYS, P., KRUTH, J.-P., Industrial computed tomography for dimensional metrology: Overview of influence factors and improvement strategies, 4th Intern. Conf. on Optical Measurement Techniques, May 25th-26th, Antwerp, Belgium, p.401-410, 2009.

[16] KATSEVICH, A., 3PI algorithms for helical computer tomography, Advances in Applied Mathematics, vol. 36, p. 213–250, 2006.

[17] CANTATORE, A., MÜLLER, P., Introduction to Computed Tomography, DTU, 2011.

[18] NEUMAYER D., MODRICH K., MAISL M., KASPERL S., Computed Tomography as a tool for industrial measurement, ECNDT 2006 - We.3.3.2, 2006.

[19] FRANZ M., KASPERL S., Quality and Speed Improvements in Industrial CT by the Use of an additional Optical Sensor, ECNDT 2006 - We.3.3.3, 2006.

[20] KRUMM M., KASPERL, S., Franz M., Reducing non-linear artifacts of multi-material objects in industrial 3D computed tomography, NDT&E International 41, 2008, p. 242–251.

[21] WENIG P., KASPERL S., Examination of the Measurement Uncertainty on Dimensional Measurements by X-ray Computed Tomography, ECNDT 2006 - We.3.3.1.

[22] KASPERL, S., HILLER, J., KRUMM, M., Computed Tomography Metrology in industrial Research & Development, International Symposium on NDT in Aerospace, Fürth, Germany, December 3-5, 2008.

[23] FELDKAMP, L, DAVID, L., KRESS, J., Practical cone–beam algorithm, Journal of the Optical Society of America, vol. 1, no. 6, pp. 612–619, 1984.

[24] VAN GESTEL, N., Determining measurement uncertainties of feature measurements on CMMs, PhD, KU Leuven, September, 2011.

[25] ISO/WD 10360-11, GPS - Acceptance and reverification tests for CMMs - Part 11: Computed tomography. ISO, Geneva, 2011.

[26] VDI/VDE 2617 - Part 1.3 draft (2009) Guideline for the application of DIN EN ISO 10360 for CMMs with CT-sensors. VDI, Dusseldorf, 2009.

[27] BARTSCHER, M., et al., Enhancement and proof of accuracy of industrial computed tomography measurements. CIRP Annals, 56/1:495–498, 2007.

[28] CARMIGNATO, S., SAVIO, E., Traceable volume measurements using coordinate measuring systems, CIRP Annals - Manufacturing Technology, Volume 60, Issue 1, Pages 519–522, 2011.

[29] CANTATORE, A., MÜLLER, P., Introduction to computed tomography, DTU, 2011.

[30] FRANZ M., KASPERL S., Quality and Speed Improvements in Industrial CT by the Use of an additional Optical Sensor, ECNDT - We.3.3.3, 2006.

[31] SIMON, M., TISEANU, I., SAUERWEIN, C., YOO, S.-M., CHO, I.-S., Development of multi sensor and multi-source computed tomography systems, DIR 2007 - International Symposium on Digital industrial Radiology and Computed Tomography, Lyon, France, June 25-27, 2007.

[32] WECKENMANN, A., JIANG, X., SOMMER, K.-D., NEUSCHAEFER-RUBE, U., SEEWIG, J., SHAW, L., ESTLER, T., Multisensor data fusion in dimensional metrology, CIRP Annals - Manufacturing Technology 58, p. 701-721, 2009.

[33] WECKENMANN, A., KRÄMER, P., Application of Computed Tomography in Manufacturing Metrology, Technisches Messen 76, Friedrich Alexander Universtität, Erlangen-Nürnberg, 2009.

[34] Website Werth, http://www.werth.de/, visited, July 8th, 2013.

[35] WENIG P., KASPERL S., Examination of the Measurement Uncertainty on Dimensional Measurements by X-ray Computed Tomography, ECNDT 2006 - We.3.3.1.

[36] REITER, M., HEINZL, C., SALABERGER, D., WEISS, D., KASTNER, J., Study on parameter variation of an industrial computed tomography simulation tool concerning dimensional measurement deviations, http://www.ndt.net/article/ecndt2010/reports/1_09_04.pdf.

[37] HILLER, J., KASPERL, S., Analyse von Einflussgrößen beim dimensionellen Messen mittels Röntgencomputertomographie, DGZfP-Jahrestagung 2007 - Vortrag 48, 2007.

[38] KUMAR, J., ATTRIDGE, A., WOOD, P.K.C., WILLIAMS, M.A., Analysis of the effect of cone-beam geometry and test object configuration on the measurement accuracy of a computed tomography scanner used for dimensional measurement, Meas. Sci. technol. 22, 035105, 2011.

[39] HILLER, J., REINDL, L. M., A computer simulation platform for the estimation of measurement uncertainties in dimensional X-ray computed tomography, Measurement 45, p. 2166–2182, 2012.

[40] BOAS, F., E., FLEISCHMANN, D., CT artifacts: Causes and reduction techniques, 2012.

[41] NEUMAYER D., MODRICH K., MAISL M., KASPERL S., Computed Tomography as a tool for industrial measurement, ECNDT 2006 - We.3.3.2, 2006.

[42] http://ctartifacts.blogspot.be/2013/10/cupping-artifacts.html

[43] KRIMMEL, S., STEPHAN J., BAUMANN, J., 3D computed tomography using a microfocus X-ray source: Analysis of artifact formation in the reconstructed images using simulated as well as experimental projection data, Nuclear

[44] KRUMM, M., KASPERL, S., FRANZ, M., Beam Hardening Correction of Multi-Material Objects, http://www.ndt.net/article/ecndt2010/reports/1_09_27.pdf.

[45] KRUMM, M., KASPERL, S., FRANZ, M., Reducing non-linear artifacts of multi-material objects in industrial 3D computed tomography, NDT&E International 41, p. 242–251, 2008.

[46] SHAMMAA, M.H., OHTAKE, Y., SUZUKI, H., Segmentation of multi-material CT data of mechanical parts for extracting boundary surfaces, Computer-Aided Design 42, p. 118-128, 2010.

[47] FUJIMORI, T., SUZUKI, H., Surface extraction from multi-material CT data.

[48] HEINZL, C., KASTNER, J., GRÖLLER, E., Surface Extraction from Multi-Material Components for Metrology using Dual Energy CT, IEEE Transactions on visualization and computer graphics, vol. 15, no. 6, p. 1520-1527, 2007.

[49] KRÄMER, P., WECKENMANN, A., Multi-energy image stack fusion in computed tomography, Meas. Sci. Technol. 21, 045105 (7pp), 2010.

[50] HEINZL, C., KASTNER, J., MÖLLER, T., GRÖLLER, E., Statistical analysis of Multi-Material Components using Dual Energy CT.

[51] KASPERL, S., FRANZ, M., Registration concepts for the just-in-time artefact correction by means of virtual computed tomography, DIR 2007 - International Symposium on Digital industrial Radiology and Computed Tomography, Lyon, France, June 25-27, 2007.

[52] KASPERL, S., Qualitätsverbesserungen durch referenzfreie Artefaktreduzierung und Oberflächennormierung in der industriellen 3D-Computertomographie, PhD, 2005.

[53] BRUNKE, O., SUPPES, A., Precise 3D dimensional metrology using high resolution X-ray computed tomography (μCT), GE Sensing & Inspection Technologies GmbH, phoenix|x-ray, Wunstorf, Germany, http://www.ndt.net/article/ecndt2010/reports/1_09_08.pdf.

[54] DEWULF, W., TAN, Y., KIEKENS, K., Sense and non-sense of beam hardening correction in CT metrology, CIRP Annals - Manufacturing Technology Volume 61, Issue 1, Pages 495–498, 2012.

[55] SUPPES, A., NEUSER, E., Metrology with µCT: Precision Challenge, phoenix|x-ray systems and services GmbH.

[56] HILPERT, U., BARTSCHER, M., NEUGEBAUER, M., GOEBBELS, J., WEIDEMANN G., BELLON C., Simulation-aided computed tomography (CT) for dimensional measurements, Proc. Of DIR2007, Lyon, France, 2007.

[57] WECKENMANN, A., KRÄMER, P., Assessment of measurement uncertainty caused in the preparation of measurements using computed tomography, XIX IMEKO World Congress on Fundamental and Applied Metrology, p. 1888-1892, Lisbon, Portugal, 6-11 September 2009.

[58] KIEKENS, K., WELKENHUYZEN, F., TAN, Y., BLEYS, Ph., VOET, A., KRUTH, J.-P., DEWULF, W., A test object with parallel grooves for calibration and ccuracy assessment of industrial computed tomography (CT) metrology, Meas. Sci. Technol. 22, 2011.

[59] HEINZL, C., KASTNER, J., AMIRKHAMOV, A., GRÖLLER, E., GUSENBAUER, C., Optimal specimen placement in cone beam X-ray computed tomography, NDT & E International, Volume 50, p. 42–49, 2012.

[60] KRUTH, J.-P., VANHERCK, P., DE JONGHE, L., Self-calibration method and software error correction for three-dimensional coordinate measuring machines using artefact measurements, Measurement 14, p.157-167, 1994.

[61] BARTSCHER, M., HILPERT, U., NEUSCHAFER-RUBE, U., Industrielle Computertomographie auf dem Weg zur Koordinatenmesstechnik, PTB-Mitteilungen 117 Heft 4, p. 397-406, 2007.

[62] SAEWERT H., FIEDLER D., BARTSCHER M., WÄLDELE F., Obtaining dimensional information by industrial CT-scanning – present and prospective process chain, International Symposium on Computed Tomography and Image Processing, DGZfP Conference book BB 84-CD, Berlin, 2003.

[63] BARTSCHER M., NEUSCHAEFER-RUBE U., WÄLDELE F., Computed Tomography – A Highly potential tool for industrial quality control and production near measurements, Braunschweig, Germany.

[64] HILLER, J., MAISL, M., REINDL, L. M., Physical characterization and performance evaluation of an X-ray micro-computed tomography system for dimensional metrology applications, Meas. Sci. Technol. 23, 085404 (18pp), 2012.

[65] LETTENBAUER, H., GEORGI, B., WEISS, D., Means to Verify the Accuracy of CT Systems for Metrology Applications (In the Absence of Established International Standards), DIR 2007 - International Symposium on Digital industrial Radiology and Computed Tomography, Lyon, France, June 25-27, 2007.

[66] WELKENHUYZEN, F., INDESTEEGE, D., BOECKMANS, B., KIEKENS, K., TAN, Y. , DEWULF, W., KRUTH, J.-P., Accuracy study of a 450 kV CT system with a calibrated test object, 11th International Symposium on Measurement and Quality Control 2013, September 11-13, Cracow-Kielce, Poland, 2013.

[67] MÜLLER, P., HILLER, J., CANTATORE, A., TOSELLO, G., DE CHIFFRE, L., New reference object for metrological performance testing of industrial CT systems, Proceedings of the 12th euspen International Conference, Stockholm, June, 2012.

[68] MULLER, P., HILLER, J., CANTATORE, A., BARTSCHER, M., DE CHIFFRE, L., Investigation on the influence of image quality in X-ray CT metrology, http://orbit.dtu.dk/fedora/objects/orbit:114296/datastreams/file_10509658/content.

[69] BARTSCHER M., HILPERT U., GOEBBELS J., WIEDEMANN G., Enhancement and Proof of Accuracy of Industrial Computed Tomography (CT) Measurements, Annals of the CIRP Vol. 56 Issue 1, p. 495-498, 2007.

[70] BARTSCHER, M., STAUDE,A., EHRIG, K., RAMSEY, A., The Influence of Data Filtering on Dimensional Measurements with CT, 18th World Conference on Nondestructive Testing, Durban, South Africa, 16-20 April, 2012.

[71] CARMIGNATO, S., PIEROBON, A., SAVIO, E., Interlaboratory Comparison of Computed Tomography Systems for Dimensional Metrology, Final Report, 2011.

[72] CARMIGNATO, S., Accuracy of industrial computed tomography measurements: Experimental results from an international comparison, CIRP Annals - Manufacturing Technology 61, p. 491–494, 2012.

[73] NEUSCHAEFER-RUBE, U., NEUGEBAUER, M., EHRIG, W., BARTSCHER, M., HILPERT, U., Tactile and optical microsensors: test procedures and standards, Meas. Sci. Technol. 19, 084010 (5pp), 2008.

[74] BARTSCHER, M., NEUKAMM, M., KOCH, M., NEUSCHAEFER-RUBE, U., STAUDE, A., GOEBBELS, J., EHRIG, K., Performance assessment of geometry measurements with micro-ct using a dismountable work-piece-near reference standard, 2010.

[75] BARTSCHER, M., EHRIG, K., STAUDE, A., GOEBBELS, J., Application of an Industrial CT Reference Standard for Cast Freeform Shaped Workpieces, International Symposium on Digital Industrial Radiology and Computed Tomography - We.4.3, 2011.

[76] STAUDE, A., GOEBBELS, J., EHRIG, K., BARTSCHER, M., KOCH, M., NEUSCHAEFER-RUBE, U., A new test piece for geometry and defect measurements with micro-CT, http://www.ndt.net/article/ecndt2010/reports/1_09_11.pdf.

[77] NARDELLI, V. C., PORATH, M., C., ARENHART, F., A., DONATELLI, G. D., Modular test parts to assess the quality of computed tomography dimensional measurements, http://www.ndt.net/article/ctc2012/papers/271.pdf.

[78] EHRIG, K., BARTSCHER, M., GOEBBELS, J., HÄRTIG, F., KNIEL, K., NEUKAMM, M., NEUSCHAEFER-RUBE, U., STAUDE, A., Dimensional Control of Micro Components with Synchrotron Computed Tomography, 9th Int. Symp. on Measurement and Intelligent Instruments – ISMTII 2009, Saint-Petersburg, Russia, June 29th – July 2nd, Proceedings: Vol.1: p. 256-261, 2009.

[79] EHRIG, K., GOEBBELS, J., STAUDE, A., BARTSCHER, M., HÄRTIG, F., KNIEL, K., NEUKAMM, M., NEUSCHAEFER-RUBE, U., HILPERT, U., Dimensionelles Messen von innenliegenden Mikrostrukturen mit Computertomographie am Beispiel kleiner Hohlzahnräder, DGZfP-Jahrestagung Di.1.A.3, 2009.

[80] ONTIVEROS, S., YAGÜE-FABRA, J. A., JIMENEZ, R., TOSELLO, G., GASPARIN, S., PIEROBON, A., CARMIGNATO, S., HANSEN, H.N ., Dimensional measurement of micro-moulded parts by computed tomography, Meas. Sci. Technol. 23, 125401 (9pp), 2012.

[81] YAGÜE, J.A., TOSELLO, G., CARMIGNATO, S., ONTIVEROS, S., JIMENEZ, R., GASPARIN, S., HANSEN, H.N., PIEROBON, A., Measurement of micro moulded parts by Computed Tomography and comparison to optical and tactile techniques, Proceedings of the 11th euspen International Conference, Como, May, 2011.

[82] MARINELLO, F., SAVIO, E., CARMIGNATO, S., DE CHIFFRE, L., Calibration artefact for the microscale with high aspect ratio: The fiber gauge, CIRP Annals – Manufacturing Technolgoy 57, p. 497-500, 2008.

[83] CARMIGNATO, S., DREOSSI, D., MANCINI, L., MARINELLO, F., TOMBA, G., SAVIO, E., Testing of X-ray microtomography systems using a traceable geometrical standard, Measurement Science and Technology 20, 084021, (7pp), 2010.

[84] ANGEL, J., DE CHIFFRE, L., LARSEN, E., RASMUSSEN, J., SOBIECKI, R., CIA-CT comparison – Inter laboratory comparison on Industrial Computed Tomography, Reference Measurements, Department of Mechanical Engineering, Technical University of Denmark, 2013.

[85] HEINZL, C., KASTNER, J., GEORGI, B., LETTENBAUER, H., Comparison of surface detection methods to evaluate cone beam computed tomography data for three dimensional metrology, Proc. Of DIR2007, Lyon, France, 2007.

[86] JCGM 200:2012 International vocabulary of metrology – Basic and general concepts and associated terms (VIM), 2012

[87] VDI/VDE 2617 - Part 2.1 (2015) Computed Tomography in dimensional measurement; determination of the uncertainty of measurement and the test process suitability of coordinate measurement systems with CT sensors.

[88] BARTSCHER, M., NEUKAMM, M., HILPERT, U., NEUSCHAEFER-RUBE, U., HÄRTIG, F., KNIEL, K., EHRIG, K., STAUDE, A., GOEBBELS, J., Achieving traceability of industrial computed tomography.

[89] YAGÜE-FABRA, J.A., ONTIVEROS, S., JIMÉNEZ, R., CHITCHIAN, S., TOSELLO, G., CARMIGNATO, S., A 3D edge detection technique for surface extraction in computed tomography for dimensional metrology applications, CIRP Annals – Manufacturing Technology 62, p. 531–534, 2013.

[90] SCHMITT, R., NIGGEMANN, C., Uncertainty in measurement for X-ray-computed tomography using calibrated work pieces, Meas. Sci. Technol. 21, 054008 (9pp), 2010.

[91] ISO/FDIS 14253-2: 2011. Geometrical product specifications (GPS) — Inspection by measurement of workpieces and measuring equipment — Part 2: Guidance for the estimation of uncertainty in GPS measurement, in calibration of measuring equipment and in product verification.

[92] FRANZ, M., FUNK, C., HILLER, J., KASPERL, S., KRUMM, M., SCHRÖPFER, S., Reliability of Dimensional Measurements by Computed Tomography for Industrial Applications, 4th European-American Workshop on Reliability of NDE - Th.4.B.3.

[93] HÄRTIG, F., KRYSTEK, M., Correct treatment of systematic errors in the evaluation of measurement uncertainty, Physikalisch-Technische Bundesanstalt, Braunschweig und Berlin (PTB).

[94] HILLER, J., REINDL, L. M., A computer simulation platform for the estimation of measurement uncertainties in dimensional X-ray computed tomography, Measurement 45, p. 2166–2182, 2012.

[95] JIMENEZ, R., ONTIVEROS, S., CARMIGNATO, S., YAGÜE, J.A., Correction strategies for the use of a conventional micro-CT cone beam machine for metrology applications, Procedia CIRP 2, 34 – 37, 2012.

[96] MULLER, P., HILLER, J., CANTATORE, A., DE CHIFFRE, L., A study on evaluation strategies in dimensional X-ray computed tomography by estimation of measurement uncertainties, Int. J. Metrol. Qual. Eng. 3, p. 107–115, 2012.

[97] MULLER, P., HILLER, J., DAI, Y., ANDREASEN, J.L., HANSEN, H.N., DE CHIFFRE, L., Estimation of measurement uncertainties in X-ray computed

tomography metrology using the substitution method, CIRP Journal of Manufacturing Science and Technology 7, p.222-232, 2014.

[98] NARDELLI, V., DONATELLI, G. D., ARENHART, F. A., PORATH, M. C., Uncertainty evaluation of computed tomography measurements using multiple calibrated workpieces

[99] LETTENBAUER, H., GEORGI, B., WEISS, D., Means to Verify the Accuracy of CT Systems for Metrology Applications (In the Absence of Established International Standards), DIR 2007 - International Symposium on Digital industrial Radiology and Computed Tomography, Lyon, France, June 25-27, 2007.

[100] NARDELLI, V. C., ARENHART, F. A., DONATELLI, G. D., PORATH, M., NIGGEMANN, C., SCHMITT, R., Feature-based analysis for quality assessment of X-ray computed tomography measurements, Meas. Sci. Technol. 23, 105006 (14pp), 2012.

[101] ISO/IEC Guide 98-3:2008, Uncertainty of measurements - Part 3: Guide to the expression of uncertainty in measurements (GUM 2008).

[102] HEINZL, C., KASTNER, J., GEORGI, B., LETTENBAUER, H., Comparison of surface detection methods to evaluate cone beam computed tomography data for three dimensional metrology, DIR 2007 - International Symposium on Digital industrial Radiology and Computed Tomography, Lyon, France, June 25-27, 2007.

[103] Webiste LayerWise/3D Systems, http://www.layerwise.com, visited 2010.

[104] GEYER, A., SCAPOLO, F., BODEN, M., DÖRY, T., DUCATEL, K., "The Future of Manufacturing in Europe 2015-2020 – The Challenge for Sustainability", the European Commission and the Institute for Prospective Technological Studies, Brussels, Belgium, 2003.

[105] WECKENMANN, A., ESTLER, T., PEGGS, G., McMURTRY, D., Probing systems in dimensional metrology, CIRP Annals – Manufacturing Technology 53 Issue 2, p. 657-684, 2004.

[106] TAN, YE, Scanning and post-processing parameters optimization for CT dimensional metrology, PhD, KU Leuven, 2015.

LIST OF PUBLICATIONS

ARTICLES IN INTERNATIONALLY REVIEWED ACADEMIC JOURNALS

Tan, Y., **Kiekens, K.**, Welkenhuyzen, F., Angel, J., De Chiffre, L., Kruth, J., Dewulf, W. (2014). Simulation-aided investigation of beam hardening induced errors in CT dimensional metrology. *Measurement Science & Technology, 25* (6), art.nr. 16 (citations: 4) (IF publication year: 1.43) (most recent IF: 1.49).

Dewulf, W., **Kiekens, K.**, Tan, Y., Welkenhuyzen, F., Kruth, J. (2013). Uncertainty Determination and Quantification for Dimensional Measurements with Industrial Computed Tomography. *CIRP Annals. Manufacturing Technology, 62* (1), 535-538. (citations: 8) (IF publication year: 2.54) (most recent IF: 2.49).

Dewulf, W., Tan, Y., **Kiekens, K.** (2012). Sense and Non-Sense of Beam Hardening Correction in CT Metrology. *CIRP Annals. Manufacturing Technology, 61* (1), art.nr. CIRP779, 495-498. (citations: 20) (IF publication year: 2.25) (most recent IF: 2.49).

Kiekens, K., Welkenhuyzen, F., Tan, Y., Bleys, P., Voet, A., Kruth, J., Dewulf, W. (2011). A test object with parallel grooves for calibration and accuracy assessment of industrial CT metrology. *Measurement Science & Technology, 22*, 1-7. (citations: 16) (IF publication year: 1.49) (most recent IF: 1.49).

PAPERS AT INTERNATIONAL SCIENTIFIC CONFERENCES AND SYMPOSIA, PUBLISHED IN FULL IN PROCEEDINGS

Welkenhuyzen, F., Boeckmans, B., Tan, Y., **Kiekens, K.**, Dewulf, W., Kruth, J. (2014). Investigation of the Kinematic System of a 450 kV CT Scanner and its Influence on Dimensional CT Metrology Applications. *Proceedings of the 5th International Conference on Industrial Computed Tomography*. International Conference on Industrial Computed Tomography. Wels, Austria, 25-28 February 2014 (pp. 217-225).

Tan, Y., **Kiekens, K.**, Welkenhuyzen, F., Angel, J., De Chiffre, L., Kruth, J., Dewulf, W. (2013). Simulation-aided investigation of beam hardening induced errors in CT dimensional metrology. *Proceedings of the International Symposium on Measurement Technology and Intelligent Instruments*. International Symposium on Measurement Technology and Intelligent Instruments. Aachen, Germany, 1-5 July 2013 (pp. 1-7).

Tan, Y., **Kiekens, K.**, Welkenhuyzen, F., Kruth, J., Dewulf, W. (2013). Defining the Optimal Beam Hardening Correction Parameters for CT Dimensional Metrology Applications. *International Conference on Competitive Manufacturing*. International Conference on Competitive

Manufacturing. Stellenbosch, South Africa, 30 January - 1 February 2013 (pp. 137-143).

Welkenhuyzen, F., Indesteege, D., Boeckmans, B., **Kiekens, K.**, Tan, Y., Dewulf, W., Kruth, J. (2013). ACCURACY STUDY OF A 450 KV CT SYSTEM WITH A CALIBRATED TEST OBJECT. *Proceedings of the 11th IMEKO TC14 International Symposium on Measurement and Quality Control (ISMQC 2013).* IMEKO TC14 International Symposium on Measurement and Quality Control (ISMQC 2013). Cracow, Poland, 11-13 September 2013 (pp. 297-300).

Kiekens, K., Tan, Y., Welkenhuyzen, F., Kruth, J., Dewulf, W. (2012). Uncertainty Determination for Dimensional Measurements with Computed Tomography. . Conference on Industrial Computed Tomography. Wels, Austria, 19-21 September 2012.

Tan, Y., **Kiekens, K.**, Welkenhuyzen, F., Kruth, J., Dewulf, W. (2012). Beam hardening correction and its influence on the measurement accuracy and repeatability for CT dimensional metrology applications. . Conference on Industrial Computed Tomography. Wels, Austria, 19-21 September 2012.

Kiekens, K., Tan, Y., Kruth, J., Voet, A., Dewulf, W. (2011). Parameter dependent thresholding for dimensional X-ray computed tomography. *Proceedings of the International Symposium on Digital Industrial Radiology and Computed Tomography*. International Symposium on Digital Industrial Radiology and Computed Tomography.

Tan, Y., **Kiekens, K.**, Kruth, J., Voet, A., Dewulf, W. (2011). Material Dependent Thresholding for Dimensional X-ray Computed Tomography. In Tan, Y. (Ed.), *DGZFP-Proceedings BB 128-CD*. International Symposium on Digital Industrial Radiology and Computed Tomography. Berlin, Germany, 20-22 June 2011 (art.nr. Mo.4.3).

Kiekens, K., Welkenhuyzen, F., Tan, Y., Bleys, P., Voet, A., Dewulf, W., Kruth, J. (2010). A test object for calibration and accuracy assessment in X-ray CT metrology. . 10th International Symposium on Measurement and Quality Control (ISMQC-2010). Osaka, Japan, 5-9 September 2010.

Welkenhuyzen, F., **Kiekens, K.**, Pierlet, M., Dewulf, W., Bleys, P., Kruth, J., Voet, A. (2009). Industrial computer tomography for dimensional metrology: Overview of influence factors and improvement strategies. *Proceedings of the 4th International Conference on Optical Measurement Techniques for Structures and Systems: Optimess2009*. International Conference on Optical Measurement Techniques for Structures and Systems: Optimess. Antwerp, Belgium, 25-26 May 2009 (pp. 401-410).

Nobels, T., Willemaerts, C., Buijs, J., **Kiekens, K.**, Boonen, R., Dewulf, W. (2008). Development of new engineering projects as a cooperation of industry and bachelor grade students, with reduced industrial coaching effort. . SEFI Annual Conference. Aalborg, Denmark, 2-5 July 2008.

MEETING ABSTRACTS, PRESENTED AT INTERNATIONAL SCIENTIFIC CONFERENCES AND SYMPOSIA, PUBLISHED OR NOT PUBLISHED IN PROCEEDINGS OR JOURNALS

Voet, A., **Kiekens, K.**, Welkenhuyzen, F., Tan, Y., Dewulf, W., Kruth, J. (2010). A test object for calibration and accuracy assessment in X-ray CT metrology. International Symposium on Measurement and Quality Control. Convention Center, Osaka University,, Japan, 5-9 September 2010.

ARTICLES IN OTHER PROFESSIONALLY ORIENTED JOURNALS

Paulus, P., **Kiekens, K.**, Welkenhuyzen, F., Bleys, P. (2009). Time-to-market van producten drastisch ingekort met CT-scannen. *Metallerie, 124*, 25-26.

CURRICULUM VITAE

ALGEMEEN

° 29 augustus 1982
Lange Lostraat 4a, 3010 Kessel-Lo
Partner van Wim Wevers
mama van Joppe (18.03.2009), Eppo (22.01.2014) en Pippa (15.06.2016)

WERKERVARING

2007-heden	Assistent Katholieke Universiteit Leuven, faculteit Industriële Ingenieurswetenschappen, Campus Groep T (Leuven)

OPLEIDINGEN

2000-2005	**Master in de Industriële Ingenieurswetenschappen, optie elektromechanica** *Groep T, Leuven, afgestudeerd met **grote onderscheiding*** Eindwerk: "Studie over slip op de aandrijvingen van achtbanen (in Plopsaland)" (Promotor: Prof. Guido Ceulemans)
2005-2007	**Master in de Ingenieurswetenschappen, werktuigkundig-elektrotechnisch ingenieur, optie mechanica** (verkort programma voor industrieel ingenieurs na toelatingsproef) *Katholieke Universiteit Leuven, afgestudeerd met **onderscheiding*** Eindwerk: "Verwarmingssystemen voor lage-energiewoningen" (Promotor: Prof. Lieve Helsen)
2008	**Opleiding tot energiedeskundige, type A** *Syntra, Mechelen; erkenning behaald*
2012-2014	**Opleiding tot brood- en banketbakker (avondschool)** *Syntra, Leuven; getuigschrift behaald*
2015	**Opleiding 'inspirerend coachen'** *KU Leuven, door Tuur en Pieter Spaepen*
2009-2017	**Doctoraatsopleiding in de Ingenieurswetenschappen**